Design Optimization for Spatial Arrangement of Used Nuclear Fuel Containers

by

Jeremy Pui Fung Leong

A thesis
presented to the University of Waterloo
in fulfillment of the
thesis requirement for the degree of
Master of Applied Science
in
Systems Design Engineering

Waterloo, Ontario, Canada, 2020

Author's Declaration

I hereby declare that I am the sole author of this thesis. This is a true copy of the thesis, including any required final revisions, as accepted by my examiners.

I understand that my thesis may be made electronically available to the public.

Abstract

Canada's proposed deep geological repository is a multiple-barrier system designed to isolate used nuclear fuel containers (UFCs) indefinitely with no release of radionuclides for at least one million years. Placing UFCs together as densely as possible is ideal for mitigating repository size and cost. However, due to heat generation from radioactive decay and material limitations, a key design criterion is that the maximum temperature inside the repository must not exceed 100 °C. To satisfy that criterion, design optimization for the spatial arrangement of UFCs in a crystalline rock repository is performed. Spatial arrangement pertains to: (i) the spacing between UFCs, (ii) the separation between placement rooms underground, and (iii) the locations of variously aged UFCs that generate heat at different rates. Most studies have considered UFCs to be identical in age during placement into the repository. Parameter analyses have also been performed to evaluate repository performance under probable geological conditions. In this work, the various ages of UFCs and the uncertainties in spacing-related design variables are of focus. Techniques for the actual placement of UFCs in the deep geological repository based on their age and methods for repository risk analysis using yield optimization are developed.

The thermal evolution inside the deep geological repository is simulated using a finite element model. With many components inside the massive repository planned for upwards of 95 000 UFCs, direct optimization of the model is impractical or even infeasible due to it being computationally expensive to evaluate. Surrogate optimization is used to overcome that burden by reducing the number of detailed evaluations required to reach the optimal designs. Two placement cases are studied: (i) UFCs all having been discharged from a Canadian Deuterium Uranium reactor for 30 years, which is a worst-case scenario, and (ii) UFCs having been discharged between 30 and 60 years. Design options that have UFC spacing 1–2 m and placement room separation 10–40 m are explored. The placement locations of the variously aged UFCs are specified using either sinusoidal (cosine) functions or Kumaraswamy probability density functions.

Yield optimization under assumed design variable tolerances and distributions is performed to minimize the probability of a system failure, which occurs when the maximum temperature constraint of 100 °C is exceeded. This method allows variabilities from the manufacturing and construction of the repository components that affect the design variables to be taken into account, incorporating a stochastic aspect into the design optimization that surrogate optimization would not include. Several distributions for the design variables are surveyed, and these include uniform, normal, and skewed distributions—all of which are approximated by Kumaraswamy distributions.

Acknowledgements

I would like to express my deep gratitude to my supervisors Prof. Kumaraswamy Ponnambalam and Prof. Ali Elkamel for their guidance, encouragement, and valuable advice toward this research work. I am sincerely thankful for the opportunity to pursue a MASc in Systems Design Engineering.

I would also like to express my appreciation to my thesis readers Prof. Chrystopher Nehaniv and Prof. Qinqin Zhu for their time and efforts to provide insightful feedback and commentaries.

Thank you to the Nuclear Waste Management Organization, especially Dr. Peter Keech and Dr. Jeff Binns, for their suggestions on the direction of this research.

To my colleagues in the Design Optimization Under Uncertainty Group, my friends, and my family, thank you for the continuous kind words of motivation.

Dedication

To my family, for all the love and support.
Thank you for believing in me every step of the way.

To my mother, Helen, for discipline.
To my father, Wendell, for courage.
To my sister, Fiona, for curiosity.
To my aunt, May, for patience.

Table of Contents

List of Figures

List of Tables

List of Abbreviations

APM	Adaptive Phased Management
CANDU	Canadian Deuterium Uranium
CDF	cumulative distribution function
COMSOL	COMSOL Multiphysics
DGR	deep geological repository
DOE	design of experiments
HCB	highly compacted bentonite
LHD	Latin hypercube design
LHS	Latin hypercube sampling
MAE	mean absolute error
MATSuMoTo	MATLAB Surrogate Model Toolbox
NWMO	Nuclear Waste Management Organization
PDF	probability density function
RBF	radial basis function
RSM	response surface model
SBAO	surrogate-based analysis and optimization
UFC	used nuclear fuel container

Chapter 1

Introduction

1.1 Background and Motivation

Since the first small-scale Canadian Deuterium Uranium (CANDU) prototype reactor was jointly committed in the 1950s by the Atomic Energy of Canada Limited, Ontario Hydro, and Canadian General Electric [1], Canada has positioned itself as a world leader in nuclear energy. Today, nuclear power reactors located in Ontario and New Brunswick generate about 15% of Canada's electricity [2]. This makes nuclear energy one of the largest sources of non-emitting electricity in the country, second only to hydroelectric energy. As the world combats climate change by moving toward clean energy and aiming to reduce greenhouse gas emissions, Canada is doing its part through initiatives such as holding the Québec City Summit on Climate Change, adopting the Paris Agreement, and implementing the Pan-Canadian Framework on Clean Growth and Climate Change. With a target of cutting greenhouse gas emissions to 30% below 2005 levels by 2030 [3], nuclear energy surely plays an integral part of Canada's low carbon future.

All of Canada's nuclear power reactors are CANDU reactors. The acronym derives from the reactors' use of deuterium oxide (heavy water) as their coolant/moderator and natural uranium (compared to enriched uranium used by most other models of nuclear power reactor) as their fuel. A typical CANDU fuel bundle is shown in Fig. 1.1. After irradiation in a nuclear power reactor, most of the used nuclear fuel is composed of uranium with small amounts of transuranic elements and fission products. Although generating power through nuclear energy is non-emitting in terms of greenhouse gases, used nuclear

fuel is radioactive and remains in that state for a long period of time (see Fig. 1.2), so it must be contained and isolated to prevent harm to the biosphere. To date, all the used fuel in Canada is stored in wet and dry storage, which are considered temporary storage. There is a need for a long-term storage solution.

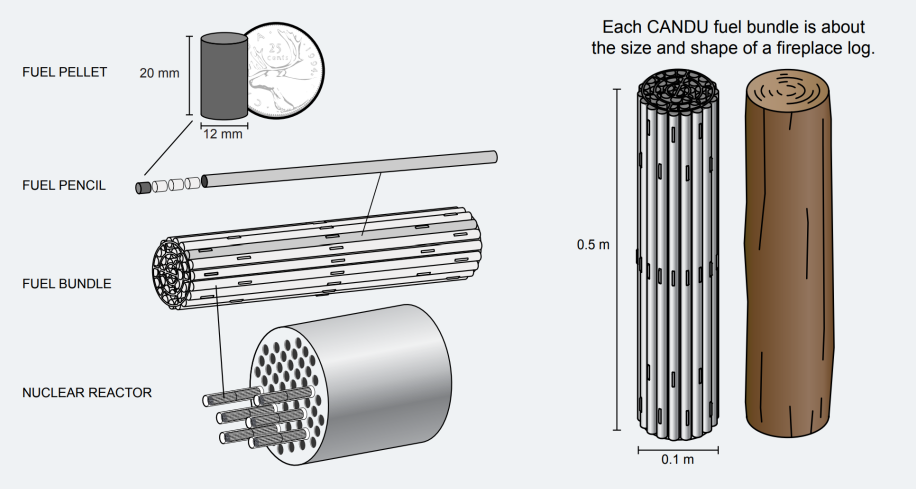

Figure 1.1: CANDU nuclear fuel [4]

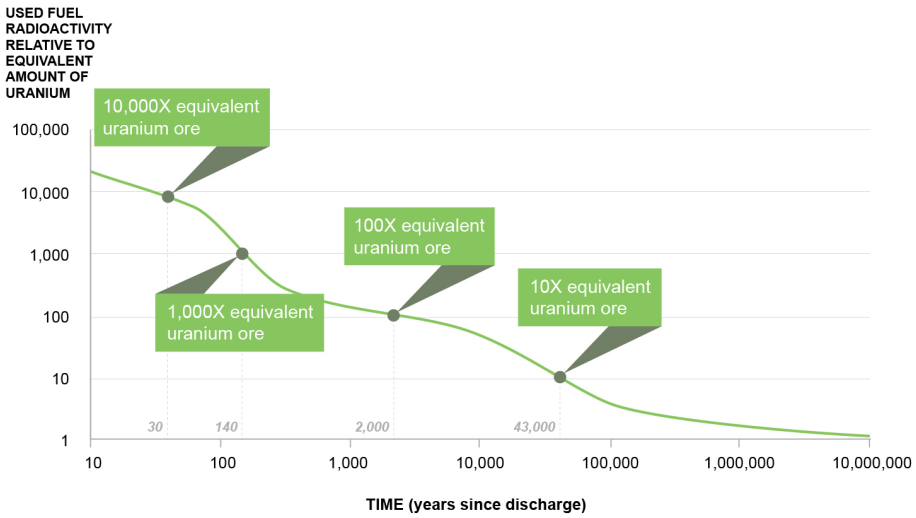

Figure 1.2: Radioactive decay over time in a typical used CANDU fuel [4]

1.2 Canada's Nuclear Waste Solution

Founded in 2002 as the outcome of the Nuclear Fuel Waste Act, the Nuclear Waste Management Organization (NWMO) was assigned the responsibility for the safe design and implementation of a plan to manage Canada's used nuclear fuel [5, 6]. The plan, now known as Adaptive Phased Management (APM), was designed as both a management system and a technical method. In terms of a management system, APM combines phased and adaptive decision-making with public engagement and continuous learning [7]. As a technical method, it involves safely containing and isolating Canada's used nuclear fuel in a central deep geological repository (DGR) at a location with suitable geological characteristics (e.g., the Canadian Shield) [7]. APM consists of various phases, namely [4]:

1. Site selection,
2. Site preparation and construction,
3. Operations,
4. Extended monitoring,
5. Decommissioning and closure, and
6. Post-closure monitoring.

Currently, the site selection process for the location of the DGR is underway. The process commenced in 2010, and 22 communities were initially interested in learning about and potentially welcoming the DGR to their neighbourhoods [5]. Through assessments for DGR suitability, NWMO is expected to select a single preferred site by 2023.

1.3 Deep Geological Repository

The plan for Canada's used nuclear fuel, as set out by NWMO's APM, is the containment and isolation of the high-level radioactive waste inside a DGR in an area with suitable rock formation, with consent from the affected community [4]. Figure 1.3 shows an illustration of a conceptual layout of the repository site, which will comprise surface facilities and the DGR. The surface facilities will include all of those that help to ensure used nuclear fuel is safely received, handled, and placed into the underground repository [4]. The DGR will be designed as a multiple-barrier system for the long-term storage of the used fuel, and it will be constructed at a depth of approximately 500 m underground [8]. In addition to those, a Centre of Expertise will be established either in or near the host community. It will support the testing of the repository site on top of other active research activities [4].

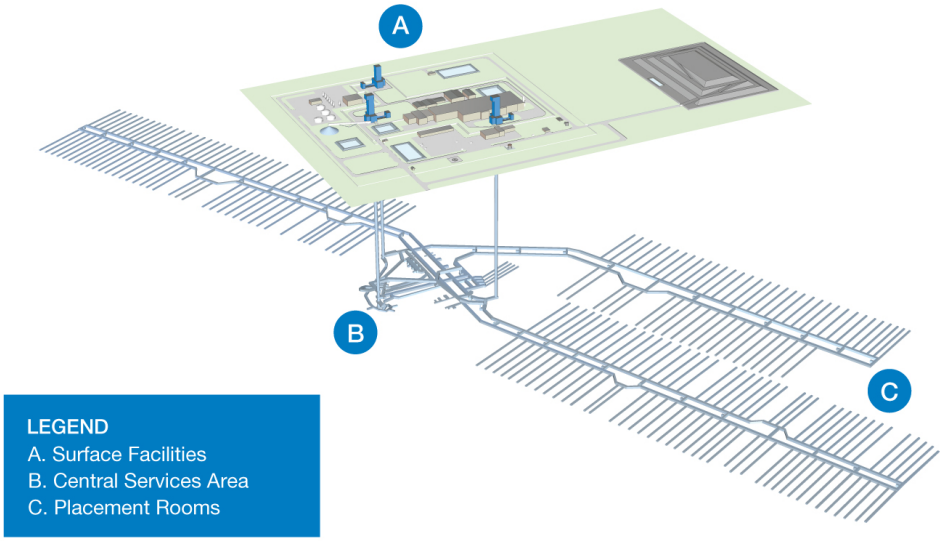

Figure 1.3: Conceptual layout for surface facilities, underground services area, and placement rooms [9]

1.3.1 Multiple-Barrier System

Examining Fig. 1.2, one can see that used nuclear fuel requires approximately one million years until its radioactivity approaches that of natural uranium. Therefore, the constructed DGR will need to contain and isolate used nuclear fuel over that period safely. This will be achieved with the DGR designed as a multiple-barrier system that will utilize engineered and natural barriers. The components of the multiple-barrier system are illustrated in Fig. 1.4 and they are as follows [10]:

1. Fuel pellets,
2. Fuel elements and fuel bundles,
3. Used nuclear fuel containers (UFCs),
4. Bentonite clay, and
5. Host rock (geosphere).

The existing nature of the used nuclear fuel pellets, elements, and bundles will form the first layers of the multiple-barrier system (recall Fig. 1.1). Fuel pellets are very durable ceramics made from uranium dioxide that are placed into sealed tubes called fuel elements, which are made from corrosion-resistant Zircaloy metal. The fuel elements together form fuel bundles, and these are what presently get stored inside wet and dry temporary storage

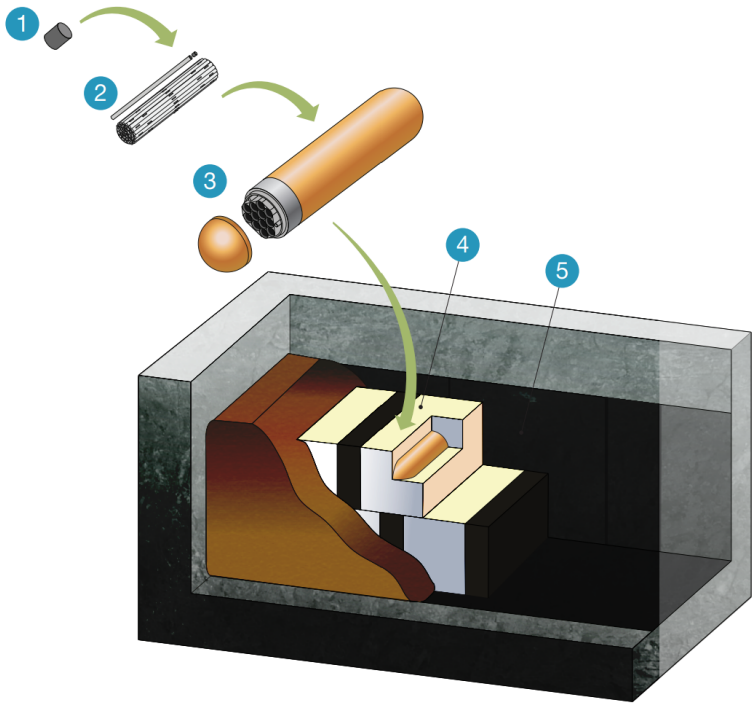

Figure 1.4: Multiple-barrier system containing and isolating used nuclear fuel [5]

located at nuclear power reactor sites. Wet storage is essentially pools of water that provide cooling and shielding against radiation for when fuel bundles are first removed from nuclear power reactors. After about ten years, the fuel bundles are transferred to dry storage, basically large containers/silos with thick concrete walls.

The remaining layers of the multiple-barrier system will be the UFCs, bentonite clay, and the host rock. Under the current design by NWMO, groups of 48 fuel bundles will be placed inside copper-coated carbon steel UFCs, and these will subsequently be set inside bentonite buffer boxes [10]. The host rock in which the DGR is ultimately built will form the outermost layer of protection. With the DGR to be located far underground, the host rock will naturally become a barrier against natural events, water flow, and human intrusion [10]. Its composition will mainly be distinguished as crystalline or sedimentary rock.

1.3.2 UFC and Bentonite Clay

The engineered parts that will be key to the multiple-barrier system are the UFCs and the bentonite clay that encases them. The design and choice of the materials that make up these components have been chosen for specific purposes.

The primary role of the UFCs will be to prevent radionuclides from escaping into the environment. The containers are designed to handle the pressure of overlying rock and future glaciers and will also be corrosion-resistant due to their copper coating [10]. In the past, NWMO has considered modified versions of the KBS-3 UFC design (the method for final disposal of spent nuclear fuel by the Swedish Nuclear Fuel and Waste Management Company) and the original NWMO IV-25 UFC design. However, in 2014, NWMO refined their design to one that is optimized for the uniquely small size of CANDU fuel bundles and other manufacturing considerations [10, 11]. This current Canadian reference design is known as the NWMO Mark II and Fig. 1.5 compares it to the earlier container designs. As mentioned, the container will house 48 CANDU used fuel bundles. This capacity makes the Mark II much smaller in size than the IV-25, which would have contained 288 used fuel bundles, allowing easier handling and placement of Mark II UFCs into the DGR [11, 12]. The Mark II will feature hemispherical ends that are designed to withstand immense pressure, and it will also have a much thinner copper coating (3 mm) as compared to previous container designs [10, 11]. Copper is the chosen corrosion-resistant material because of its favourable thermodynamic stability under anticipated DGR conditions, and less of it will be required for the Mark II thanks to modern coating technologies [11].

UFCs will be set inside buffer boxes made from highly compacted bentonite (HCB). Bentonite clay resists water flow and also swells when exposed to water; thus, acting as a sealing material will be its main role [10]. Sealing is desirable as that will limit the transport of water and dissolved corrosive species toward the UFCs. Note that there are three bentonite clay-based sealing materials present in Fig. 1.4, each with different bulk densities. The buffer boxes (shown in white) are made from HCB, and they are separated by dense backfill/spacer blocks (shown in black). Lining the room is gap-fill material (shown in brown).

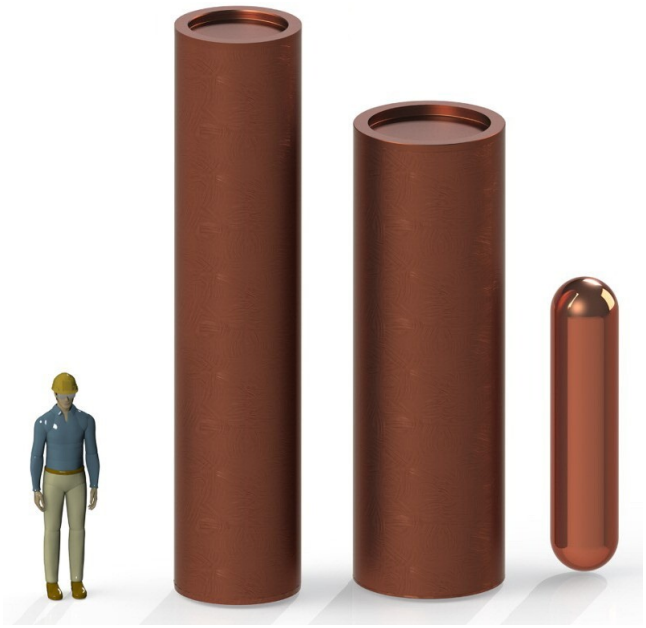

(a) KBS-3 UFC (b) NWMO IV-25 (c) NWMO Mark II

Figure 1.5: Reference UFC designs [11]

1.4 Research Objective

By now, the purpose of NWMO's plan for a DGR has been made clear—to contain and isolate Canada's used nuclear fuel for at least one million years, essentially indefinitely. The DGR and its multiple-barrier system designed by NWMO will need to withstand many processes that may cause the release of used nuclear fuel into the environment. For example, the aforementioned copper coating on the UFCs will be 3 mm thick, and a breach of this layer is considered a failure of the system. Hence, corrosion of the copper coating is one mode of failure that must be mitigated by taking into account a variety of factors such as the chemical and physical properties of groundwater, the presence of bacteria that may participate in microbiologically influenced corrosion, and the thermal evolution at the site [13].

In particular, and of specific interest to this thesis, is a thermal requirement. The DGR is to be designed such that the maximum surface temperature of the UFCs will be less than 100 °C [8]. This requirement ensures that the properties of the surrounding bentonite and copper will not be adversely affected. From observations in nature, bentonite can remain chemically stable for over one million years if its temperature does not exceed 100 °C [14]. At around 125 °C, the electrochemical properties of copper change leading to more rapid corrosion kinetics [8]. At around 140 °C, bentonite starts to convert to illite and becomes a non-swelling clay impractical for sealing purposes [8]. For this thesis, system failure is defined as the maximum temperature inside the DGR surpassing 100 °C.

UFC placement configurations (following reference designs developed by NWMO) in a crystalline rock environment are studied to meet the thermal requirement. As Fig. 1.2 might suggest, the heat output of a UFC is a function of time since its discharge from a CANDU reactor. Based on Fig. 1.3 and 1.4, individual placement rooms are separated by host rock while UFCs are separated from one another by bentonite spacer blocks. If smaller UFC spacings and room spacings are used and if younger containers are grouped closely together in the placement rooms, the temperatures evolved in the DGR will be hotter. So, three main variables of UFC placement will determine the maximum temperature that is seen by the surfaces of the containers inside the repository: (i) UFC spacing, (ii) room spacing, and (iii) UFC age. These design variables form a design optimization problem for the spatial arrangement of UFCs in the DGR such that a maximum temperature constraint (100 °C) is met.

To study the thermal profile inside the DGR, the finite element analysis software COMSOL Multiphysics (COMSOL) is used. As the DGR is composed of various materials and many geometries, obtaining an analytical solution to the heat transfer problem at hand is not possible, and thus a numerical method must be used. While numerical methods are powerful, their computational requirements become very demanding as model size and complexity increase, consequentially increasing computational time. For the design optimization problem described, evaluating many UFC placement configurations directly through COMSOL would be impractical. This inefficiency can be solved by introducing surrogate-based analysis and optimization (SBAO), which refers to the idea of speeding up optimization processes by using surrogate functions to approximate objective and constraint functions [15]. Surrogates are constructed using data drawn from high-fidelity models and provide fast approximations of objectives and constraints at new design points, thereby making intensive sensitivity and optimization studies feasible [15]. Thus, this thesis makes use of SBAO for the design optimization of the UFC placement configuration.

A similar study was conducted earlier by Lin and Ponnambalam [16]. However, the objective here is not only to validate the SBAO independently but to develop techniques for actual placement based on the age of the UFCs and to develop methods for risk analysis using yield optimization (described as follows). As a design optimization problem, the tolerances on the optimum specifications of the DGR are also of interest. From another perspective, realizing the probability of a system failure occurring given specified manufacturing and construction tolerances would be useful for a project that is meant to survive the test of time. This essentially concerns the yield of the DGR project, with yield defined as the probability of a design meeting specifications [17]. With surrogates available from SBAO, this thesis takes this opportune moment to study system failure through yield optimization as well. The system failure probabilities of optimal design points identified from SBAO are quantified, and with given yield targets, new nominal design points are then suggested.

1.5 Thesis Organization

This thesis is divided into six chapters (see Fig. 1.6). The current chapter presented background information concerning Canada's nuclear waste problem and the solution pursued by NWMO and also outlined the research objectives moving forward. Following this introductory chapter, Chapter 2 reviews literature pertaining to the design of the DGR as carried out by academic researchers and NWMO themselves. Literature regarding SBAO and yield optimization are also surveyed for later use in solving and analysing the optimization problems described. In Chapter 3, a numerical model is developed in COMSOL for the simulation of the thermal evolution inside a DGR, and it is then validated against previous work. Chapter 4 makes use of the developed model and applies SBAO to determine optimal design points by approximating the function that represents the maximum temperature inside the DGR under two cases: (i) an inventory with identical UFC age and (ii) an inventory with assorted UFC ages. In the penultimate chapter, Chapter 5, surrogates from Chapter 4 are put to use in yield optimization to explore system failure probabilities under assumed manufacturing and construction tolerances. Finally, the main findings of the thesis are recapitulated in Chapter 6, and future research recommendations are proposed.

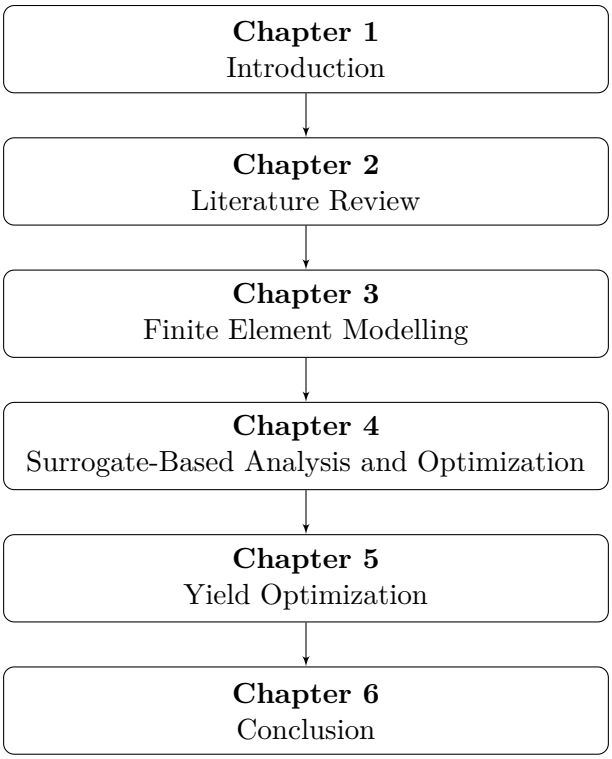

Figure 1.6: Thesis organization by chapter

Chapter 2

Literature Review

The DGR design proposed by NWMO will be located about 500 m underground and will consist of a series of placement rooms home to numerous UFCs. The capsule-shaped UFCs (i.e., cylinders with hemispherical ends) will be encased in bentonite buffer boxes. Based on the existing set of CANDU reactors in Canada, the total projected number of used fuel bundles produced by their end of life ranges approximately 3.5–5.4 million used fuel bundles, which would fill up around 73–113 thousand UFCs [18]. As the maximum temperature inside the DGR is of concern in this thesis, a temperature profile is required. The temperature profile of such a problem of this size and geometry is impossible to determine algebraically; thus, a numerical method must be employed. In this chapter, the thermal evolution inside one of NWMO's proposed DGR as modelled by the finite element analysis software COMSOL is examined to understand the complexity of the maximum temperature experienced by the UFCs. With this understanding and prior to the development of a new numerical model in Chapter 3 for the design optimization of the spatial arrangement of UFCs (based on UFC spacing, room spacing, and UFC age), the concepts and methods of SBAO and yield optimization are also explored.

2.1 Thermal Evolution in a Deep Geological Repository

The idea for a DGR being the solution for the final disposal of used nuclear fuel has been studied numerous times in the past. Guo [28, 29] of NWMO stated that there had been many studies that performed two- and three-dimensional thermal transient and thermo-mechanical analyses, specifically those of [19–27]. Although there was interest in studying behaviours at various repository resolutions, Guo explained that it was numerically

impractical for near-field details to be included in a repository-sized model, hence those analyses were separated into near and far-field modelling. It is important to note that for near-field modelling, adiabatic thermal boundary conditions are often used to create a smaller, infinitely repeating repository model in the horizontal dimensions. However, when interpreting the results for a finite repository using this approach, the thermal evolution is accurate only at early times because the adiabatic boundaries do not represent the heat dissipation at the extents of the repository, causing overestimation in the temperature to occur [25]. To remove the influence of these adiabatic boundary conditions and correct thermal evolution results, Guo first proposed a method in [25] and later revised the approach in [28, 29]. We now explore how this method was applied to NWMO's conceptual DGR in a hypothetical crystalline rock environment and how the maximum temperature evolved in the DGR can be accurately obtained.

2.1.1 Description of a Conceptual Deep Geological Repository

The crystalline rock DGR studied by Guo was based on one of two conceptual DGRs by NWMO [8]—the other being a sedimentary rock DGR. The DGR considered held approximately 4.6 million used fuel bundles or about 96 000 UFCs, and this capacity came from the many placement rooms inside the repository. Rooms were grouped into one of eight distinct sections/panels, each consisting of 35 or 36 rooms (see Fig. 2.1). In each room, there were two layers of UFCs and spacer blocks. Figure 2.2 shows the main components inside the DGR and their geometries while Fig. 2.3 illustrates a layered and perfectly staggered arrangement of the UFCs (in buffer boxes) and spacer blocks. For the purpose of comparing the results from Guo's model to the new model developed later for this thesis in Chapter 3, the following details of Guo's model in [28, 29] are highlighted:

UFC Spacing	Centre-to-centre distance of 1.5 m.
Room Spacing	Centre-to-centre distance of 20 m.
UFC Age	All 30 years out of a nuclear power reactor at time of placement.*

*Information for the heat output of a UFC as a function of time is presented in Chapter 3.

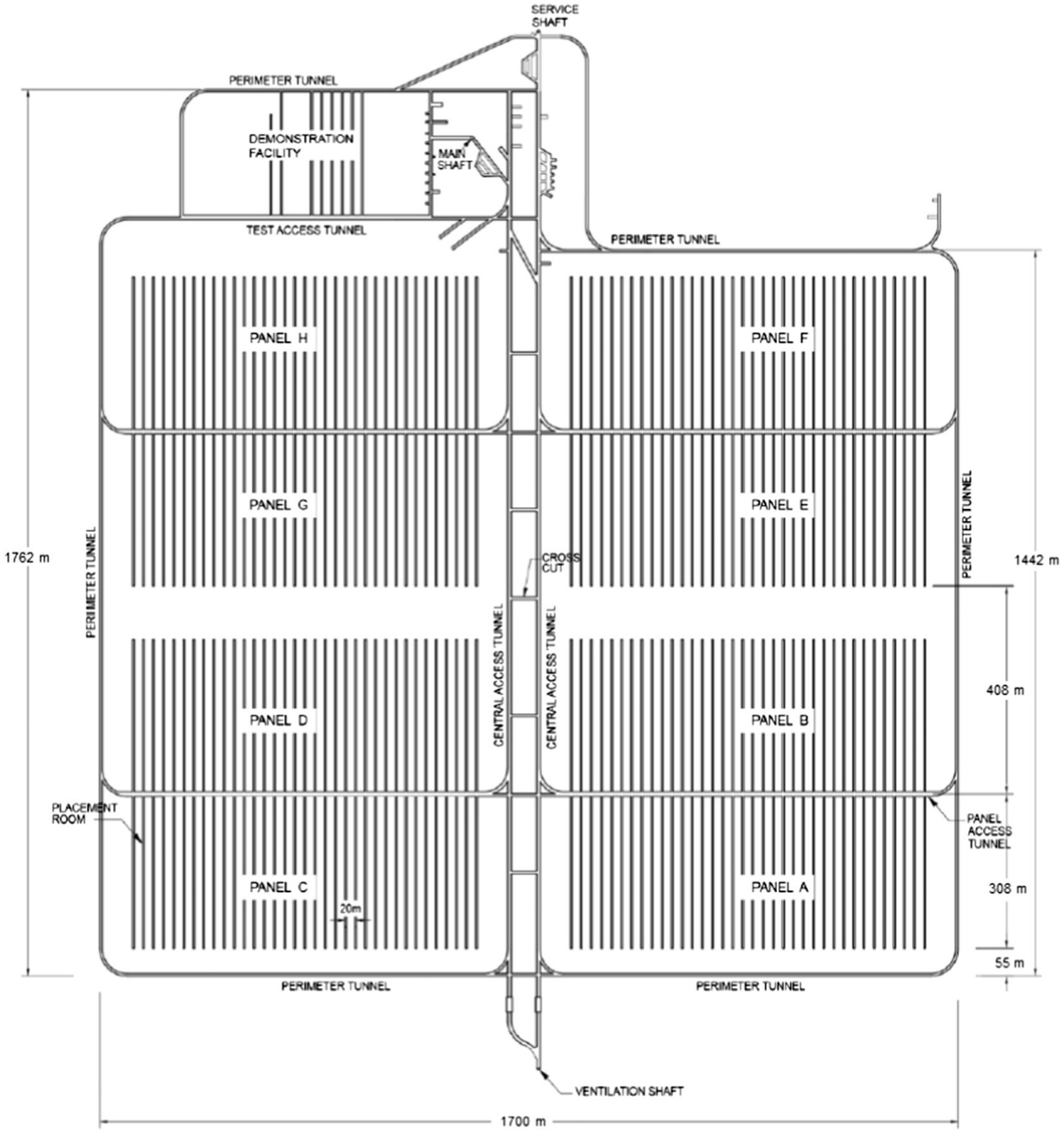

Figure 2.1: Underground layout of a crystalline rock DGR for 4.6 million used nuclear fuel bundles [8]

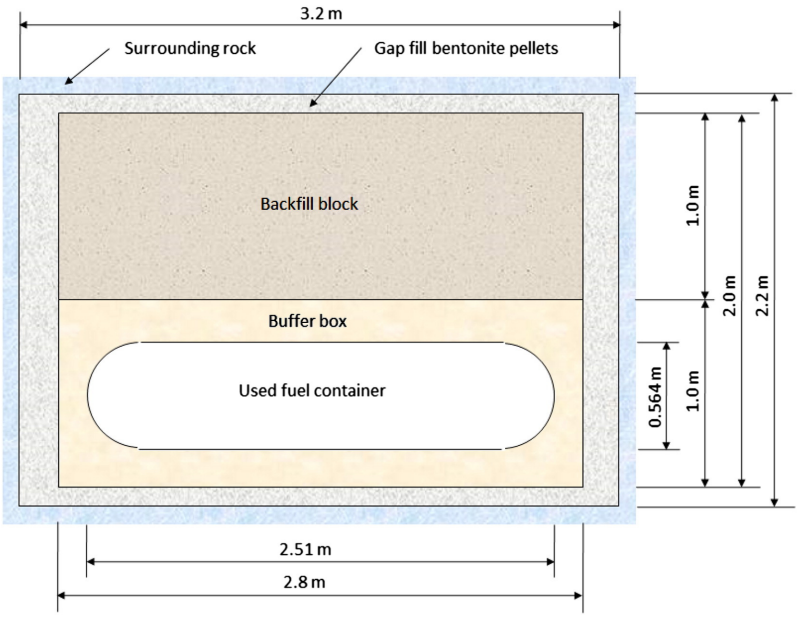

Figure 2.2: Front view of placement room geometry [29]

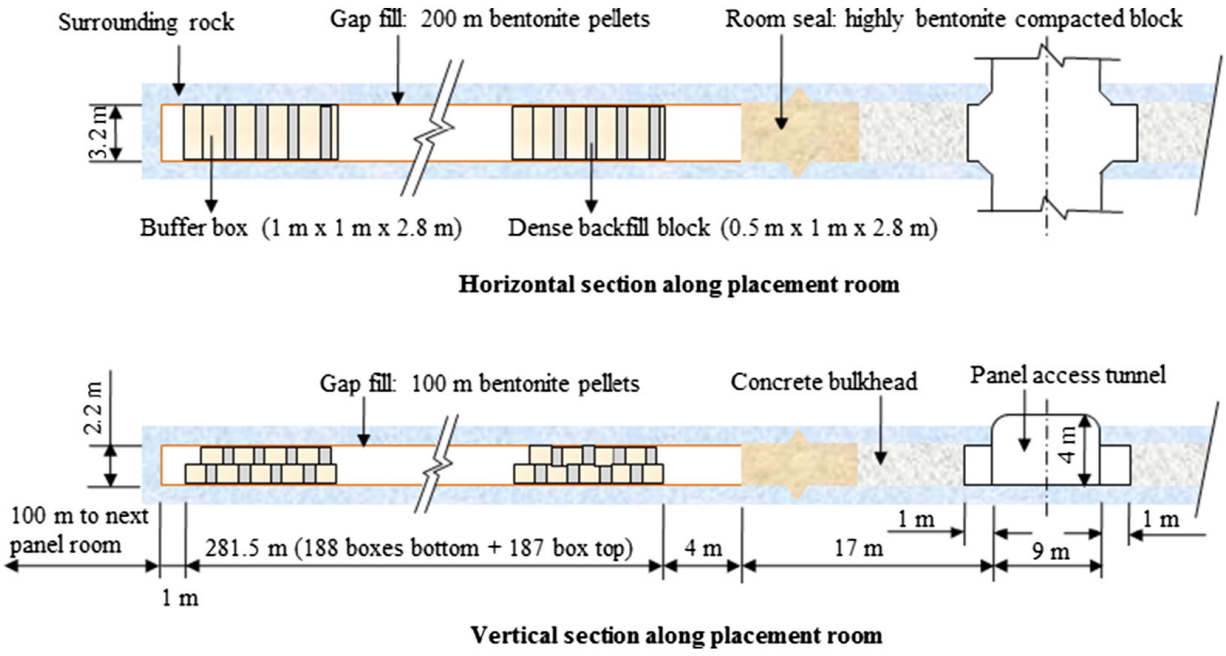

Figure 2.3: Top and side views of placement room geometry [29]

2.1.2 Near-Field and Far-Field Modelling

Guo's method for obtaining accurate thermal evolution results began with developing near and far-field models of the DGR in COMSOL Multiphysics 5.1. The simulation period was one million years as that is the time it takes for irradiated uranium fuel to return to natural radioactivity levels.

Near-Field Model

For near-field modelling, Guo constructed a rectangular model in detail to include the small yet important repository components, e.g., UFCs, buffer boxes, spacer blocks, gap-fill, and host rock. The near-field model was simplified into an infinite repository using symmetries in the xz- and yz-planes, i.e., adiabatic boundary conditions were applied to the four rectangular faces lying in those planes. The assumptions of a constant ground surface temperature of 5 °C (representing the average Canadian Shield temperature) and a geothermal gradient of 0.012 °C/m were used [23]. Also, to ensure that the depth of the host rock modelled did not influence the thermal results, Guo extended the host rock depth down to 10 000 m. In this way, the two remaining faces in the xy-plane were given isothermal boundary conditions of 5 °C (top) and 125 °C (bottom) and the initial temperature of the whole domain varied linearly (0.012 °C/m) between these two temperatures. Figure 2.4 shows the geometry and boundary conditions of the described near-field model. The model in the figure represents a unit cell, and due to symmetry, the overall model size was relatively small at 0.75 m × 10 m × 10 000 m (when compared to the far-field model to be reviewed next).

Temperature profiles from Guo's near-field model simulation at various points inside the unit cell are given in Fig. 2.5. The results indicate that the surface temperature of the UFCs (e.g., Point T) is the greatest in the DGR and that the maximum surface temperature for the parameters studied was 84 °C, occurring at about 45 years after UFC placement.

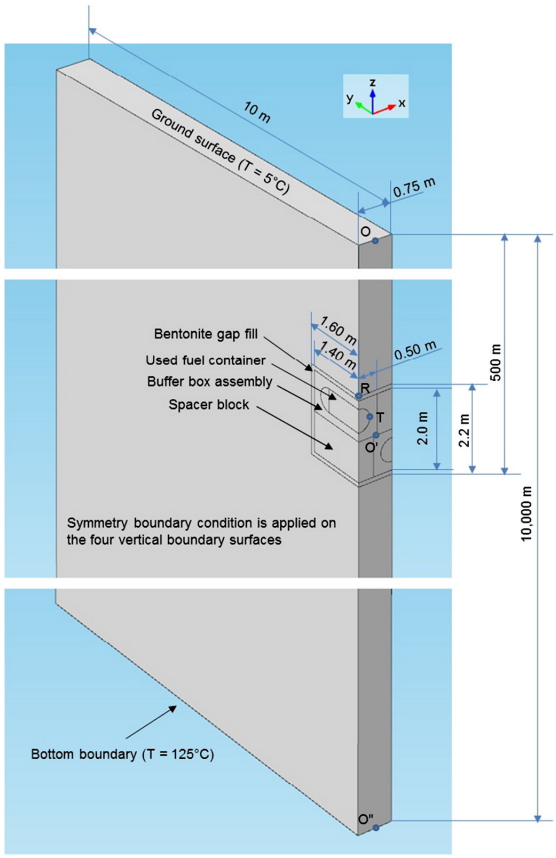

Figure 2.4: Near-field model geometry and boundary conditions [29]

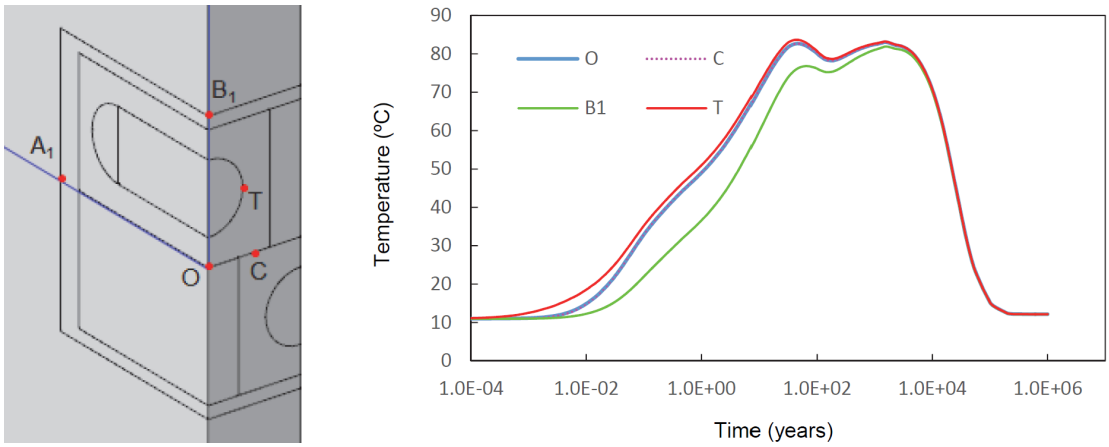

Figure 2.5: Near-field model results at various locations [28]

Far-Field Model

The repository outlined in Fig. 2.1 has 284 rooms divided into eight panels, each with 375 buffer boxes. To be conservative in terms of estimating a maximum temperature, Guo assumed each panel would consist of 36 rooms instead of the fewer 35 rooms. For the far-field model, the many details inside the placement rooms were omitted and were collectively replaced with 2 m thick panels of equivalent heat-generating material. Symmetry was used again for model simplification; thus, a far-field model that represented a quarter of the entire repository (two of eight panels) with the same boundary and initial conditions as the near-field model was created. The overall far-field model size was 6000 m × 6000 m × 10 000 m and the choices of 6000 m in both the x- and y-directions were such that the thermal responses at the host rock boundaries remained unaffected by the presence of the DGR during the simulation period. Figure 2.6 and 2.7 outline the geometry of the described far-field model.

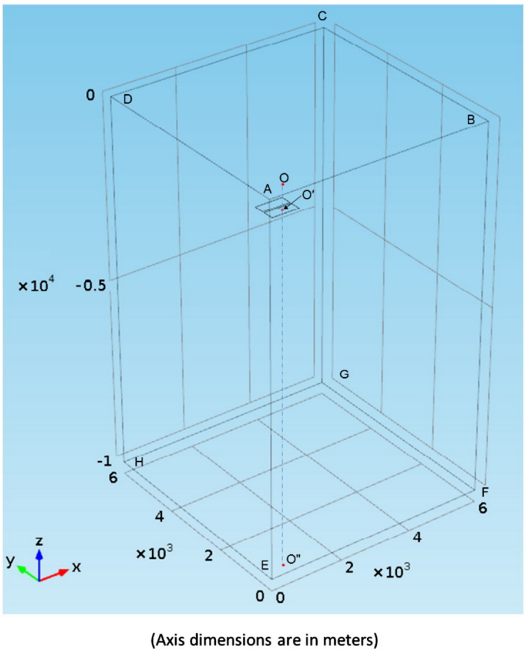

Figure 2.6: Far-field model geometry [29]

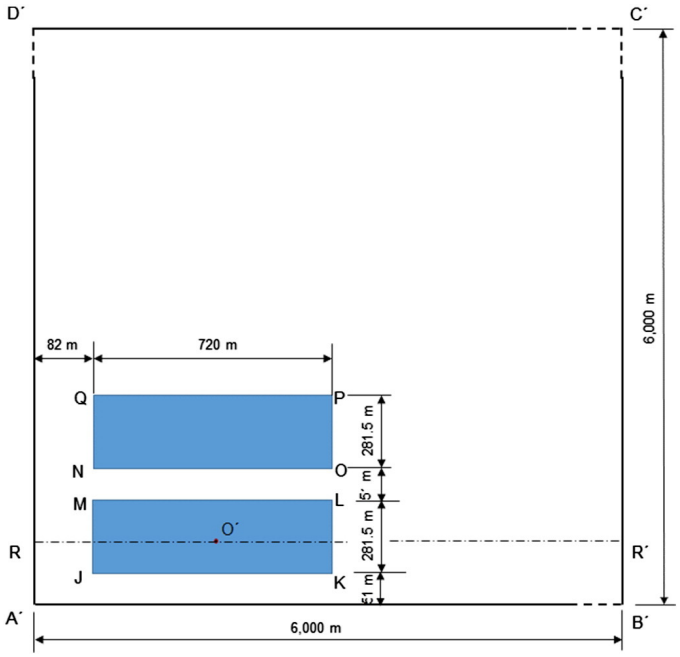

Figure 2.7: Section view of far-field model geometry at a depth of 500 m [29]

Fig. 2.8 shows the temperature profiles at different points of the far-field model. Guo also plotted the temperature profiles at several depths along the vertical line that passed through the centre of the repository in Fig. 2.9.

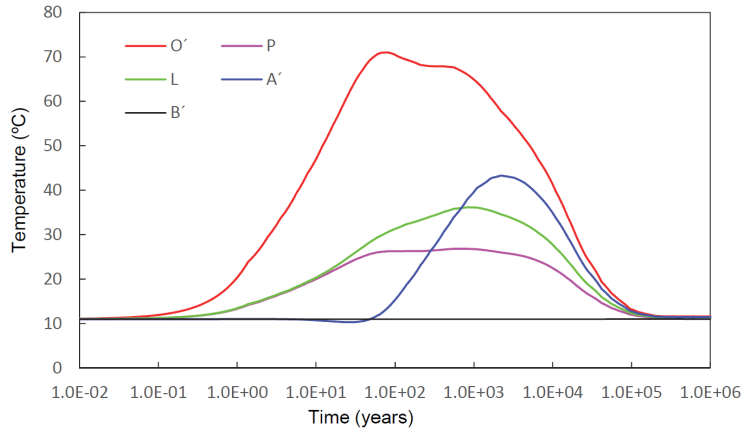

Figure 2.8: Far-field model results at various locations† [28]

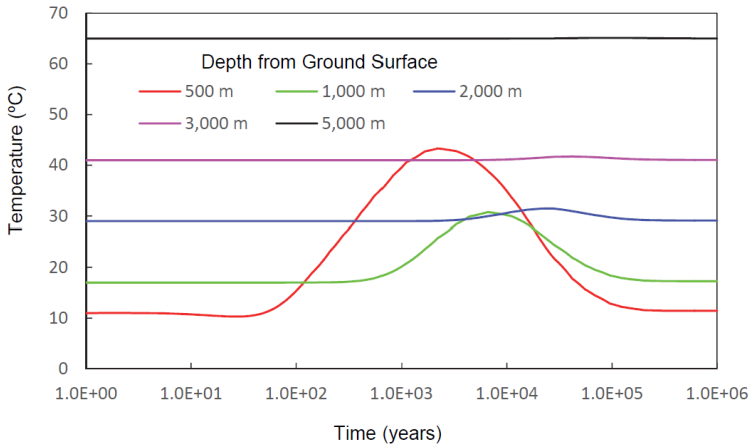

Figure 2.9: Far-field model temperatures along the repository centre [28]

The first figure identifies that the maximum temperature from the far-field model was 71 °C, occurring in the centre of the inner panel (Point O′ in Fig. 2.7) at about 78 years after placement of the UFCs. The maximum temperature here as compared to the near-field model result was lower because the far-field model determined the *average* temperature

†Refer to Fig. 2.7 for the locations of Point O′, P′, L′, A′, and B′.

inside the placement rooms. The latter figure was used to determine if the modelled depth of 10 000 m was sufficient for the thermal results to be uninfluenced by the extent of the host rock modelled. Since there was essentially no temperature change at 5000 m, the modelled depth of 10 000 m was deemed more than adequate.

2.1.3 Modified Near-Field Temperature

If the near and far-field results respectively in Fig. 2.5 and 2.8 are compared, it can be seen that the temperature profile peaks twice for the near-field model but only once for the far-field model. Guo attributed the second peak seen in the near-field results to the influence of the adiabatic boundary conditions applied in the model. With the presence of the adiabatic boundary conditions, the thermal evolution in the near-field model was due to contributions from the true repository heat load (Q_1 of Fig. 2.10a) and a nonexistent heat load from the area beyond the repository (Q_2 of Fig. 2.10b) as well. Thus, a *modified* temperature profile that would exclude the contribution from the nonexistent heat load was desired by Guo.

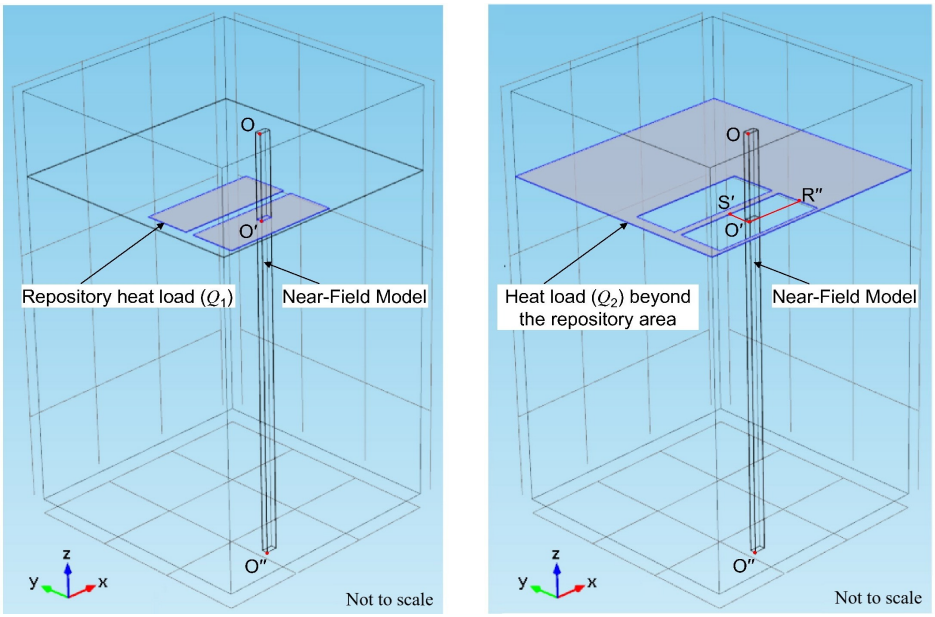

(a) True repository heat load, Q_1

(b) Heat load due to adiabatic boundary conditions, Q_2

Figure 2.10: Heat load contributions in the near-field model [29]

The desired modified temperature profile corresponding to the near-field model was denoted as $T_0 + \Phi_1$, comprising an initial temperature term (T_0) and a temperature rise term (Φ_1). The adiabatic boundary conditions that caused the presence of the nonexistent heat load induced an extra temperature rise represented as ΔT, meaning the actual near-field modelling results were instead $T_0 + \Phi_1 + \Delta T$. Guo's method for obtaining the modified temperature profile involved determining ΔT first and then subtracting that from $\Phi_1 + \Delta T$, which was explained using the following PDEs [29]:

1. The temperature rise from the true repository heat load (finite repository) would be:

$$\frac{\partial \Phi_1}{\partial t} - \alpha \nabla^2 \Phi_1 = Q_1 \tag{2.1}$$

$$\Phi_1(x, y, z, 0) = 0 \tag{2.1a}$$

$$\Phi_1(x, y, 0, t) = 0 \tag{2.1b}$$

   where α is thermal diffusivity and ∇^2 is the Laplace operator.

2. The temperature rise for the infinite repository would be:

$$\frac{\partial (\Phi_1 + \Delta T)}{\partial t} - \alpha \nabla^2 (\Phi_1 + \Delta T) = Q_1 + Q_2 \tag{2.2}$$

$$(\Phi_1 + \Delta T)(x, y, z, 0) = 0 \tag{2.2a}$$

$$(\Phi_1 + \Delta T)(x, y, 0, t) = 0. \tag{2.2b}$$

3. The temperature rise from the nonexistent heat load induced by the adiabatic boundary conditions could be obtained by subtracting (2.1) from (2.2). Simplifying would give:

$$\frac{\partial (\Delta T)}{\partial t} - \alpha \nabla^2 \Delta T = Q_2 \tag{2.3}$$

$$\Delta T(x, y, z, 0) = 0 \tag{2.3a}$$

$$\Delta T(x, y, 0, t) = 0. \tag{2.3b}$$

Instead of solving for ΔT directly using (2.3), Guo determined the temperature rise caused by the adiabatic boundaries more simply by using $\Delta T = (\Phi_1 + \Delta T) - \Phi_1$. To use this equation, Guo constructed a simplified near-field model to calculate the parenthesized terms in a manner that was comparable to the earlier far-field model, which gave the last term of the equation. The simplified near-field model omitted the placement room details and replaced them with a 0.75 m $\times$ 10 m $\times$ 2 m thick section of heat-generating material having the same heat density as that used in the far-field model. This ensured similar heat loads between the two models. Figure 2.11 gives the dimensions of the simplified near-field model, which represents a unit cell in the centre of a panel like before.

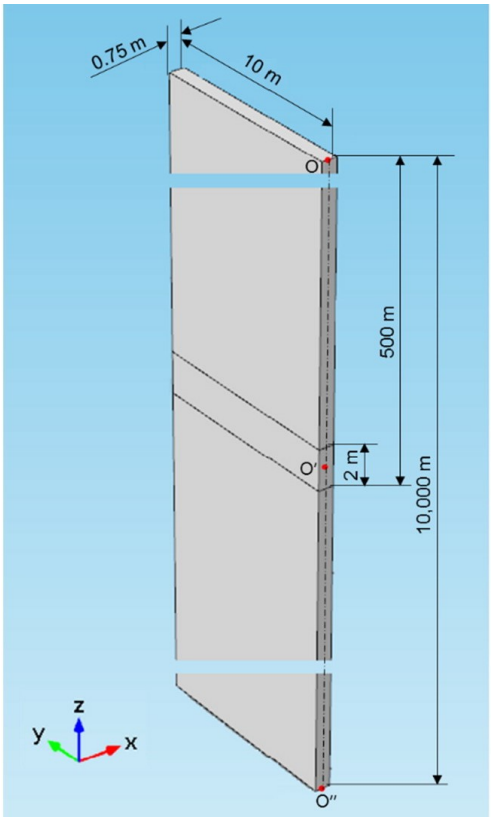

Figure 2.11: Simplified near-field model geometry [29]

Carrying out the simulation, Guo compared the average temperature profiles at the centre of a panel for the infinite repository (simplified near-field model) and the finite repository (far-field model) in Fig. 2.12. The difference between these two temperature profiles was the previously discussed and desired ΔT (at 500 m depth). Having quantified ΔT, the modified

temperature profile at the surface of a UFC was calculated and is presented in Fig. 2.13. Guo noted that the modified temperature profile was validated against a theoretical solution produced using HOTROK [23]—a program that can analytically determine the thermal evolution inside a DGR [20].

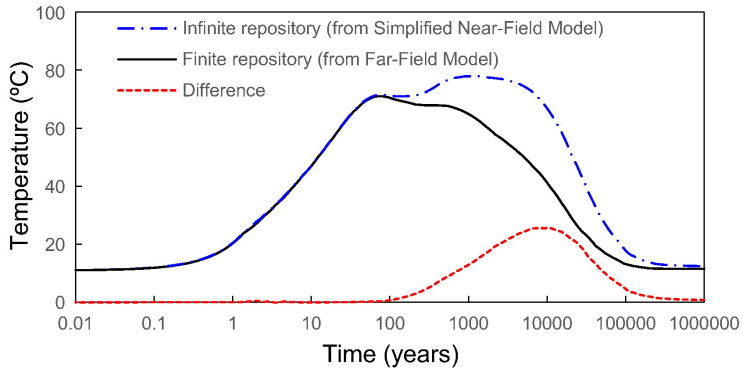

Figure 2.12: Panel centre (Point O′) temperatures from the simplified near-field model and far-field model[‡] [29]

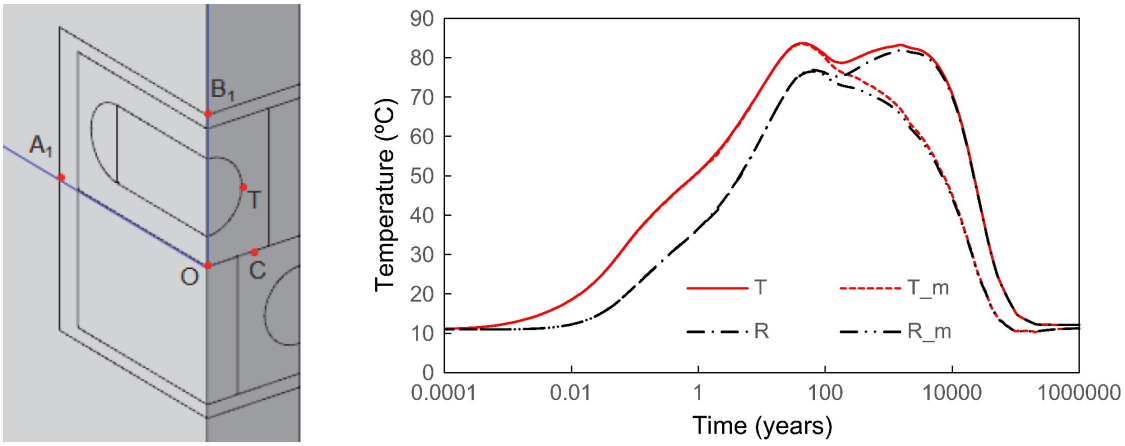

Figure 2.13: Unmodified (T) and modified (T_m) UFC surface temperatures [29]

[‡]Refer to Fig. 2.7 and 2.11 for the location of Point O′.

The modified temperature profile (red, dashed line) in Fig. 2.13 shows that the UFC surface temperature peaks once instead of twice as in the unmodified temperature profile (red, solid line). Under Guo's model specifications, the maximum of the modified temperature profile in the figure occurred at about 45 years after UFC placement. For comparison, the second peak of the unmodified temperature profile occurred at 1550 years. It is important to note that the single peak of the *modified* temperature profile matched the first of the two peaks seen in the *unmodified* temperature profile; they are essentially the same in Fig. 2.13. As well, since the heat output of UFCs decreases over time (recall Fig. 1.2), we can be sure that the single peak of the modified temperature profile (or the first peak of the unmodified temperature profile) was indeed the maximum temperature evolved inside the modelled DGR. This key observation indicates that if finding the maximum surface temperature of the UFCs is the only interest and an *unmodified* temperature profile is to be used, simulating a short portion of the DGR's lifespan is sufficient. The simulation period only needs to be long enough such that one peak in the temperature profile occurs, and that will be the maximum temperature evolved. Because the two peaks occur far apart (about 1500 years), the second peak should be not realized if an appropriately short simulation period is chosen. Therefore, the simulation period of one million years can be reduced by several orders of magnitude. This advantage saves computation/CPU time when using computationally expensive software such as COMSOL and is especially valuable for optimization studies.

2.1.4 Other Deep Geological Repositories

The earlier subsections introduced NWMO's conceptual DGR within a crystalline rock environment and Guo's method for determining the thermal evolution inside the repository by differencing the influence of adiabatic boundary conditions from the thermal response of an infinite repository model. For completeness, we now briefly review a few other thermal calculation methods employed by other international organizations/researchers studying the final disposal of used nuclear fuel here. Unlike NWMO's horizontal, two-layered placement of capsule-shaped UFCs in bentonite buffer boxes that are then stacked into placement rooms (recall Fig. 2.3), the following methods described have been utilized to study repositories that place UFCs vertically into cylindrical deposition holes/boreholes lined with bentonite along parallel tunnel floors. An example is shown in Fig. 2.14, which is the Swedish Nuclear Fuel and Waste Management Company's KBS-3 method. Despite the differences in container layout, we can review their approaches as applied to finite-sized repositories nonetheless.

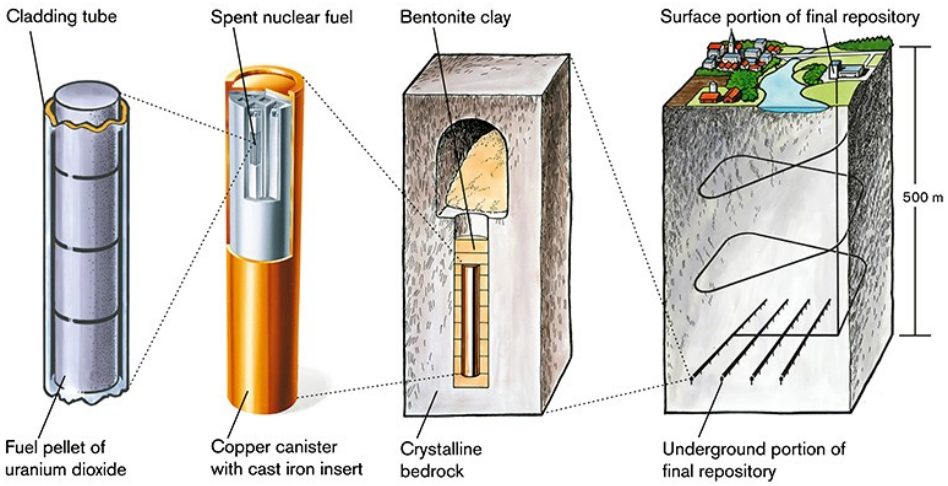

Figure 2.14: KBS-3 method for containing and isolating used nuclear fuel in deposition holes [30]

Park et al. [24] of the Korea Atomic Energy Research Institute demonstrated the use of a *simple large model* in ABAQUS to calculate the thermal evolution for a DGR with a finite number of UFCs. The development of the simple large model first needed the construction of a *detailed basic model* describing one unit cell within the placement tunnels. This model represented the geometries of the repository components well as it contained a large number of mesh points; its results were considered reliable. With the detailed basic model constructed, a *simple basic model* that ignored geometrically insignificant components and replaced others with rectangular elements was made next to reduce the number of mesh points in the model. This simple basic model was optimized to produce similar temperature results as the detailed basic model using the fewest possible mesh points. Note that both the detailed and simple basic models would act as infinite repositories as they would be solved using adiabatic boundary conditions. Finally, the simple large model was built from many simple basic models to obtain a repository model containing a finite number of UFCs. Park et al. described this method as an efficient way to portray an entire repository due to it requiring the use of fewer mesh points than one would for a *detailed large model*. Since the extent of the repository was modelled, it also allowed the consideration of boundary effects at the repository level. However, the drawback was that the approach would not have scaled well due to high computational requirements and also if accurate temperatures were required, the *submodel* function in ABAQUS had to be carried out after the global model was solved.

Another method to calculate the thermal evolution inside a DGR is to use the superposition principle. An example was given by Zhou et al. [31] for the analysis of a proposed high-level radioactive waste repository in China. They first analysed a simple model of one UFC surrounded by a layer of bentonite set in host rock with the assumption that heat would be conducted radially outwards from the cylindrical container only. Through Laplace transforms, the analytical solution of the thermal evolution in the Laplace domain for this single-UFC model was determined. For obtaining the temperature profile in the time domain, numerical inversion of the Laplace domain result was then performed using the Crump method [32]. With the temperature profile for the single-UFC model available, use of the superposition principle allowed for the inclusion of the temperature effects from multiple containers. The temperature increment at any location of surrounding host rock was the sum of the temperature increments induced by all the UFCs in the studied repository. To get the surface temperature of a UFC centred in the repository, where the maximum temperature would occur should all UFCs be identical, Zhou et al. summed the initial host rock temperature, the temperature increase of the host rock at the bentonite-rock interface, and the temperature change across the bentonite layer together. Although superposition was used successfully, a possible limitation may be the loss of accuracy due to the oversimplification of the heat transfer process beyond the first layers of the container, bentonite, and host rock. The heat from a central UFC conducted radially outwards should repeatedly pass through bentonite, host rock, another layer of bentonite, and then a neighbouring container. However, a starting model of a single UFC using the method described by Zhou et al. might ignore these details and instead have the remainder of the modelled domain be replaced with infinite host rock in order to arrive at a more straightforward analytical solution.

Hökmark and Fälth [33] also demonstrated the use of superposition for the analysis of the Swedish KBS-3 repository. In their analysis, the temperature increase at the bentonite-rock interface was calculated as the superposition of the solutions that were generated by many point, line, and compound line heat sources. The compound line sources combined two line sources of different powers and heights and were capable of better representing the larger heat fluxes experienced at the ends of cylindrical UFCs than individual line sources. Likewise, line sources would represent cylindrical containers better than point sources. For simplification of their model, Hökmark and Fälth represented the UFC centred in their repository being analysed (most unfavourable location) and its two neighbours using compound line sources. The further neighbours were substituted with line sources and then point sources. Even further away, entire tunnels were replaced with more line sources.

2.2 Surrogate-Based Analysis and Optimization

Computer models and simulations are frequently used when studying complex physical phenomena—including heat transfer problems like in this thesis and specifically in regard to the temperature constraint. As engineering design problems dealing with these physical phenomena become increasingly complex, there exists a dependence on computer-aided design and the use of numerical simulations for evaluating such problems. Since theoretical/ analytical models are not usually available for a given design problem, simulation-driven design and design optimization need to be employed. We can consider nonlinear optimization problems of the general form:

$$\begin{aligned} \min_{\boldsymbol{x}} \quad & f(\boldsymbol{x}) \\ \text{s.t.} \quad & \boldsymbol{x} \in R_A \end{aligned} \tag{2.4}$$

where $f(\boldsymbol{x})$ is the objective function to be minimized evaluated at the design variable vector $\boldsymbol{x}$, and R_A denotes the feasible region. Usually, in engineering problems, we have [34]:

$$f(\boldsymbol{x}) = U(\boldsymbol{R}_f(\boldsymbol{x})) \tag{2.5}$$

where $\boldsymbol{R}_f$ is the system response vector and U is defined through a norm that measures the distance between $\boldsymbol{R}_f$ and a target vector $\boldsymbol{y}$. Concerning simulation-driven design and design optimization, the system response vector $\boldsymbol{R}_f$ is obtained through running computer simulations and the models used are referred to as high-fidelity or fine models [34]. For simplification, f itself is regarded as the high-fidelity model altogether.

In terms of solving (2.4), it is impractical to directly use high-fidelity models with traditional optimization techniques for several reasons. High-fidelity models are computationally expensive to run, and due to limited resources (most notably time), there are restrictions on the total number of evaluations possible. As well, objective functions coming from computer simulations are often black-boxes and analytically intractable (i.e., discontinuous, non-differentiable, or inherently noisy) [34]. For tackling black-box optimization problems, there are heuristics (e.g., evolutionary algorithms, simulated annealing, and tabu search) and derivative-free methods (e.g., directional direct-search, simplicial direct-search, and trust-region algorithms). However, some of the methods in these classes may be undesirable. They can require a significant amount of evaluations, making them better suited for compact domains. Moreover, they may even lack mathematical convergence guarantees and fail to converge to global optimums should certain assumptions/conditions not be met [35–41].

Surrogate-based methods are a group of methods that appear to be successful in overcoming the difficulties discussed. These methods iteratively approximate objective functions (black-box functions) globally and use them to search for optimum solutions [35]. By so doing, surrogate-based methods offer a balance between exploration and speed, making them desirable methods for optimization problems. This section reviews the concepts and methodologies regarding SBAO, and it also introduces a MATLAB toolbox specifically for surrogate modelling, which will be useful in this thesis. SBAO will be used for approximating the maximum temperature inside the DGR as a function of UFC spacing, room spacing, and UFC age.

2.2.1 Surrogate-Based Methods

Surrogate-based methods are composed of three iterative phases—namely design, model, and search. Vu et al. [35] outlined the optimization algorithm as follows:

Phase 1 The design is initiated (iteration $k := 0$) by selecting and evaluating a set of initial points, $\boldsymbol{S}_0$, using a high-fidelity model.

Phase 2 Using the available data, $\{(\boldsymbol{x}, f(\boldsymbol{x})) \mid \boldsymbol{x} \in \boldsymbol{S}_k\}$, a surrogate model, s_k, is constructed or refined.

Phase 3 The set of next iteration points are identified using s_k and then evaluated using the high-fidelity model.
Should prescribed stopping criteria not be met, the process is repeated from Phase 2 ($k := k + 1$) after updating $\boldsymbol{S}_k$ with the new information.

In the design phase (Phase 1), the set of initial points selected and then evaluated are spread over the domain of interest (design space) in order to try understanding the global behaviour of the black-box function. The model phase (Phase 2) employs computationally cheap surrogate models to approximate the black-box function (high-fidelity) given the data available. Finally, the search phase (Phase 3) uses information from the surrogate model to find which point(s) should be evaluated in the next iteration if stopping criteria are not satisfied. Koziel and Leifsson [42] summarized these steps more simply using a flowchart in Fig. 2.15. The three phases are reviewed in more detail in the following subsections.

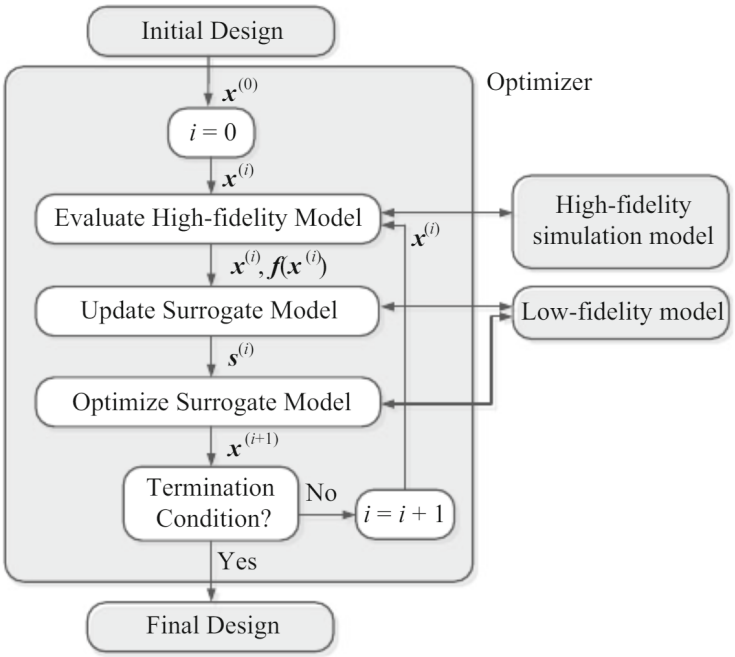

Figure 2.15: Surrogate-based optimization process [42]

2.2.2 Design of Experiments

Selecting an initial set of design points for evaluation is referred to as design of experiments (DOE), and it is a strategy for allocating the points in a manner that captures the most amount of information about the design space [34]. There are two key conditions for good experimental design [35, 43]:

Space-Fill Design points should be evenly distributed over the design space.

Non-Collapseness If it is not known which design variables are important beforehand, the design points should not have any common coordinate values.

The first requirement aims to explore the entirety of the design space if no prior knowledge about the behaviour of the objective function is available. The latter avoids evaluating similar points which would arise when there are design variables that have inconsequential influences on the objective function. Design points that only differ in these variables should not be used as they can be considered the same points.

It is beneficial to have space-filling designs as they can improve interpolation methods (which are used for constructing surrogates) [44]. Unfortunately, designs with good space-fill are often also collapsing; thus, there is a trade-off between these two requirements [35]. This is seen with classic DOE techniques like factorial designs and their alternatives (e.g., full, fractional, central composite, star, and Box-Behnken) that are certainty space-filling, yet they fall short of being non-collapsing. They do not search over the entire design space, are very collapsed, and even require evaluations that are exponentially proportional to the number of design variables. Focusing on space-filling and non-collapsing designs, they can be grouped into geometrical or statistical designs [35]. One of the most popular geometrical designs in literature—and the one to be used in this thesis—is Latin hypercube design (LHD) [45].

An LHD is one that is obtained through Latin hypercube sampling (LHS). This sampling technique selects n sample points by first dividing the design space into a set of cells. For m design variables (dimensions), each of the axes is split into n equal bins so that the design space will contain n^m cells. The design is then determined by randomly allocating the n sample points into the n^m cells such that for all one-dimensional projections of the samples, only one is in each bin [34]. The advantage of LHS is that it ensures that each design variable is represented in a fully stratified manner, even when the objective function is dominated by a select few [45]. However, note that LHS does not necessarily result in space-filling designs. An extreme example where a two-dimensional LHD is composed of points falling along a diagonal, and thus lacking uniformity over the design space, is seen in the left portion of Fig. 2.16.

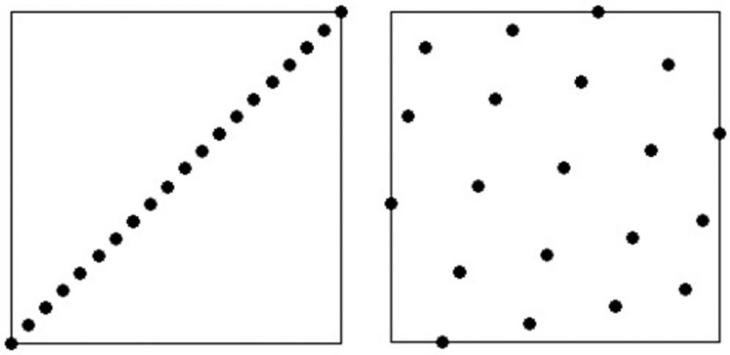

Figure 2.16: Poor versus good space-filling in a two-dimensional Latin hypercube design [35]

There are many designs on top of LHDs that offer better uniform sampling distributions. In particular, maximin distance designs have been well-studied due to their simple space-fill measure [35]. A maximin distance design finds a set of sample points where the minimum distances between all points are maximized. Formally, a design $\boldsymbol{S}^*$ having cardinality n is a maximin distance design if it solves [35]:

$$\max_{|\boldsymbol{S}|=n} \min_{\boldsymbol{x},\boldsymbol{y}\in\boldsymbol{S}} d(\boldsymbol{x},\boldsymbol{y}) \tag{2.6}$$

where $d(\boldsymbol{x},\boldsymbol{y})$ is a nonnegative function such that [46]:

$$d(\boldsymbol{x},\boldsymbol{y}) = d(\boldsymbol{y},\boldsymbol{x}) \quad \forall(\boldsymbol{x},\boldsymbol{y}) \in \boldsymbol{S} \tag{2.6a}$$

$$d(\boldsymbol{x},\boldsymbol{y}) \geq 0 \quad \text{with equality if and only if } \boldsymbol{x} = \boldsymbol{y}. \tag{2.6b}$$

The optimizations in this thesis will be carried out using MATLAB (interfacing COMSOL), and will make use of the built-in function *lhsdesign* (Latin hypercube sampling design) to generate initial sample points. For securing a set of initial sample points that will be non-collapsing as well as space-filling, the criterion for *lhsdesign* will be set to *maximin*, which uses the formulation described in (2.6). In this way, the *lhsdesign* function will iteratively try to maximize the Euclidean distance between the initial points, i.e., $d(\boldsymbol{x},\boldsymbol{y})$ in (2.6) will calculate the Euclidean distance between points $\boldsymbol{x}$ and $\boldsymbol{y}$.

2.2.3 Surrogate Functions

A number of surrogate models can be used to approximate black-box functions, and they can be constructed through parametric or nonparametric approaches. Some examples of parametric approaches are polynomial response surface modelling, moving least-squares regression, and Kriging; nonparametric examples include projection-pursuit regression and radial basis function interpolation [15, 47]. There are also approaches based on machine learning algorithms such as neural networks and support vector machines [34]. Here, we will focus on surrogate functions based on polynomial functions and radial basis functions (RBFs).

To fit polynomial functions and RBFs, the MATLAB Surrogate Model Toolbox (MATSuMoTo) will be used [48]. Developed by Müller for computationally expensive black-box global optimization problems, it includes functions for fitting to polynomial, RBF, and mixed-function surrogate models [49–52]. Some of the functions offered by Müller's toolbox will be incorporated into the SBAO of this thesis.

Polynomial Response Surface Modelling

Polynomial response surface models (RSMs) try to explain the relationship between dependent and independent variables by fitting a polynomial regression model to given data. Although they are able to provide good function approximations in local regions and are very computationally cheap to evaluate, they are unsuitable as global models for approximating highly nonlinear, multimodal, and multidimensional functions [47]. Nonetheless, polynomials are a class of well-studied functions due to their simple formulation and thus are quite popular as surrogate models.

The true polynomial RSM in m variables can be written as [53]:

$$f(\boldsymbol{x}) = \hat{f}(\boldsymbol{x}) + \varepsilon, \ \boldsymbol{x} \in \mathbb{R}^m \tag{2.7}$$

where $\hat{f}(\boldsymbol{x})$ is the r^{th}-order polynomial approximation and the independent and identically distributed random error ε follows a normal distribution with mean zero and variance σ^2. The polynomial RSM predictor is in the form:

$$\hat{f}(\boldsymbol{x}) = \beta_0 + \sum_{i=1}^{m} \beta_i x_i + \sum_{i=1}^{m} \sum_{j \le i}^{m} \beta_{ij} x_i x_j + \sum_{i=1}^{m} \sum_{j \le i}^{m} \sum_{k \le j}^{m} \beta_{ijk} x_i x_j x_k + \cdots \tag{2.8}$$

where $\boldsymbol{\beta}$ is a column vector of p coefficients. Since there are $p = \binom{m+r}{r}$ coefficients, the coefficients can be determined using a least-squares regression approach if there are $n \ge p$ sample points available. The least-squares estimator of $\boldsymbol{\beta}$ would be:

$$\underset{p\times 1}{\boldsymbol{\beta}} = (\underset{p\times p}{\boldsymbol{X}^{\mathrm{T}}\boldsymbol{X}})^{-1} \underset{p\times n}{\boldsymbol{X}^{\mathrm{T}}} \underset{n\times 1}{\boldsymbol{f}} \tag{2.9}$$

where $\boldsymbol{X}$ is a matrix whose ij element is the i^{th} observation of the j^{th} independent variable, and $\boldsymbol{f}$ is a column vector of observations. After solving for $\boldsymbol{\beta}$, the polynomial RSM in (2.8) can then be used as a surrogate model for approximating a function f with $\hat{f}$.

The number of monomials in (2.8) can be decreased if one considers a *reduced* polynomial in which interaction terms are excluded from the RSM. Doing so would lessen the number of coefficients that need to be determined, but it sacrifices the ability to account for the interactions between variables. This may be useful when m is large since coefficients corresponding to higher-order terms would likely be negligible and including them would cause overfitting. In this case, the polynomial RSM predictor takes the form [48]:

$$\hat{f}(\boldsymbol{x}) = \beta_0 + \sum_{i=1}^{m} \beta_i x_i + \sum_{i=1}^{m} \beta_{ii} x_i^2 + \sum_{i=1}^{m} \beta_{iii} x_i^3 + \cdots. \tag{2.10}$$

Radial Basis Function Interpolation

RBF interpolation uses a linear combination of simple functions to approximate more complicated functions. These functions are radially symmetrical as their values at any point depend only on the distance between that point and the origin, or any reference point defined as the *centre*. First developed in 1971 by Hardy [54] for solving equations of topography based on coordinate data, RBF interpolation can approximate functions not only with reasonable local and global accuracy but with efficiency (using limited data) as well.

An RBF is defined as any function $\psi = \psi(\|\boldsymbol{x}\|)$ where $\|\boldsymbol{x}\|$ denotes the Euclidean norm of point $\boldsymbol{x}$ from centre $\boldsymbol{c}$. Examples of some common RBFs are listed in Table 2.1.

Table 2.1: Examples of radial basis functions [47]

RBF	Formulation
Linear	$\psi(\boldsymbol{x}) = \|\boldsymbol{x}\|$
Cubic	$\psi(\boldsymbol{x}) = \|\boldsymbol{x}\|^3$
Thin-Plate Spline	$\psi(\boldsymbol{x}) = \|\boldsymbol{x}\|^2 \log\|\boldsymbol{x}\|$
Multiquadric	$\psi(\boldsymbol{x}) = (\gamma^2 + \|\boldsymbol{x}\|^2)^{1/2}$
Inverse Multiquadric	$\psi(\boldsymbol{x}) = (\gamma^2 + \|\boldsymbol{x}\|^2)^{-1/2}$
Gaussian	$\psi(\boldsymbol{x}) = e^{-\gamma\|\boldsymbol{x}\|^2}$

If n evaluated points $\boldsymbol{x}_i$ (in m variables) are treated as reference centres, the RBF interpolant of a function $f(\boldsymbol{x})$ is [55]:

$$\hat{f}(\boldsymbol{x}) = \sum_{i=1}^{n} \lambda_i \psi(\|\boldsymbol{x} - \boldsymbol{x}_i\|), \ \ \boldsymbol{x} \in \mathbb{R}^m \tag{2.11}$$

where $\boldsymbol{\lambda}$ are weights. For fixed bases such as linear, cubic, and thin-plate spline RBFs, there is one weight per basis function. Parametric basis functions such as the multiquadric, inverse multiquadric, and Gaussian RBFs can offer improved generalization properties of (2.11), but it comes at the cost of a more difficult parameter estimation process [47]. To determine the weights $\boldsymbol{\lambda}$, we can consider the following linear system:

$$\underset{n\times n}{\boldsymbol{\Psi}} \ \underset{n\times 1}{\boldsymbol{\lambda}} = \underset{n\times 1}{\boldsymbol{f}} \tag{2.12}$$

where $\Psi_{ij} = \psi(\|\boldsymbol{x}_i - \boldsymbol{x}_j\|)\ \forall(i,j) = 1,\ldots,n$. The weights can be calculated using the inverse matrix method where (2.12) is rewritten as $\boldsymbol{\lambda} = \boldsymbol{\Psi}^{-1}\boldsymbol{f}$. Obtaining the weights, the RBF interpolation in (2.11) results in a surrogate model that approximates f with $\hat{f}$ at any point $\boldsymbol{x}_*$ as:

$$\hat{f}(\boldsymbol{x}_*) = \boldsymbol{\Psi}_*^T \boldsymbol{\Psi}^{-1}\boldsymbol{f} \tag{2.13}$$

where $\boldsymbol{\Psi}_*^T = [\psi(\|\boldsymbol{x}_* - \boldsymbol{x}_1\|),\ldots,\psi(\|\boldsymbol{x}_* - \boldsymbol{x}_n\|)]$.

In certain cases, $\boldsymbol{\Psi}$ may not be positive definite and can potentially be singular, meaning the inverse matrix method cannot be applied to (2.12) [56]. RBF interpolation can overcome this by augmenting (2.11) with a polynomial tail which represents a global trend function [53, 57]. The augmented RBF interpolant is as follows [55]:

$$\hat{f}(\boldsymbol{x}) = \sum_{i=1}^{n} \lambda_i \psi(\|\boldsymbol{x} - \boldsymbol{x}_i\|) + p(\boldsymbol{x}) \tag{2.14}$$

where $p(\boldsymbol{x}) = c_0 + \boldsymbol{c}_1\boldsymbol{x} + \cdots + \boldsymbol{c}_k\boldsymbol{x}^k$ is a k^{th}-order polynomial with $km + 1$ coefficients. To obtain a surrogate model using augmented RBF interpolation, the linear system to be solved takes the form:

$$\begin{bmatrix} \underset{n\times n}{\boldsymbol{\Psi}} & \underset{n\times(km+1)}{\boldsymbol{P}} \\ \underset{(km+1)\times n}{\boldsymbol{P}^T} & \underset{(km+1)\times(km+1)}{\boldsymbol{0}} \end{bmatrix} \begin{bmatrix} \underset{n\times 1}{\boldsymbol{\lambda}} \\ \underset{(km+1)\times 1}{\boldsymbol{c}} \end{bmatrix} = \begin{bmatrix} \underset{n\times 1}{\boldsymbol{f}} \\ \underset{(km+1)\times 1}{\boldsymbol{0}} \end{bmatrix}. \tag{2.15}$$

2.2.4 Infill of Design Space

Once a surrogate model is constructed using initial data collected during DOE, the iterative surrogate optimization process can begin. The surrogate model is used to search for new points to be evaluated with the high-fidelity model, and the results are used to update the surrogate model and signal a reiteration of the search process should stopping criteria not be met. The criterion for selecting new sample points is known under different names such as *infill criterion* or *figure of merit* [58]. There are many infill criteria available such as those that use the predictor minimum, trust-region, probability of improvement, or expected improvement [47]. Here, surface-minimum sample point selection is discussed, which is one of the sampling strategies that Müller [48] presented with their MATSuMoTo toolbox.

Surface-minimum sample point selection uses the local minimum of a surrogate model as the next sample point for each iteration of an optimization process [48]. Compared to using a high-fidelity model, determining the minimum of the corresponding surrogate model is computationally cheap. If the surrogate model's minimum is too close to already evaluated

points, a point that maximizes the minimum distance to the evaluated points should be selected instead. This is done to improve the fit of the surrogate model in unexplored regions of the design space. When calculating the distances separating points, their coordinates should first be normalized to the interval $[0, 1]$ as per the bounds of each design variable. Normalization ensures that the distances are calculated using design variable values that are under a common scale. It is noted that the global minimum of a surrogate model does not necessarily need to be determined during optimization iterations. As the surrogate model is only an approximation, its minima do not necessarily match the minima of the true objective function; in fact, it is desirable to evaluate them for exploration [48].

2.3 Yield Optimization

Performance specifications are present in every engineering project, and they must be fulfilled in order to deem a project successful. These performance specifications are usually satisfied by determining nominal values for the individual project components (design variables) that make up the entire engineered system [59]. However, doing so does not consider the fact that a *real* system is being designed and analysed since uncertainty is not taken into account. Due to limited precision and inherent variability in all processes (e.g., manufacturing and construction), components in an engineered system will be produced within certain tolerances. This uncertainty signifies that the design variables are random variables and in turn, the performance of the system is a random variable as well [59]; thus, measures of system performance are not deterministic. Their values may not be those predicted from when the nominal values for the design variables are used. In this thesis, the performance specification to be met is for there to be no system failure (maximum temperature inside the DGR exceeding 100 °C).

To ensure performance specifications are met, yield optimization/maximization can be used to increase the chances that extreme values of the design variables do not lead to undesirable performance results. Yield is defined as the ratio of the number of outcomes satisfying specifications to the total number of outcomes [60]. From another perspective, it is the probability of a design meeting all of its specifications. For a vector $\boldsymbol{x}$ of m statistically varying design variables with a joint probability density function (PDF) $f_{\boldsymbol{x}}(\boldsymbol{x}; \boldsymbol{\mu}_{\boldsymbol{x}}, \boldsymbol{\Sigma}_{\boldsymbol{x}})$ where $\boldsymbol{\mu}$ and $\boldsymbol{\Sigma}$ are the mean values and covariance matrix, respectively, the yield at a nominal design point $\boldsymbol{\mu}_{\boldsymbol{x}} = \boldsymbol{X}_0$ is [61]:

$$Y = \Pr(\boldsymbol{x} \in R_A) = \int_{R_A} f_{\boldsymbol{x}}(\boldsymbol{x}; \boldsymbol{X}_0, \boldsymbol{\Sigma}_{\boldsymbol{x}})\, d^m\boldsymbol{x} \tag{2.16}$$

where $R_A \in \mathbb{R}^m$ is the acceptability/feasible region. For example, if the random variables of $\boldsymbol{X}$ are independent and uniformly distributed, the yield in (2.16) reduces to [60]:

$$Y = \frac{\mathrm{V}(R_T \cap R_A)}{\mathrm{V}(R_T)} \tag{2.17}$$

where $\mathrm{V}(R)$ is the hypervolume of region R and subscript T denotes the tolerance region. Maximizing (2.17) would determine the worst-case design.

Yield optimization can either be done by: (i) determining what the allowed tolerances on design variables are at a fixed nominal design point or (ii) determining a more robust nominal design point given the tolerances on design variables. The latter will be the yield optimization method used in this thesis. This approach to yield optimization is known as *design centring* as the goal is to find a nominal design point $\boldsymbol{X}_0$ that maximizes yield for a given distribution $f_{\boldsymbol{x}}(\boldsymbol{X}; \boldsymbol{X}_0, \boldsymbol{\Sigma}_{\boldsymbol{x}})$ [61]. To be specific, tolerances on the design variables form an m-dimensional tolerance box, and the objective is to determine the location of this box such that the probability mass of $\boldsymbol{X}$ contained inside the feasible region is at a maximum [62]. By doing so, the probabilistic centre can be found, and it will be a point that has the greatest probabilistic distances from the boundaries of the feasible region, hence yield is increased [63]. However, a difficulty that arises is that the probability distributions of random variables may be unknown prior to an optimization process. To study the yield of a design then requires assuming arbitrary distributions for component values (e.g., the worst-case design in (2.17)). To do so, Seifi et al. [17, 59, 64] presented a method consisting of three main steps for maximizing the yield of engineered systems:

1. Feasible region approximation,
2. Joint cumulative distribution approximation, and
3. Yield maximization.

These steps are reviewed in the following subsections.

2.3.1 Feasible Region Approximation

The feasible region of an optimization problem prescribed by k design specifications and design variable bounds is [64]:

$$R_A = \{\boldsymbol{x} \in \mathbb{R}^m \mid h_i(\boldsymbol{x}) \geq 0,\ i = 1, 2, \ldots, k\} \tag{2.18}$$

where $h_i(\boldsymbol{x})$ is a measure of system performance by the i^{th} constraint. The method described in this section assumes that R_A is convex, but should it be nonconvex, the problem can still be solved by repeating the calculations of the optimization process using different initial points [64]. Although the feasible region in (2.18) can directly be used for optimization, formulating a yield optimization problem having a feasible region bounded by highly nonlinear constraints is difficult. Furthermore, a feasible region may be bounded by constraints that have unknown analytical forms. For an uncomplicated problem formulation later in the yield maximization step, the feasible region described by (2.18) can be approximated using simpler boundaries.

Polyhedral Approximation

Polyhedral approximation is one method for approximating the feasible region in (2.18). This method approximates each system performance measure using a first-order approximation at an expansion point $\boldsymbol{x}^*$ as follows [64]:

$$h_i(\boldsymbol{x}) \approx h_i(\boldsymbol{x}^*) + \boldsymbol{g}_i(\boldsymbol{x}^*)^{\mathrm{T}}(\boldsymbol{x} - \boldsymbol{x}^*) \tag{2.19}$$

where $\boldsymbol{g}_i(\boldsymbol{x}^*)$ is the gradient vector of $h_i(\boldsymbol{x}^*)$. The expansion point lies on the surface of $h_i(\boldsymbol{x}) = 0$, and it will be closest to the centre of the design's tolerance box. For each constraint, this results in the minimization subproblem below [64]:

$$\begin{aligned} \min_{\boldsymbol{x}} \quad & \sqrt{(\boldsymbol{x} - \boldsymbol{x}^c)^{\mathrm{T}}(\boldsymbol{x} - \boldsymbol{x}^c)} \\ \text{s.t.} \quad & h_i(\boldsymbol{x}) = 0 \end{aligned} \tag{2.20}$$

where superscript c denotes the centre of the tolerance box. Seifi et al. [64] iteratively solved (2.20) for $\boldsymbol{x}^*$ by using the Lagrangian with a fixed-point method:

$$\boldsymbol{x}^{k+1} = \boldsymbol{x}^c - \frac{\boldsymbol{g}_i^k[(\boldsymbol{g}_i^k)^{\mathrm{T}}(\boldsymbol{x}^c - \boldsymbol{x}^k) + \boldsymbol{h}_i^k]}{(\boldsymbol{g}_i^k)^{\mathrm{T}}\boldsymbol{g}_i^k} \tag{2.21}$$

where superscripts k and $(k+1)$ are iteration indices.

After determining the first-order approximation of each constraint in the form of (2.19), the polyhedral approximation of the feasible region can be formed. The approximate feasible region is a polytope R_P specified by [64]:

$$R_P = \{\boldsymbol{x} \mid \boldsymbol{A}\boldsymbol{x} \geq \boldsymbol{c},\, \boldsymbol{x}^L \leq \boldsymbol{x} \leq \boldsymbol{x}^U\} \tag{2.22}$$

where the vector $(\boldsymbol{g}_i^*)^{\mathrm{T}} = [\frac{\partial h_i}{\partial x_1}, \frac{\partial h_i}{\partial x_2}, \ldots, \frac{\partial h_i}{\partial x_m}]_{\boldsymbol{x}_i^*}$ and scalar $(\boldsymbol{g}_i^*)^{\mathrm{T}}\boldsymbol{x}_i^*$ make up the i^{th} row of $\boldsymbol{A}$ and $\boldsymbol{c}$, respectively. The superscripts L and U respectively denote fixed lower and upper bounds on the design variables.

2.3.2 Distribution Approximation

The yield of a design depends directly on how its components (design variables) vary; thus, it is important to represent the probability distributions of the random variables as accurately as possible. For random variables with unknown distributions, studying the yield of their design requires assigning arbitrary distributions based on available information. If symmetrical distributions are used, the problem is similar to that described in (2.17) where maximizing yield essentially becomes a search for where the tolerance box can be located such that its overlap with the feasible region is at a maximum. This is the case as the probabilistic centre is also the geometrical centre, $\boldsymbol{X}_0$ [63].

When generalizing to asymmetrical distributions, the yield must be maximized directly instead of using the above approach. Recalling the definition of yield in (2.16), one can imagine that evaluating the multidimensional integral would be quite challenging—or even analytically impossible if the PDFs do not have closed-form cumulative distribution functions (CDFs). For that reason, Seifi et al. [17, 59, 64] used the Kumaraswamy distribution for the design variables as the distribution does have a closed-formed CDF. Specific examples are demonstrated in those sources. The Kumaraswamy distribution is a double-bounded distribution with PDF and CDF respectively as follows [65]:

$$f(x; a, b) = abx^{a-1}(1 - x^a)^{b-1} \tag{2.23}$$

$$F(x; a, b) = 1 - (1 - x^a)^b, \qquad x \in (0, 1) \tag{2.24}$$

where $x = (z - z_{\min})/(z_{\max} - z_{\min})$, $z_{\min} \leq z \leq z_{\max}$, and a and b are positive, nonzero parameters. In addition to having a closed-form CDF, the Kumaraswamy distribution can take on a variety of shapes depending on the values of its two parameters. This capability allows the Kumaraswamy distribution to approximate other distributions such as uniform, triangular, tail, and single modal distributions, even including the truncated Gaussian or beta distributions [64]. Examples of the shapes the Kumaraswamy PDF can take for various combinations of parameter values a and b are shown in Fig. 2.17.

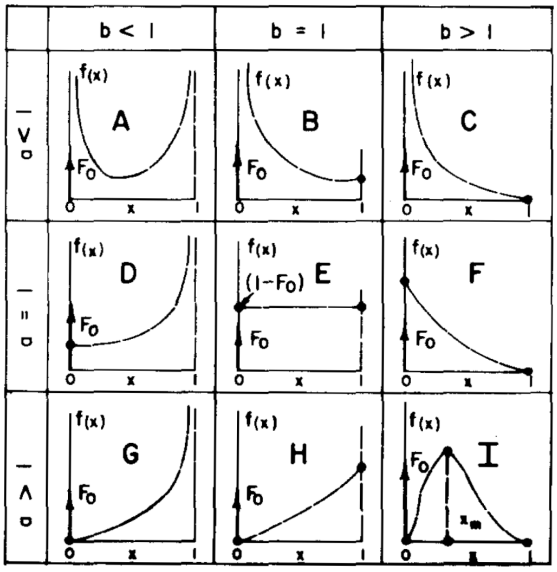

Figure 2.17: Examples of Kumaraswamy PDF shapes
for various parameter combinations of a and b [65]

2.3.3 Yield Maximization

With an approximated feasible region and representative design variable distributions, yield optimization proceeds with maximizing the yield integral described in (2.16). As mentioned, the yield must be maximized directly. This reduces the problem to finding a maximum yield box contained inside the feasible region and using the polytope R_P, the containment requirement can be written as [17, 64]:

$$\boldsymbol{A}^{+}\boldsymbol{x}^{u} - \boldsymbol{A}^{-}\boldsymbol{x}^{l} \leq \boldsymbol{c} \tag{2.25}$$

where $A_{ij}^{+} = \max\{0, A_{ij}\}$ and $A_{ij}^{-} = \max\{0, -A_{ij}\}$, and superscripts l and u denote the lower and upper bounds of the optimal maximum yield box, respectively. The maximum yield box is contained inside the design's tolerance box, which is of a given size with dimensions specified by $\boldsymbol{t}$. Locating the tolerance and maximum yield boxes in the optimization requires using three decision variables [64]:

- Reference point $\boldsymbol{x}^{r}$, corresponding to the lower bounds of the tolerance box,
- Point $\boldsymbol{x}^{l}$, corresponding to the lower bounds of the maximum yield box, and
- Point $\boldsymbol{x}^{u}$, corresponding to the upper bounds of the maximum yield box.

Altogether, the yield maximization problem is [64]:

$$\begin{aligned} \max_{\boldsymbol{x}^r, \boldsymbol{x}^l, \boldsymbol{x}^u} \quad & Y(\boldsymbol{x}^r, \boldsymbol{x}^l, \boldsymbol{x}^u) \\ \text{s.t.} \quad & \boldsymbol{A}^+ \boldsymbol{x}^u - \boldsymbol{A}^- \boldsymbol{x}^l \leq \boldsymbol{c} \\ & \boldsymbol{x}^u \leq \boldsymbol{x}^r + \boldsymbol{t} \\ & \boldsymbol{x}^r \leq \boldsymbol{x}^l \leq \boldsymbol{x}^u. \end{aligned} \tag{2.26}$$

In the case that the design variables are assumed to be independent of each other, the yield of the maximum yield box can be calculated as a product of individual probabilities. If closed-form CDFs are available for each individual parameter, the calculation is straightforward. Recall that Seifi et al. [64] used the Kumaraswamy distribution for this very reason. For example, if the Kumaraswamy distribution is used for all m design variables and independence is assumed, the yield is calculated as follows [64]:

$$\begin{aligned} Y(\boldsymbol{x}^r, \boldsymbol{x}^l, \boldsymbol{x}^u) &= \prod_{j=1}^{m} \Pr(x_j^l \leq x_j \leq x_j^u) \\ &= \prod_{j=1}^{m} \left[F_j\left(\frac{x_j^u - x_j^r}{t_j} \right) - F_j\left(\frac{x_j^l - x_j^r}{t_j} \right) \right] \\ &= \prod_{j=1}^{m} \left[-\left(1 - \left(\frac{x_j^u - x_j^r}{t_j} \right)^{a_j} \right)^{b_j} + \left(1 - \left(\frac{x_j^l - x_j^r}{t_j} \right)^{a_j} \right)^{b_j} \right]. \end{aligned} \tag{2.27}$$

Chapter 3

Finite Element Modelling

Predicting the thermal evolution inside the DGR is done by running computer simulations using the finite element analysis software COMSOL. This chapter concerns the development and validation of a COMSOL model that represents NWMO's conceptual DGR in a crystalline rock environment. The model is developed similarly to that of Guo's [29], as reviewed in the previous chapter, for comparability. By setting the design variables (and other parameters) to the values used by Guo (recall UFC spacing of 0.5 m, room spacing of 20 m, and constant UFC age of 30 years) and comparing the temperature results, the developed model is validated. This validated model is later used for SBAO in the subsequent chapter to determine optimal design points by approximating the function that represents the maximum temperature inside the DGR.

In brief, the model developed in this chapter differs from the one developed by Guo in three main ways. The first difference is that this model used half of a placement room to serve as the repeating unit of an infinite repository instead of only using a small section of a placement room as in Guo's model. A significant portion of a placement room was required to be modelled as UFC age was one of the design variables considered, meaning UFCs could be of various ages depending on their locations in the placement room. Thus, one section of a placement room may behave differently compared to another. Half the length of a placement room was modelled as UFC age was assumed to be symmetric from the middle of the room. The two remaining differences are that the depth of the host rock modelled was 5000 m as opposed to 10 000 m and that the simulation period was reduced from one million years to about 300 years. These follow the information obtained from reviewing Guo's results in Chapter 2 and helped reduce the computational requirements of the model.

COMSOL Multiphysics 5.3 was the finite element analysis software used for developing and running the computer models representing the DGR. For the COMSOL simulations in this thesis, the software ran on a machine having an Intel Core i5-3230M CPU at 2.60 GHz using two cores in one socket with 8 GB of RAM. Via LiveLink for MATLAB, COMSOL was interfaced with MATLAB for more convenient preprocessing, model manipulation, and postprocessing.

3.1 Description of the Deep Geological Repository

The repository studied was the crystalline rock DGR described in the 2016 NWMO sixth case study report [66] and its corresponding reference data report [67]. It was similar to the one studied by Guo [29] (presented in Chapter 2) except for some small modifications, primarily the distances separating Panel B/D and E/G. The newer underground layout of the DGR and a longitudinal section of the placement rooms are shown in Fig. 3.1 and 3.2, respectively. Note the directions of the coordinate system displayed in the figures for future reference. The separations between Panel B/D and E/G would now be 252.8 m instead of 100 m as before (cf. Fig. 3.1 and 2.1). The DGR would be located 500 m underground in granite rock, containing components of UFCs, buffer boxes, spacer blocks, and gap-fill. NWMO had specified that the fuel inside each UFC must have been discharged from a nuclear power reactor for at least 30 years by the time of placement into the DGR [67]. For clarity, the time since the fuel inside a UFC was discharged from a nuclear power reactor at the time of DGR placement is denoted as UFC age.

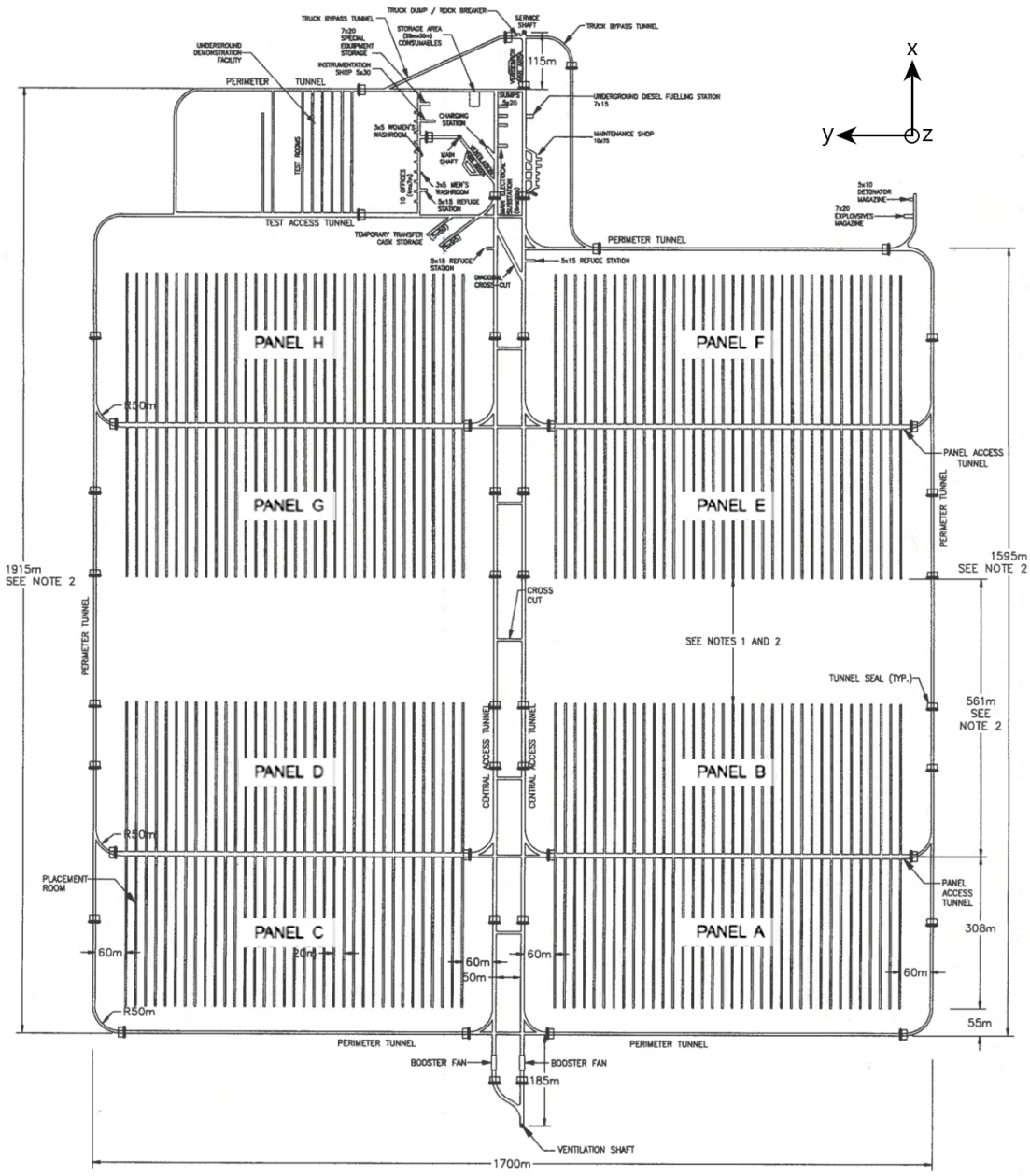

NOTES:

1. 252.8m SEPARATION BETWEEN PANELS B/D AND PANELS E/G IS BASED ON A HYPOTHETICAL LAYOUT LIMITING FRACTURE ZONE WITH THE FOLLOWING STANDOFF:
   - 100m (+10% FOR POSITION UNCERTAINTY)
   - 252.8m SEPARATION TO ACCOMMODATE CURVATURE
2. NWMO MAY ADJUST THE SEPARATION IN THE FUTURE BASED ON SITE SPECIFIC SAFETY ANALYSES.

Figure 3.1: Updated underground layout of a crystalline rock DGR [66]

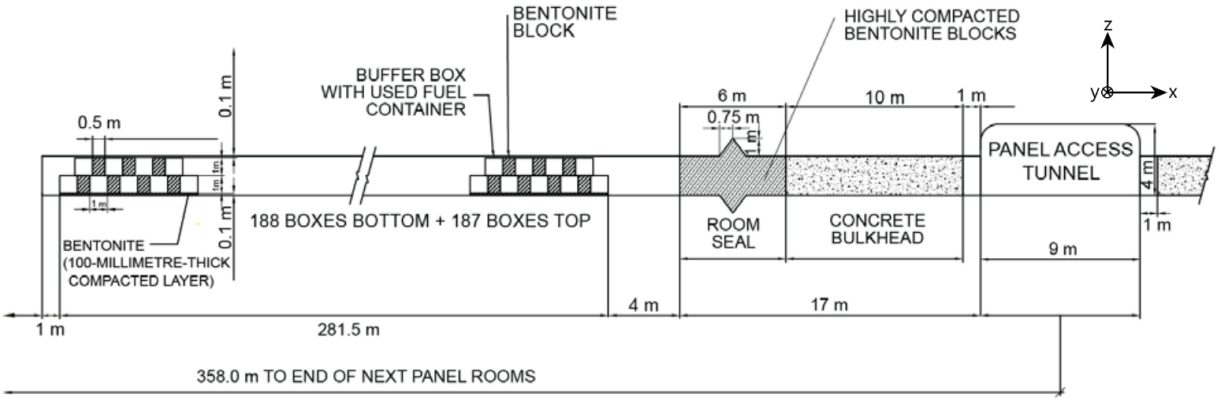

Figure 3.2: Updated side view of placement room geometry [66]

3.2 Model Development

The model here is developed using the same values for the design variables as Guo [29] to allow for comparisons in the next section. Specifically, the UFC spacing was 1.5 m, room spacing was 20 m, and all UFCs had an age of 30 years.

3.2.1 Heat Equation and Assumptions

The COMSOL model developed solved a heat conduction problem with governing equation:

$$\rho C_p \frac{\partial T}{\partial t} + \nabla \cdot \boldsymbol{q} = Q \tag{3.1}$$

where ρ is density, c_p is specific heat capacity at constant pressure, T is temperature, t is time, $\boldsymbol{q}$ is a conductive heat flux vector, and Q is a heat source term. From Fourier's law, the conductive heat flux vector is $\boldsymbol{q} = -k\nabla T$, where k is thermal conductivity. It was assumed that the thermal properties (ρ, C_p, and k) used in the heat equation, (3.1), were constant with temperature and that their corresponding materials were homogeneous and isotropic.

The host rock was assumed to be granite throughout the model domain. Any component in Fig. 3.1 and 3.2 not modelled was replaced by the host rock material. This was also done for voids so that no empty space was present in the model. Regarding UFC age, since there would be multiple fuel bundles inside each UFC, the age of the fuel inside each UFC was considered the same so that the overall age was representative of the whole container.

As the DGR would be some significant distance underground, the Earth's geothermal gradient was taken into account. It was assumed that the ground surface temperature of the DGR site would be 5 °C, and the temperature underground would increase linearly with depth at a rate of 0.012 °C/m [23].

3.2.2 Model Geometry and Boundary & Initial Conditions

Although Fig. 3.1 outlined the overall footprint of the conceptual DGR, it was disregarded here as the spatial arrangement of the UFCs was eventually optimized. The spacing design variables (specifically room spacing and UFC spacing) would determine the number of placement rooms required which in turn would affect the DGR size. What was important was the size of the placement rooms where the containers would be placed. The placement rooms modelled took on the fixed dimensions specified in Fig. 3.2. Note that from the figure, only a portion of the total length of the placement room was usable for UFC placement and that UFCs should be placed into two perfectly staggered layers. As for the components within the placement rooms, they retained the dimensions mentioned in Fig. 2.2.

Since modelling the entire DGR in Fig. 3.1 was not ideal as such a model would be very large and computationally expensive to solve, methods for reducing the model size were employed. They were as follows:

Panel/Placement Room Symmetry

The DGR was modelled as an infinite repository based on one horizontally repeating unit. Instead of considering all eight panels in Fig. 3.1, one panel could be modelled if symmetry boundary conditions were used around it in the xz- and yz-planes. Further extending the use of symmetry, one placement room could be used to represent all rooms in a particular panel if symmetry boundary conditions were used around that. The symmetry boundary conditions were applied as adiabatic boundary conditions, which took the form:

$$-\boldsymbol{n} \cdot \boldsymbol{q} = 0 \tag{3.2}$$

where $\boldsymbol{n}$ is the normal vector on the boundary.

UFC Age Arrangement Symmetry

If the UFC age arrangement were assumed to be symmetric from the centre of the placement room, the model could be reduced by half along the length of the room (x-axis). However, since the separations between Panel A/C/E/G and B/D/F/H (51 m) and Panel B/D and E/G (252.8 m) were different, the symmetry could not

be used unless another assumption was made. Thus, it was also assumed that the separations between panels at both ends of the placement rooms were 51 m. Using the smaller separation modelled the placement rooms tighter together, which would give a more conservative estimate on the maximum temperature evolved in the repository. The symmetry boundary conditions were applied similarly like before using (3.2).

UFC, Buffer Box, Spacer Block, and Gap-Fill Symmetry

The geometries of the components inside the placement room were symmetric from the centre of the room on the xz-plane, allowing the model to be halved along the y-axis. Again, (3.2) was used for applying the symmetry boundary conditions.

Domain Depth

To ensure that the depth of the host rock modelled did not influence the thermal results, Guo [29] included 10 000 m depth of host rock in their model. As revealed in Fig. 2.9, the temperature was unchanged at approximately 5000 m depth indicating 10 000 m of host rock was more than sufficient. Thus, the depth up to 5000 m was modelled.

A summary of the relevant dimensions of various parameters inside the DGR is given in Table 3.1.

So far, only boundary conditions in the xz- and yz-planes have been covered. Two remaining boundary conditions in the xy-plane would need to be specified. These would be isothermal boundary conditions applied to the top (ground surface) and bottom (modelled depth) limits of the model, and they would take on the same values as the initial temperature of the system. Based on the geothermal gradient of 0.012 °C/m and the assumed ground surface temperature of 5 °C, the initial temperature inside the DGR was expressed as:

$$T(x, y, z, t = 0) = T_0(z) = 5 + 0.012z \tag{3.3}$$

where z is underground depth in [m] and initial temperature T_0 is in [°C]. From that, the isothermal boundary conditions were 5 °C and 65 °C at the ground surface and underground depth of 5000 m, respectively.

Table 3.1: Key dimensions inside a crystalline rock DGR

Component - Dimension	Value [m]	Comment
Host Rock		
- Depth	5000	Extent of z domain modelled
Panel		
- Separation	51	At both ends
- Depth	500	Ground surface to bottom of placement room
Placement Room		
- Separation	20	
- Length	281.5	Usable length
- Width	3.2	
- Height	2.2	
Gap-Fill		
- Vertical Thickness	0.2	At sides of placement room
- Horizontal Thickness	0.1	At top and bottom of placement room
Spacer Block		
- Length	2.8	
- Width	0.5	
- Height	1	
Buffer Box		
- Length	2.8	
- Width	1	
- Height	1	
UFC		
- Length	2.514	Cylindrical body
- Radius	0.282	Cylindrical body and hemisphere caps

The COMSOL model that corresponds to the components, geometry, and boundary conditions described thus far is depicted in Fig. 3.3. Because of the fixed placement room dimensions, not every combination of room spacing and UFC spacing would fit the placement room perfectly. Hence, it was assumed that there would always be a UFC placed at the top layer of the perfectly staggered arrangement in the middle of a placement room (see Fig. 3.3b). At the ends of the placement room, extra space was filled with enlarged spacer blocks and solid HCB blocks (see Fig. 3.3c), similarly to what was described in [67].

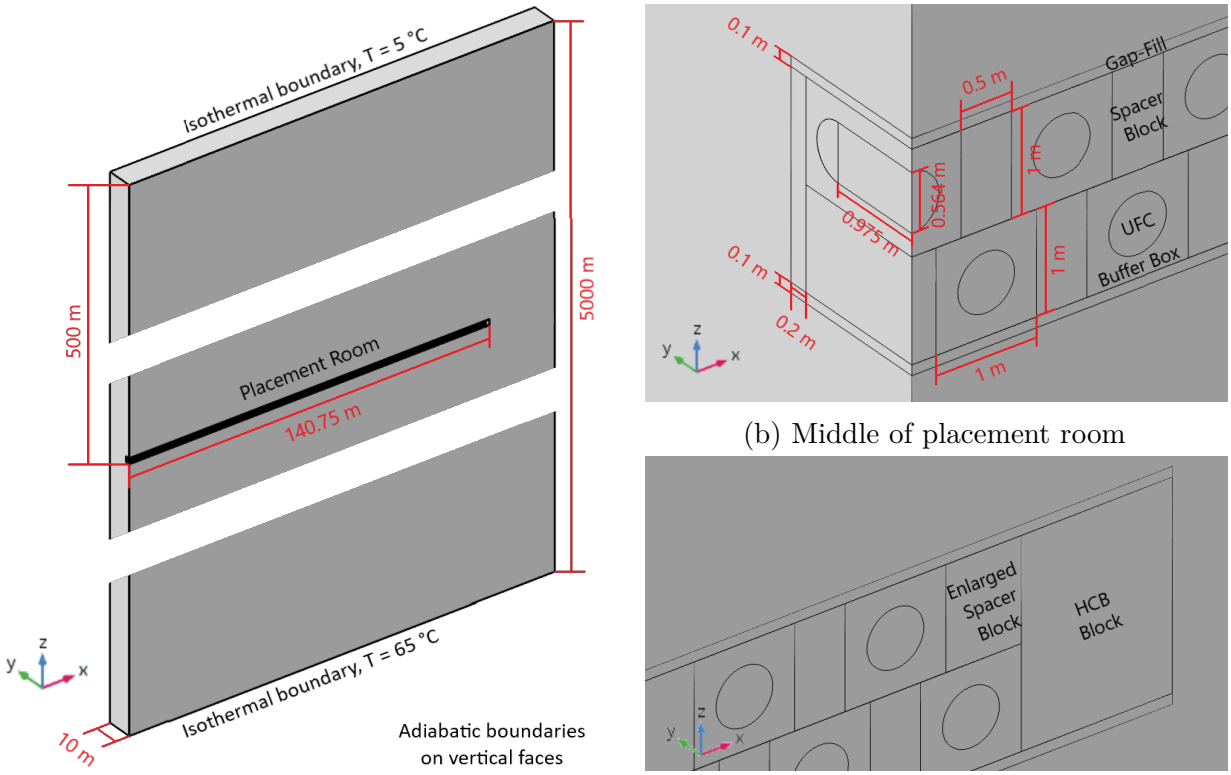

(a) Overall repeating unit

(b) Middle of placement room

(c) End of placement room

Figure 3.3: COMSOL model components, geometry, and boundary conditions

3.2.3 Material Properties and UFC Heat Load

The thermal properties of the DGR's components were required to model the thermal evolution inside the repository. The main properties required were the bulk density, thermal conductivity, and specific heat capacity of each component. The thermal properties of the UFCs and host rock (granite) used were taken from [29] while the thermal properties for the remaining materials were those specified by the reference data report of NWMO's post-closure safety assessment on a conceptual crystalline rock repository [67]. Table 3.2 summarizes these thermal properties, and they were assumed to be constant values.

Table 3.2: Thermal properties of components inside a crystalline rock DGR [29, 67]

Component	Bulk Density [$kg\,m^{-3}$]	Thermal Conductivity [$W\,m^{-1}\,K^{-1}$]	Specific Heat Capacity [$J\,kg^{-1}\,K^{-1}$]
UFC	7800	60.5	434
Buffer Box	1955	1.0	1280
Spacer Block	2276	2.0	1060
Gap-Fill	1439	0.4	870
Host Rock	2700	3.0	845

The heat outputs of the UFCs were also required for modelling the thermal evolution inside the DGR. The heat output of each UFC is a function of its age, which is in reference to the time since its discharged from a CANDU reactor. How hot and radioactive nuclear fuel is at the time of its discharge from a nuclear power reactor is dependent on its fuel burnup/utilization. When nuclear fuel is operated at higher fuel burnups, it becomes hotter and more radioactive. For the repository proposed by NWMO, the nuclear fuel at the time of placement will have been discharged from a nuclear power reactor for at least 30 years [67]. That is, the used fuel bundles will have been in wet and dry storage during that time leading up to their consolidation inside UFCs. Table 3.3 provides the heat output at different times for a UFC with fuel subjected to a typical fuel burnup, beginning at 30 years after discharge from a CANDU reactor. This data was assumed to be applicable for all UFCs placed into the DGR.

Table 3.3: Heat output of a UFC containing fuel (48 CANDU used fuel bundles) having had a burnup of 220 MWh kg_U^{-1} [68]

Time Out-of-Reactor [a]	Heat Output [W]	Time Out-of-Reactor [a]	Heat Output [W]
30	169.092	150	46.108
35	155.232	160	44.075
40	142.296	200	38.716
45	131.208	300	32.802
50	121.968	500	26.888
55	112.728	1000	18.665
60	105.336	2000	12.751
70	91.568	5000	9.240
75	85.932	10 000	6.644
80	80.850	20 000	3.844
90	72.257	35 000	2.097
100	65.327	50 000	1.321
110	59.783	100 000	0.380
135	49.988	1 000 000	0.137

3.2.4 Simulation Period

As identified in [29] in Chapter 2, the maximum temperature in the proposed repository will occur relatively near the beginning of the DGR lifespan, soon after repository closure (about 45 years). Since only the maximum temperature was of concern, the entire lifespan of the DGR did not need to be simulated. To save computation time, the simulation period used was 1e10 seconds, or approximately 300 years—significantly less than one million years (about 3e13 seconds) but enough time such that the DGR temperature would have peaked once. The time steps in seconds that were solved for followed an exponential growth, and specifically, they were at times $t = \{10^{n/20} \mid n = 0, 1, 2, \ldots, 200\}$. The choice of exponentially growing time intervals was to match the behaviour of the heat load from the UFCs (see Table 3.3), which is approximately an exponentially decaying function.

3.2.5 Mesh Refinement Study

With the appropriate material properties and heat loads assigned in COMSOL, the model constructed needed to be discretized/meshed. Given the various geometries in the DGR, tetrahedral mesh elements were used to mesh the entire domain as they offered a better fit and less element distortion compared to other mesh element types. Since the maximum temperature inside the placement room was required, and it was the location of large thermal gradients due to the heat output from UFCs, the room components used a finer mesh while the host rock adopted a coarser one. The mesh for the host rock was finest near the placement room and gradually increased in coarseness further away. An example of the meshed model is illustrated in Fig. 3.4.

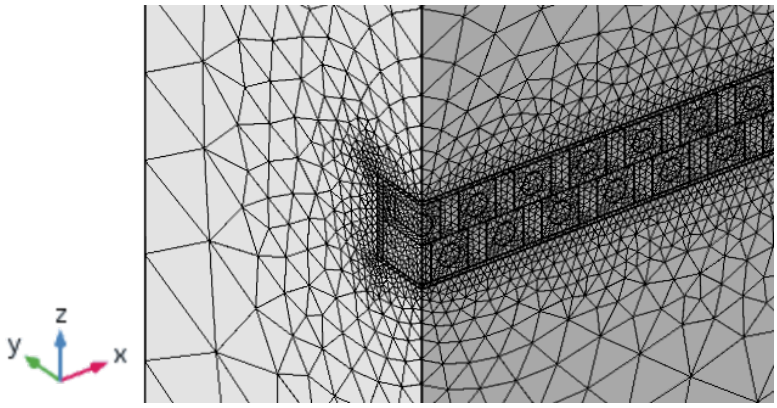

Figure 3.4: Tetrahedral elements around the middle of the placement room

As the maximum temperature was solved numerically, the choice of the mesh density directly affected the accuracy of the solution. A fine mesh would yield a more accurate result compared to a coarse mesh. To ensure that the model results were independent of the mesh used to model the DGR, a mesh refinement study was performed. In the study, the host rock's maximum element size and maximum element growth rate were respectively fixed at 50 m and 1.25 while the maximum element size for the components in the placement room was varied from 0.45 m to 0.15 m in 5 cm decrements. Decrements in the centimetre scale were selected to recognize the small geometries of the components inside the placement room, especially those of the spacer blocks (see Table 3.1) whose sizes were one of the design variables of interest. The host rock's mesh elements near the placement room scaled accordingly to the specified maximum element growth rate. Because of the model size, slight decreases in the mesh element size resulted in substantial increases

in the total number of elements and, in turn, the computational requirements as well. Due to limited computing resources, the gap-fill around the placement room was not modelled during the mesh refinement study to allow a broader exploration of element sizes. The results of the mesh refinement study are summarized in Table 3.4 and Fig. 3.5.

Table 3.4: Mesh refinement study results

Maximum Room Element Size [m]	Number of Domain Elements	Maximum Temperature [°C]	Temperature Change	CPU Time [min]
0.45	317 263	79.307	—	19.1
0.40	414 950	79.192	−0.1%	23.0
0.35	473 963	78.363	−1.0%	25.1
0.30	615 062	78.518	+0.2%	30.4
0.25	960 831	78.728	+0.3%	45.1
0.20	1 503 934	80.659	+2.5%	67.7
0.15	3 106 981	80.703	+0.1%	870.3

Results for UFC spacing = 1.5 m, room spacing = 20 m, and UFC age = 30 years. Gap-fill component not modelled. Maximum element size and maximum element growth rate of host rock fixed at 50 m and 1.25, respectively.

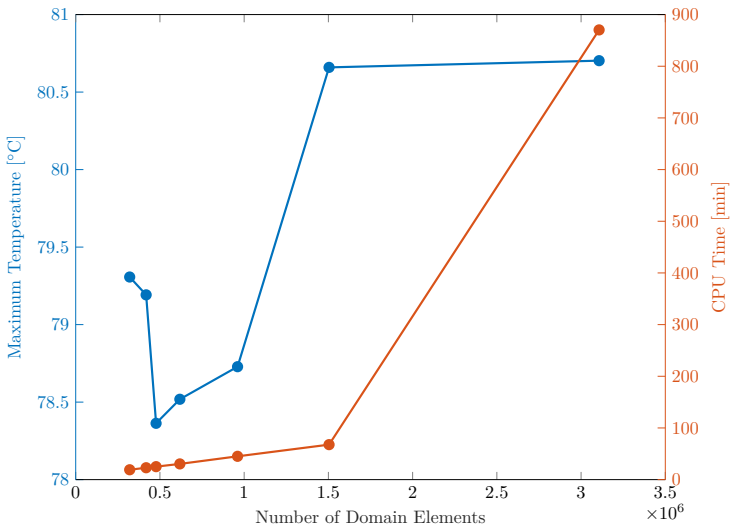

Results for UFC spacing = 1.5 m, room spacing = 20 m, and UFC age = 30 years.

Figure 3.5: Mesh refinement study results

From Table 3.4 and Fig. 3.5, the results for the maximum temperature inside the DGR are seen to vary between approximately 78 and 81 °C depending on the number of mesh elements used. Observing that the absolute percentage changes of the maximum temperature decreased as the number of mesh elements increased and that the change from the penultimate to the last result was reasonably small, it was chosen here that the placement room maximum element size be 0.20 m. The maximum element size of 0.15 m was not chosen based on the computation times seen in the last column of Table 3.4. As the maximum element size decreased, the number of mesh elements quickly grew, and thus COMSOL was required to solve for the temperature at many more mesh points. This led to increased memory usage and more mathematical operations being performed by the machine's CPU, both of which contributed to longer solution times. Seeing that the machine used could not reasonably handle solving the model built with a maximum element size of 0.15 m and how the computational requirements drastically scaled from the results obtained thus far, it was decided that placement room maximum element sizes between 0.20 and 0.15 m would not be considered. From Fig. 3.5, it was expected that the computation time would not be linearly proportional to the number of elements in the model. The model using a maximum element size of 0.20 m already required over one hour to solve. Further decreases in the maximum element size would increase the number of elements in the model, lengthening the computation time. Furthermore, additional refinement through a relative tolerance study in the following subsection would increase the computation requirements even more. For the application of the model to SBAO in the subsequent chapter where multiple evaluations would be performed, it was preferred to keep the model at a manageable state for the machine available.

3.2.6 Relative Tolerance Study

Confidence in a numerical solution can be based on the number of significant digits in the results. Determining the number of significant digits requires the error associated with the numerical solution. However, if the true value of the solution is unknown, which is the maximum temperature inside the DGR in this case, the true error cannot be calculated. For iterative/numerical methods, approximate errors are used instead. For the simulations here, the COMSOL solver allowed the specification of a tolerance on the relative approximate error, ϵ_a, which was:

$$\epsilon_a = \frac{\hat{y}_{\text{present}} - \hat{y}_{\text{previous}}}{\hat{y}_{\text{present}}} \tag{3.4}$$

where $\hat{y}$ is the iterative solution. This tolerance defined the maximum relative approximate error allowed. Given a relative approximate error, the number of significant digits is:

$$n = \lfloor -\log(2 \times |\epsilon_a|) \rfloor \tag{3.5}$$

where $\lfloor \cdot \rfloor$ is the floor function. With this, a relative tolerance study was performed on the model. Relative tolerance values decreasing from 1e−1 to 1e−4 were specified into the COMSOL solver, and the results are given in Table 3.5 and visualized in Fig. 3.6.

Table 3.5: Relative tolerance refinement study results

Relative Tolerance	Maximum Temperature [°C]	Temperature Change	CPU Time [min]
1e−1	79.054	—	67.5
1e−2	82.388	+4.2%	85.0
1e−3	84.423	+2.5%	111.0
1e−4	84.229	−0.2%	183.6

Results for UFC spacing = 1.5 m, room spacing = 20 m, and UFC age = 30 years.

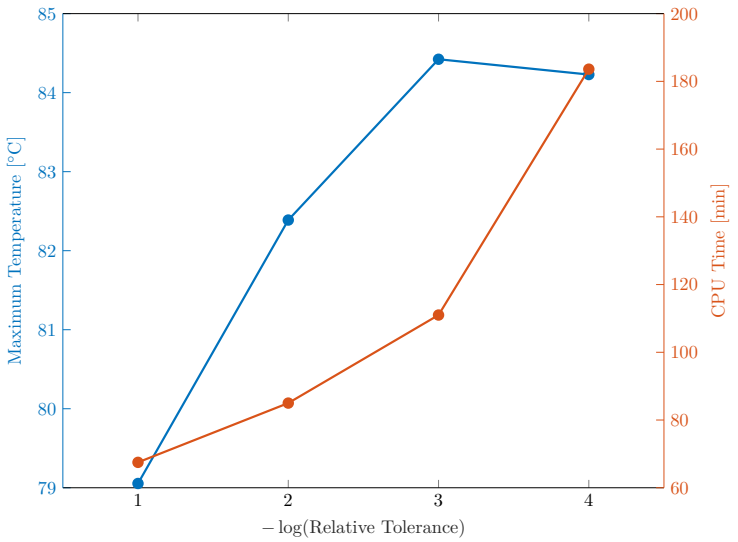

Results for UFC spacing = 1.5 m, room spacing = 20 m, and UFC age = 30 years.

Figure 3.6: Relative tolerance refinement study results

From Table 3.5 and Fig. 3.6, the maximum temperature results can be seen to vary between approximately 79 and 84 °C. There was more confidence in values corresponding to the smaller relative tolerances as using (3.5), a solution converged from a relative tolerance of 1e−4 has three significant digits compared a solution from a relative tolerance of 1e−1 having zero significant digits. It was chosen here that the relative tolerance specified for the solver be 1e−3 (corresponding to two significant digits). The smaller relative tolerance of 1e−4 was not chosen based on the increased computation times seen in the last column of Table 3.5 and the fact that the maximum temperature inside the DGR was required to be less than 100 °C. Thus, a solution with two significant digits would suffice and would be computationally cheaper to find.

3.3 Model Validation

From the mesh refinement and relative tolerance studies, the COMSOL model was finalized with maximum element size in the placement room of 0.20 m and solver relative tolerance of 1e−3. With these specifications, the COMSOL solver should take roughly two hours to solve a single simulation (see Table 3.5) using the machine described at the beginning of the chapter. In this section, the behaviour of the maximum temperature in the DGR is validated against the findings in the literature review of Chapter 2. Again, the design variables were set to a UFC spacing of 1.5 m, room spacing of 20 m, and all UFCs had an age of 30 years.

Guo [29] showed that the temperature profile inside a DGR peaks twice when modelling it as an infinite repository and once when modelling it as a finite repository (see Fig. 2.12). Moreover, the first of two peaks for an infinite repository is representative of the true maximum temperature of its corresponding finite repository (see Fig. 2.13) [29]. The evolution of the maximum DGR temperature for the infinite repository model developed is presented in Fig. 3.7. In regard to the overall behaviour, the simulation period was sufficient such that one maximum temperature peak had occurred while a second peak had yet to manifest itself. This was important and desired as the maximum of the entire plot was then representative of the maximum temperature that will occur inside the DGR over its one million years lifespan.

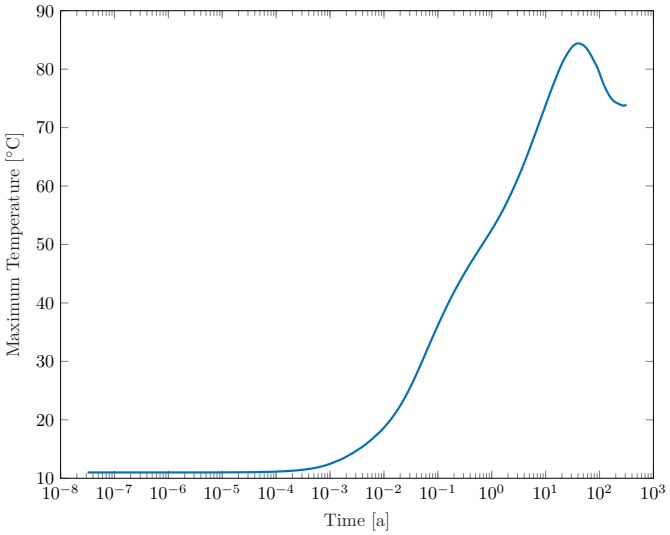

Result for UFC spacing = 1.5 m, room spacing = 20 m, and UFC age = 30 years.

Figure 3.7: Maximum temperature evolution

Observing Fig. 3.7 more closely, the maximum temperature was approximately 84.4 °C, and it occurred at about 40 years after UFC placement. For comparison, the maximum temperature reported by Guo was 84 °C occurring at about 45 years [29]. The discrepancy in the time of occurrence was likely due to the resolution of the chosen time steps (which were at times of $10^0, 10^{0.05}, 10^{0.10}, \ldots, 10^{10.00}$ seconds here). The occurrence at 40 years corresponded to $10^{9.10}$ seconds. If the maximum temperature were found to be at the next time step of $10^{9.15}$ seconds, that would correspond to 45 years and match the value found by Guo. Nonetheless, the value of the maximum temperature determined by the model agreed with previous work and could be used for optimization processes in the forthcoming chapters.

Chapter 4

Surrogate-Based Analysis and Optimization

The COMSOL model developed in Chapter 3 was a high-fidelity model for determining the maximum temperature inside the conceptual DGR. The model would then be optimized to determine combinations of values for the design variables such that the maximum temperature would be below the 100 °C constraint. In this chapter, the use of SBAO would reduce the costly computational requirements for the optimization of the high-fidelity COMSOL model by approximating the function that represents the maximum temperature inside the DGR. Recall, the maximum temperature is a function of three design variables in this thesis: (i) UFC spacing, (ii) room spacing, and (iii) UFC age. Two cases on the UFC age inventory are considered. The first case concerns UFCs that have all been discharged from a reactor for 30 years while the second case concerns assorted UFC ages. It is understood that there is a trade-off between UFC spacing and room spacing as a decrease in one should require an increase in the other if maximum temperature is to be held constant. However, it is unclear how the arrangement of variously aged UFCs affects the results. The following sections describe the SBAO process and present results for these two cases.

4.1 Problem Formulation

Feasible design points are those that result in maximum DGR temperatures that are less than 100 °C—leading to no system failure. To maximize the efficiency of the DGR, feasible design points that lead to maximum temperatures just below the temperature constraint were of interest. Finding these optimal points required solving the following optimization problem:

$$\begin{aligned} \max_{\boldsymbol{x}} \quad & T_{\max}(\boldsymbol{x}) \\ \text{s.t.} \quad & T_{\max}(\boldsymbol{x}) \leq 100 \\ & x_i^L \leq x_i \leq {x_i}^U, \quad i = 1, 2, 3 \end{aligned} \tag{4.1}$$

where $T_{\max}$ is the maximum temperature reached inside the DGR in [°C]; $\boldsymbol{x} = [x_1, x_2, x_3]$ is the design variable vector with indices corresponding to UFC spacing in [m], room spacing in [m], and UFC ages in [a]; and superscripts L and U denote lower and upper bounds, respectively.

As the maximum temperature constraint was the only constraint in the design space (excluding design variable bounds), approximating this function allowed for the determination of the feasible region for the DGR design. With that information, the optimal design points would simply be those that lie on or just below the constraint. This means that solving (4.1) could instead be done by determining the boundary that separates design points resulting in maximum temperatures over and under 100 °C. To determine this boundary, and thus the feasible region of the design space, an optimization problem was formulated such that deviations of the maximum temperature from the predefined 100 °C constraint would be minimized. It was as follows:

$$\min_{\boldsymbol{x}} \quad |T_{\max}(\boldsymbol{x}) - 100| \tag{4.2}$$

$$\text{s.t.} \quad x_i^L \leq x_i \leq {x_i}^U, \quad i = 1, 2, 3. \tag{4.2a}$$

The bounds on the spacing design variables (UFC spacing and room spacing) were chosen with consideration to the NWMO reference design for a crystalline rock DGR [67] and adopted from a study by Lin and Ponnambalam [16]. The reference design used UFC spacing of 1.5 m (corresponding to a spacer block width of 0.5 m) and room spacing of 20 m. In [16], the upper bound on UFC spacing was double that of the value used in the reference design while the room spacings explored were from half to double the reference's values. These were used in this work as well; thus, the discrete values considered for the spacing design variables were $x_1 = \{1.0, 1.1, 1.2, \ldots, 2.0\}$ and $x_2 = \{10, 11, 12, \ldots, 40\}$. Regarding UFC spacing, $x_1 = 1.0$ indicates the absence of spacer blocks and is the minimum separation due to the buffer boxes being one metre wide.

As for the bounds on the UFC age, they were based on the estimated repository operation time of about 38 years [66]. When considering the case where the inventory would be of identical UFC age, all UFCs were specified to be 30 years out of a nuclear power reactor (i.e., $x_3 = 30$), which is the minimum set by NWMO. This age specification could be considered as an absolute worst-case as all the UFCs would be at its highest allowed heat output at the time of placement into the DGR. For the case where the inventory would be of assorted UFC ages, the ages considered were $x_3 = \{k \in \mathbb{R} \mid 30 \leq k \leq 60\}$. Sixty years was chosen as the maximum UFC age instead of 68 years (due to 30 years of cooling plus 38 years of repository operation) as older UFCs output less heat, and thus more conservative results would be obtained.

4.1.1 Parameterization of UFC Age Arrangement

Having chosen that the ages of the UFCs considered range from 30 to 60 years old, another assumption had to be made regarding the UFC inventory. If the true UFC inventory was considered, then the model of a single placement room would contain a fixed number of UFCs per age as the inventory must then be distributed equally among all rooms. Investigating the arrangement of this fixed inventory would fundamentally be considering all the various permutations of the available UFCs. Instead, it was proposed here to consider various arrangements of UFC age directly with the assumption that there would be enough inventory (UFCs at each specific age) for such arrangements. This approach would allow for a wider range of inventories and their arrangements to be studied.

To specify the various inventories of the UFCs, it would be easier to redefine x_3 in (4.2a) to be a design variable that represents the arrangement of the UFC ages in the placement rooms. Specific functions could be used to represent the arrangement of the UFC ages in this case. These functions would be parameterized and bounded between the lower and upper bounds of the UFC age (30–60 years) and be defined along the modelled length of the half placement room (0 to 281.5/2 m). By changing the value of the parameter(s) in these functions, the arrangement of the UFC ages could then take on different arrangement *shapes*. If the functions are chosen such that they contain only one parameter, the number of design variables in (4.2) can remain the same, i.e., $x_3 = x_3(u; \alpha)$ where u is a position from the centre to the end of the placement room, and α is a so-called *shape parameter*. The design variables of focus would then be: (i) UFC spacing, (ii) room spacing, and (iii) the shape parameter. Just as with x_1 and x_2, the shape parameter α would take on discrete values (i.e., x_3 would be a discrete variable).

Two functions were used to represent the arrangement of the UFC ages in this thesis, namely the cosine function and the Kumaraswamy PDF. They are described as follows.

Sinusoidal UFC Age Arrangement

A sinusoidal UFC age arrangement would place UFCs in a pattern where the age oscillates between a minimum of 30 years and a maximum of 60 years. Depending on the frequency of the oscillations denoted by a parameter, the amount of relatively young or old UFCs grouped closely together would change. The cosine function was the sinusoidal function considered as it is symmetric about the y-axis—which was treated as the lengthwise centre of the placement room. The function that specified the UFC age $A_1(u)$ between 30 and 60 years at a position between the centre ($u = 0$) and the end ($u = 281.5/2$) of the placement room in metres was:

$$A_1(u;\omega) = 15\cos\left(\omega\frac{2u}{281.5}\right) + 45,\ u \in \left[0, \frac{281.5}{2}\right] \tag{4.3}$$

where ω is the number of oscillations along half of the placement room.

When the sinusoidal function was used in (4.2), the UFC age design variable was then a function of the shape parameter ω, i.e., $x_3 = x_3(u;\omega)$. The values of the shape parameter considered were limited to $\omega = \{0.5, 1.0, 1.5, \ldots, 10.0\}$ during SBAO, and Fig. 4.1 exemplifies the UFC age arrangements based on (4.3) at several values of ω. Note that while the arrangements are drawn as continuous functions in the figure, the actual arrangement of the UFC ages would be discrete as there would be a finite number of UFCs spread over the length of the room.

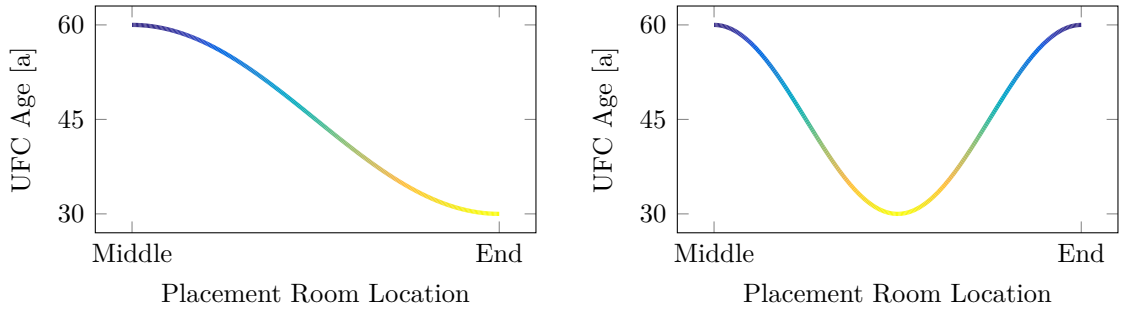

(a) Parameter: $\omega = 0.5$ (b) Parameter: $\omega = 1$

Colours imply younger UFCs generate more heat compared to older UFCs.

Figure 4.1: Examples of UFC ages arranged sinusoidally (cosine) with parameter $w \in \{0.5, 1.0, 5.0, 10.0\}$

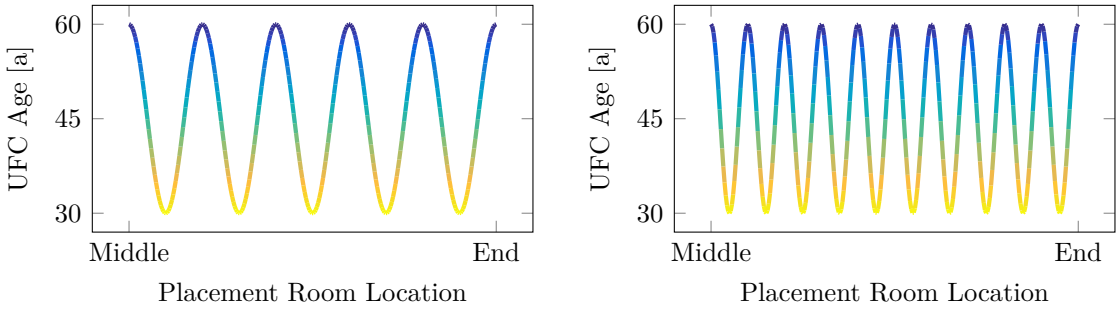

(c) Parameter: $\omega = 5$ (d) Parameter: $\omega = 10$

Colours imply younger UFCs generate more heat compared to older UFCs.

Figure 4.1: (Continued)

Kumaraswamy PDF-Like UFC Age Arrangement

The Kumaraswamy distribution was introduced in Chapter 2 and is a family of continuous probability distributions originally proposed for double-bounded random processes [65]. Recall that the Kumaraswamy PDF is defined as:

$$f(x; a, b) = abx^{a-1}(1 - x^a)^{b-1}, \ x \in (0, 1). \tag{2.23}$$

A UFC age arrangement following the shape of the Kumaraswamy PDF would be able to place UFCs in a variety of patterns. Depending on the value of its two shape parameters, $a > 0$ and $b > 0$, the Kumaraswamy PDF could take on different shapes, including those similar to uniform, Gaussian, and exponential distributions, among others. Adapting (2.23) to the problem at hand, the function shaped like a Kumaraswamy PDF that specified the UFC age $A_2(u)$ between 30 and 60 years at a position between the lengthwise centre ($u = 0$) and the end ($u = 281.5/2$) of the placement room in metres was:

$$\hat{A}_2(u; a, b) = \frac{30ab}{\max \hat{A}_2'(u; a, b)} \left(\frac{2u}{281.5}\right)^{a-1} \left(1 - \left(\frac{2u}{281.5}\right)^{a}\right)^{b-1} + 30, \ u \in \left[0, \frac{281.5}{2}\right] \tag{4.4}$$

where $\hat{A}_2'(u; a, b) = ab\,(2u/281.5)^{a-1}\,(1 - (2u/281.5)^a)^{b-1}$.

For keeping the scope of the optimization small, parameter b was kept at a constant value. With that, when the Kumaraswamy PDF was used in (4.2), the UFC age design variable was then a function of the varying shape parameter a, i.e., $x_3 = x_3(u; a)$. The constant parameter was given the value $b = 1.5$ and the values of the varying shape parameter

considered was limited to $a = \{0.25, 0.50, 0.75, \ldots, 4.00\}$ during SBAO. However, a problem that arose when using (4.4) for values $0 < a < 1$ and $b = 1.5$ was that the function tended toward infinity as $u \to 0$ (or $x \to 0$ in (2.23)). The asymptotic behaviour was avoided by mapping the interval $x \in [0.01, 1]$ to u such that (4.4) became:

$$A_2(u; a, b) = \frac{30ab}{\max A_2'(u; a, b)} \left(\frac{2(0.99)u}{281.5} + 0.01 \right)^{a-1} \times \left(1 - \left(\frac{2(0.99)u}{281.5} + 0.01 \right)^{a} \right)^{b-1} + 30, \; u \in \left[0, \frac{281.5}{2} \right] \quad (4.5)$$

where $A_2'(u; a, b) = ab\,(2(0.99)u/281.5 + 0.01)^{a-1}\,(1 - (2(0.99)u/281.5 + 0.01)^{a})^{b-1}$. Examples of UFC age arrangements based on (4.5) for various values of a are presented in Fig. 4.2.

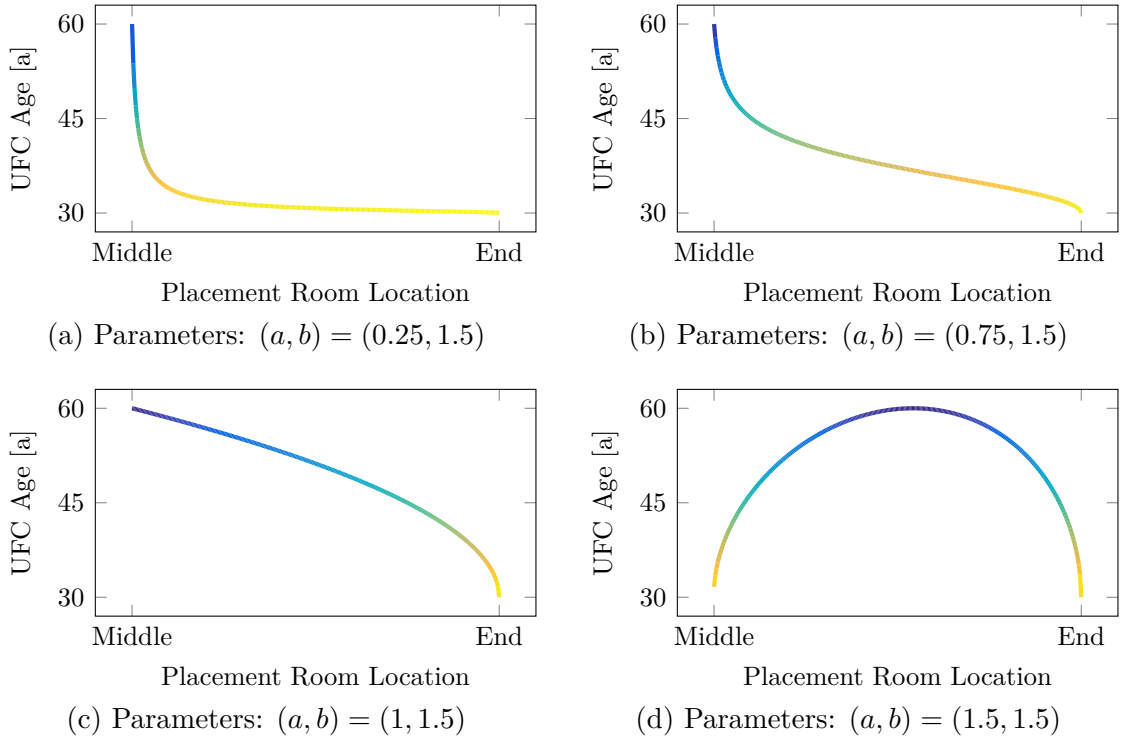

(a) Parameters: $(a, b) = (0.25, 1.5)$ (b) Parameters: $(a, b) = (0.75, 1.5)$

(c) Parameters: $(a, b) = (1, 1.5)$ (d) Parameters: $(a, b) = (1.5, 1.5)$

Colours imply that younger UFCs generate more heat compared to older UFCs.

Figure 4.2: Examples of UFC ages arranged similar to a Kumaraswamy PDF with parameters $a \in \{0.25, 0.75, 1.00, 1.50, 2.00, 4.00\}$ and $b = 1.5$

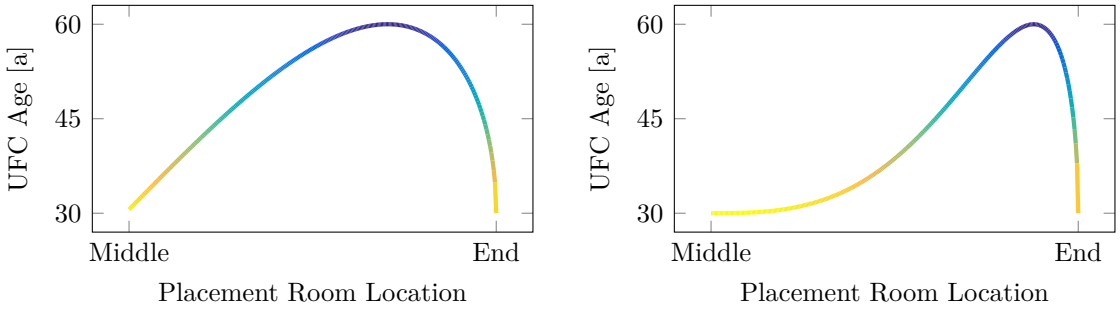

(e) Parameters: $(a, b) = (2, 1.5)$ (f) Parameters: $(a, b) = (4, 1.5)$

Colours imply that younger UFCs generate more heat compared to older UFCs.

Figure 4.2: (Continued)

4.2 Algorithm

The SBAO algorithm for solving (4.2) followed the methods and steps described in Chapter 2 and by Fig. 2.15. Initial design points were first chosen through DOE. They were evaluated using the high-fidelity COMSOL model, and then a surrogate function was fit to the data. Next, using a sampling technique, a new design point was chosen from the surrogate and evaluated using the high-fidelity model. The result from the high-fidelity model was compared with the estimate from the surrogate, and if it met a convergence criterion, the optimization process was complete. The details of each step are given below:

Initial Design Points

Initial design points were selected through an LHS with a criterion that maximized the minimum distance between points, i.e., a maximin distance design (recall (2.6)). It was chosen to start with ten initial points, and the MATLAB function *lhsdesign* was used to generate the space-filling and non-collapsing design. The maximum temperature corresponding to each initial design point was then determined through evaluating the high-fidelity model.

Surrogate Approximation

A surrogate function was fitted to available data in order to approximate the maximum temperature inside the DGR within the design space. Several surrogate functions were used for approximating the objective function in (4.2) to compare their performances, including polynomials (quadratic, reduced quadratic, cubic, and reduced cubic) and RBFs (cubic and thin-plate spline). The MATSuMoTo toolbox provided the MATLAB functions for fitting these surrogates.

Sample Point Selection

The sampling technique used to infill the design space for the problem described in (4.2) was surface-minimum sample point selection. As the identification of the feasible region was desired, design points near and on the boundary representing the 100 °C constraint should be evaluated. Surface-minimum sample point selection achieved this by selecting the local minimum of the surrogate model as the next sample point in each iteration.

Because the design variables were discrete, the next sample point chosen via surface-minimum sample point selection was based on searching within a tolerance around the minimum of the objective function. The minimum of the objective function in (4.2) is zero. At each iteration, design points that were predicted to result in maximum temperatures in the range ±0.5 °C were considered as candidates. If no candidate points were found, the tolerance was relaxed until at least one point was found. In the case that multiple candidate points were found, the point with maximin distance to all evaluated points was used to promote space-filling. Furthermore, if multiple maximin distance points existed, one was randomly selected.

Convergence Criterion

The iterative process of the optimization continued until a convergence criterion was met. The convergence criterion used was that at each iteration, the mean absolute error (MAE) on the maximum temperature inside the DGR must be less than 0.5 °C. MAE was calculated as:

$$\text{MAE} = \frac{1}{n}\sum_{i=1}^{n}|e_i| = \frac{1}{n}\sum_{i=1}^{n}|y_i - \hat{y}_i| \tag{4.6}$$

where n is the number of points evaluated during the particular iteration, e is the error, y is the true maximum temperature from the high-fidelity model, and $\hat{y}$ is the predicted maximum temperature from the surrogate model. As the sampling technique was specified to choose only one point at each iteration, (4.6) calculated the absolute error.

4.3 UFC Inventory of Identical Age

For the case of identical UFC age, all UFCs were assumed to have been discharged from a nuclear power reactor for 30 years at the time of placement into the DGR. Referring to (4.2a), the value of the UFC age design variable would be constant at $x_3 = 30$ in this case. The two remaining design variables were then UFC spacing (x_1) and room spacing (x_2). The ten initial design points chosen for x_1 and x_2 using LHS are identified in Fig. 4.3.

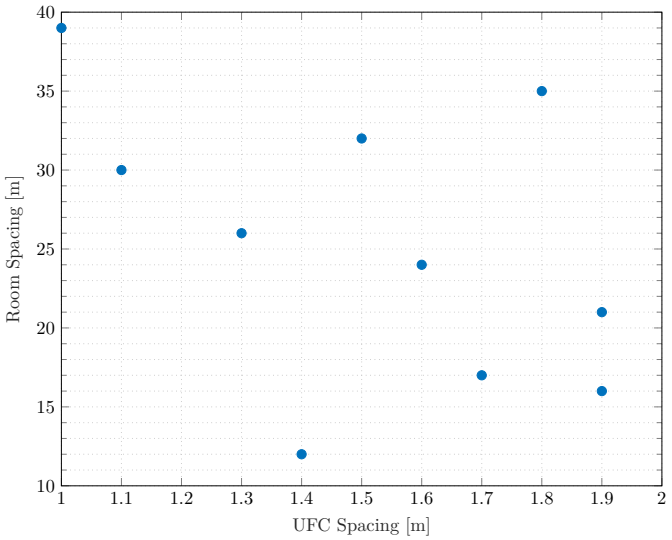

Figure 4.3: Initial design points chosen via an LHD for the identical UFC age case

The surrogate optimization process and its results using a cubic polynomial surrogate are illustrated in Fig. 4.4. Figure 4.4a shows the initial surrogate approximation based on the first ten evaluated points while the final model after the last iteration is given in Fig. 4.4b. Six iterations were required totalling 16 evaluations, and the convergence is shown in Fig. 4.4c. Feasible points closest to the maximum temperature constraint without exceeding it are the most efficient design points as they would place the most UFCs per a given amount of space. These points—UFC spacing and room spacing combinations—are identified in Fig. 4.4d. Note that the surrogate model displayed does not correspond to the objective function stated in (4.2) as it was unaesthetic to plot the surface of a two-dimensional absolute value function. For better illustration, the surfaces in Fig. 4.4 plot $T_{\max} = T_{\max}(x_1, x_2)$ with the 100 °C temperature constraint featured as bold contours.

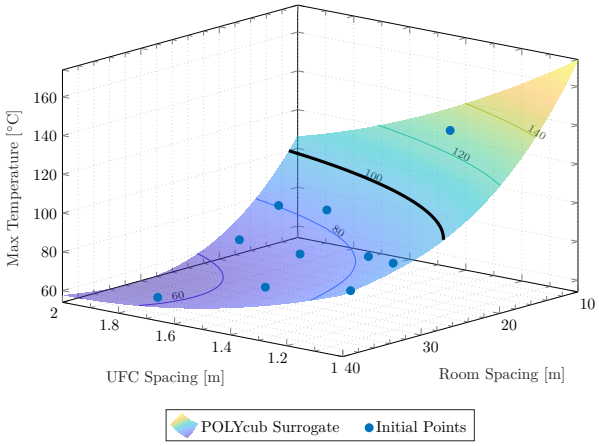

(a) Initial surrogate approximation

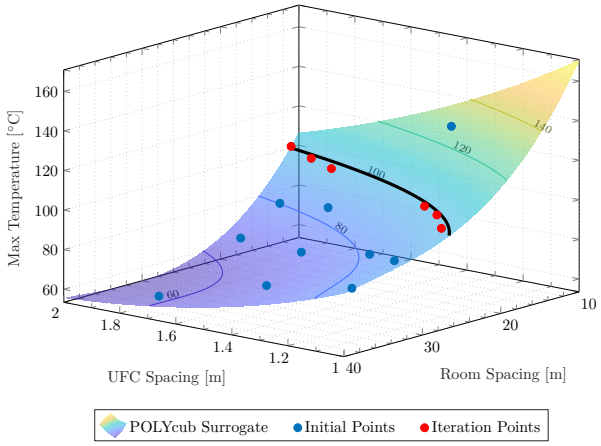

(b) Final surrogate approximation

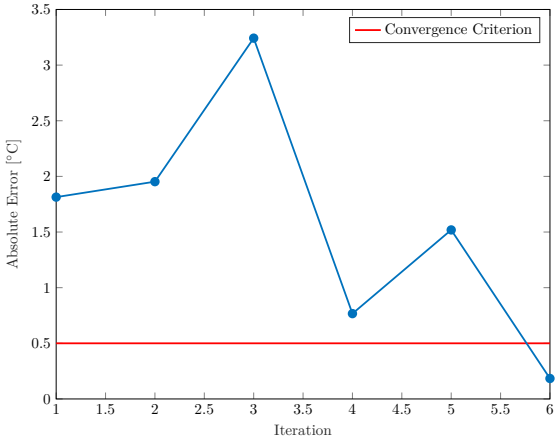

(c) Convergence plot

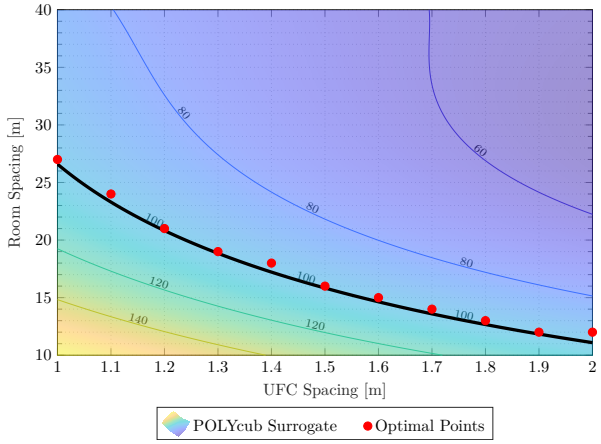

(d) Optimal UFC spacing and room spacing combinations

Figure 4.4: Surrogate optimization process using a cubic polynomial surrogate for the identical UFC age case

From first glance, the surrogate model reveals that the function for the maximum temperature inside the DGR is a decreasing function within the bounds studied in terms of both UFC spacing and room spacing. As expected, larger UFC spacings and room spacings lead to lower maximum temperatures since fewer heat-generating UFCs are packed

into a given area. The points in Fig. 4.4d are the optimal design points if the maximum temperature constraint is the only requirement considered. These points, (x_1^*, x_2^*), border the feasible region and any design point (x_1, x_2) is in the feasible region if the truth function $(x_1 \geq x_1^*) \wedge (x_2 \geq x_2^*)$ is true.

The predicted maximum temperatures from the surrogate model for the optimal points in Fig. 4.4d are organized in Table 4.1 and compared with their true maximum temperatures found by evaluating the high-fidelity model. Using a cubic polynomial function as the surrogate, predicting the maximum temperatures of the optimal points had an MAE of 1.072 °C. Considering that the feasible region was identified after 16 evaluations of the high-fidelity model, which is a small subset of the design space containing a total of 341 discrete (x_1, x_2) points, the error is arguably reasonable given the reduction in computationally expensive model evaluations. The 16 evaluations in the SBAO amounted to about 32 hours of simulation time. If all 341 discrete design points were evaluated, that would require roughly 700 hours of simulation time. This contrast shows the advantage of incorporating SBAO into the design process.

Table 4.1: Optimal design points using a cubic polynomial surrogate for the identical UFC age case

UFC Spacing [m]	Room Spacing [m]	Predicted Maximum Temperature [°C]	Actual Maximum Temperature [°C]	Error [°C]
1.0	27	99.268	100.274	−1.006
1.1	24	98.326	98.072	+0.254
1.2	21	99.462	98.813	+0.648
1.3	19	99.466	98.280	+1.186
1.4	18	96.984	95.615	+1.369
1.5	16	99.268	97.660	+1.608
1.6	15	98.302	96.728	+1.573
1.7	14	97.958	96.451	+1.506
1.8	13	98.223	97.018	+1.205
1.9	12	99.085	98.371	+0.713
2.0	12	94.886	94.164	+0.721
			Mean Absolute Error	1.072

4.3.1 Comparison of Surrogate Functions for Approximation

The choice of the surrogate function used in a surrogate model is important as it should be able to fit adequately to the true underlying model being approximated. A function that is not suited for such purposes will not yield accurate results and may also require more iterations in the optimization process before convergence. Figure 4.4 presented results that were based on using a cubic polynomial as the surrogate function for approximating the behaviour of the maximum temperature inside the DGR. In Fig. 4.5, the results and performance of SBAO using several surrogate functions (starting from the same initial points) are compared using contour plots. The comparison included reduced quadratic, cubic, and reduced cubic polynomial functions, as well as cubic and thin-plate spline RBFs.

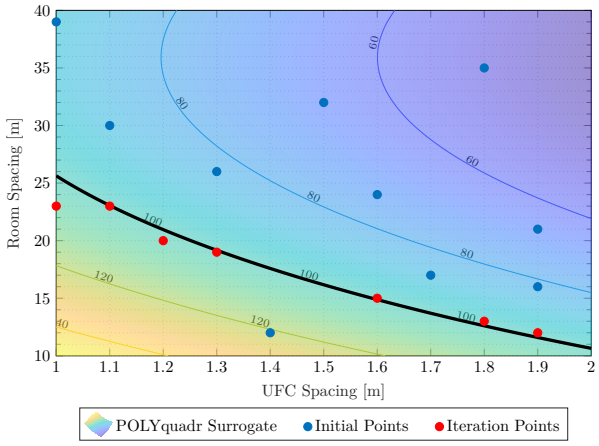

(a) Reduced quadratic polynomial
Total evaluations: 17

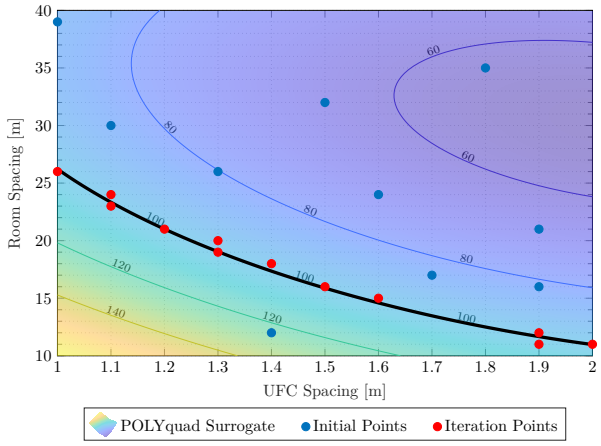

(b) Quadratic polynomial
Total evaluations: 22

Figure 4.5: Comparison of polynomial and RBF surrogates for the identical UFC age case starting from the same initial points

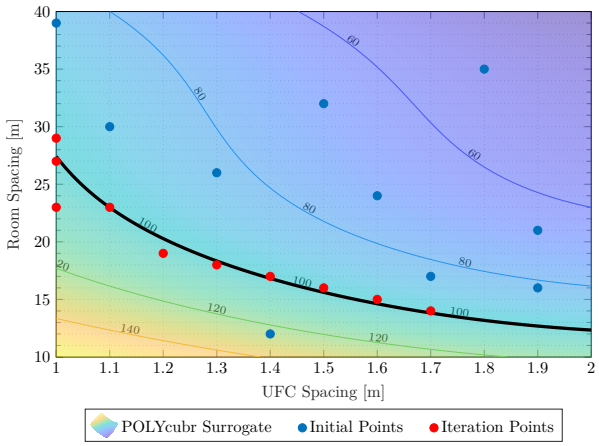

(c) Reduced cubic polynomial
Total evaluations: 20

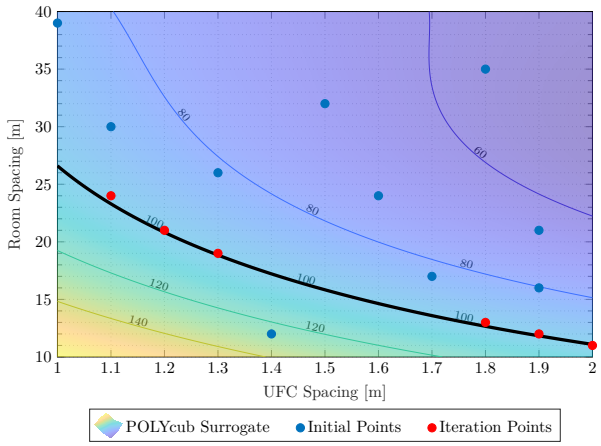

(d) Cubic polynomial
Total evaluations: 16

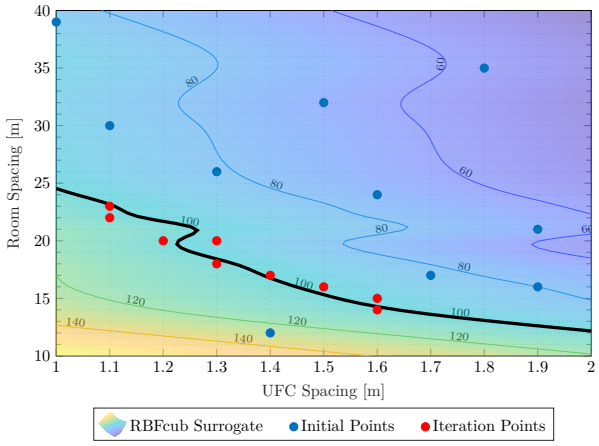

(e) Cubic RBF
Total evaluations: 19

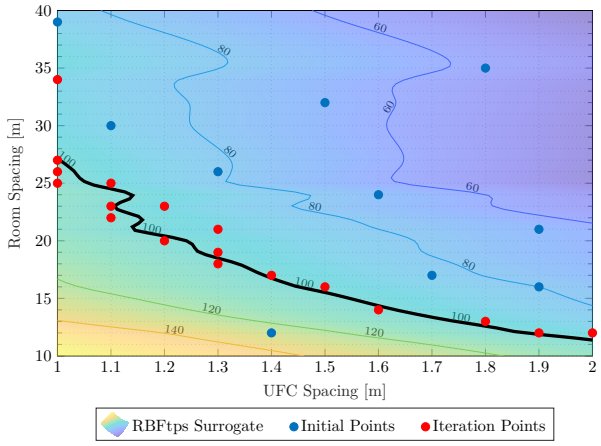

(f) Thin-plate spline RBF
Total evaluations: 28

Figure 4.5: (Continued)

From observing the plots, it is apparent that the contours resulting from polynomial surrogates (Fig. 4.5a to 4.5d) are much smoother compared to those from RBF surrogates (Fig. 4.5e and 4.5f). The reason for such behaviour is due to their different model fitting approaches. A polynomial surrogate is derived using regression where a surface that minimizes the least-squares to evaluated points is found. For an RBF surrogate, a linear combination of radially symmetric functions is used to interpolate between evaluated points.

Thus, RBF surrogate models will not be smooth if an insufficient amount of points is supplied or if the points are not space-filling. Although their contours are seen not to be very smooth, RBF surrogate models should perform better than polynomial surrogate models in terms of capturing nonlinearity as they are not limited to a fixed set of monomials as their basis functions. It can be seen that the general shapes of the contour lines in the plots corresponding to the RBF surrogates are similar to those of the polynomial surrogates. If more points were evaluated in the unexplored regions of the design space, the contour lines for the RBF surrogate models should tend toward those seen in the polynomial surrogate models—where all the maximum temperature contours were similar. Nonetheless, all the surrogate functions used modelled the overall behaviour around the maximum temperature constraint quite similarly and resulted in nearly identical feasible regions.

Comparing the total number of evaluations for each surrogate in Fig. 4.5, it is arguable that all surrogate functions performed similarly except for the thin-plate spline RBF (Fig. 4.5f), which required the most iterations until convergence. The cubic and reduced quadratic polynomial surrogate functions converged the quickest at six and seven iterations, respectively, and were followed by the cubic RBF surrogate function at nine iterations. As the maximum temperature inside the DGR is viewed as a black-box function, cubic RBF surrogates may be the better choice in later optimizations if they do not converge significantly slower than their polynomial counterparts and if they can achieve comparable overall results.

4.3.2 Initial Points Selection on Convergence

In addition to the choice of the surrogate function used in a surrogate model, the initial design points chosen through DOE (here being LHDs) are also important as they may affect the overall effectiveness of SBAO. As with all numerical methods, an inappropriate choice of initial points leads to poor convergence—or even lack thereof. Figure 4.6 shows the results and convergences of three SBAO trials starting from different initial points using cubic RBF surrogates. The first of the three results is what was previously from Fig. 4.5e. New initial points generated within the same bounds were used to obtain Fig. 4.6b while new initial points generated under tighter bounds (smaller room spacing) based on the then known maximum temperature contour were used to produce Fig. 4.6c.

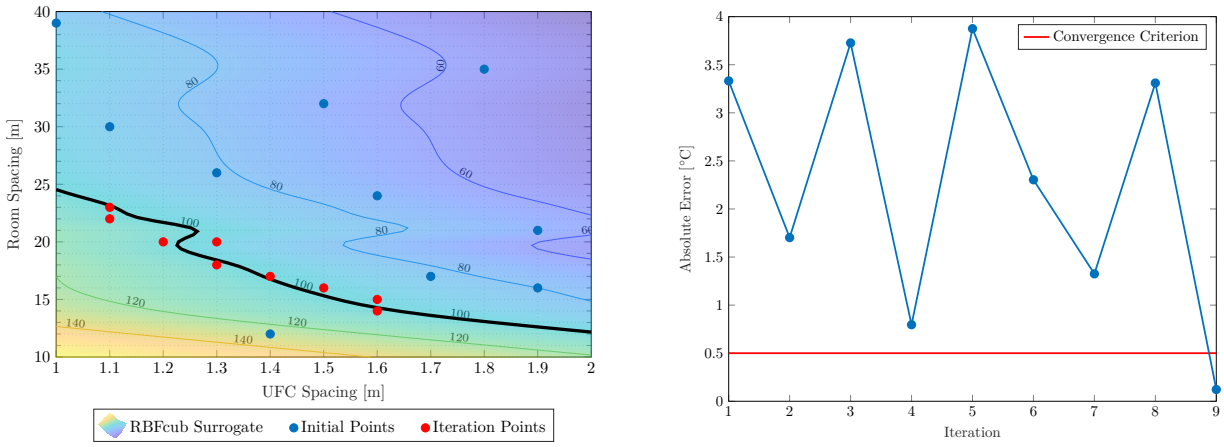

(a) Total evaluations: 19

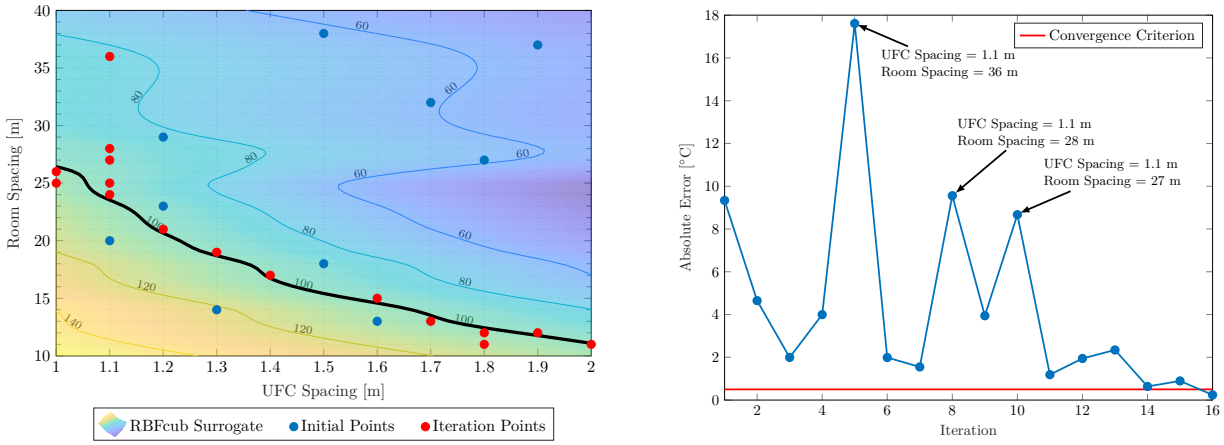

(b) Total evaluations: 26

Figure 4.6: Convergence based on different initial points using cubic RBF surrogates for the identical UFC age case

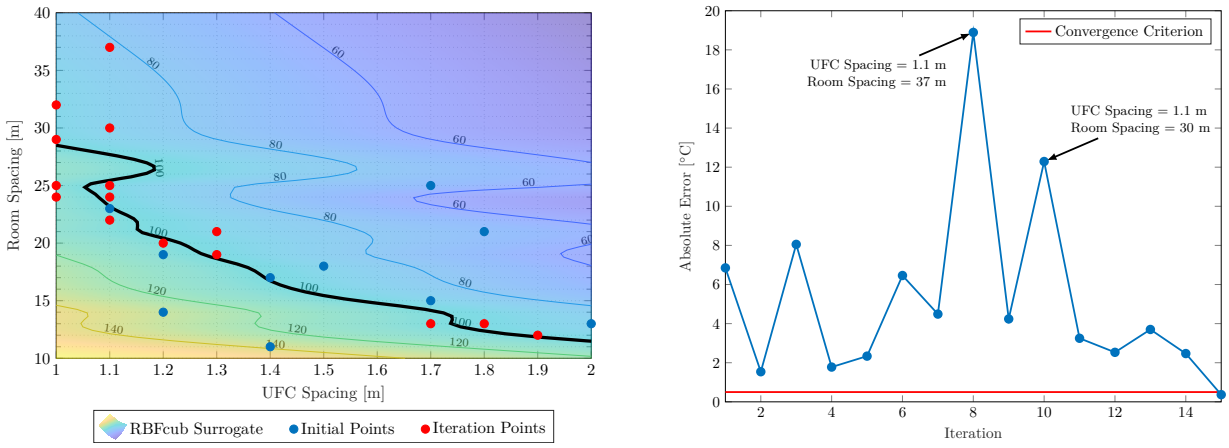

(c) Total evaluations: 25

Figure 4.6: (Continued)

The surrogate models at convergence for the three trials in Fig. 4.6 had similar overall results but the total number of iterations until convergence varied considerably between the trials. The similarity in the overall results of the three trials indicates that the choice of initial points does not affect the final surrogate model significantly, but as expected, it does affect the overall speed of convergence of the SBAO process. For instance, when new initial points were used in the second trial (Fig. 4.6b), 16 iterations were required until convergence compared to only nine originally (Fig. 4.6a). Even when new initial points were generated under tighter bounds such that more points were initially evaluated near the maximum temperature contour in the third trial (Fig. 4.6c), 15 iterations were still required. These observations show that if fast convergence is desired, careful selection of initial points through DOE is crucial.

Although fast convergence is ideal for reducing the number of iterations, and thus computation time, comparing the contour plot in Fig. 4.6a against those in Fig. 4.6b and 4.6c offers an example of when slower convergence may be worthwhile. In the first contour plot, all the iteration points are near the maximum temperature contour. In the second and third contour plots, some iteration points are scattered around the top left corner in addition to the iteration points near the maximum temperature contours. Looking at their respective convergence plots, the prominent peaks in the absolute error

corresponded to these points (see annotations). These points were chosen based on their maximin distances to all evaluated points during their respective iterations. At the cost of more evaluations, the surrogate model benefited from increased accuracy over a larger portion of the studied domain due to increased exploration.

4.4 UFC Inventory of Assorted Ages

In the case of assorted UFC ages, UFCs were assumed to be variously aged between 30 to 60 years out of a nuclear power reactor at the time of placement into the DGR. Referring to (4.2a), the value of the UFC age design variable at a particular position in the placement room would depend on the shape parameter that governs the prescribed UFC age arrangement. Here, the UFC age arrangements explored follow the shapes of sinusoidal (cosine) functions and Kumaraswamy PDFs:

$$x_3(u, \boldsymbol{\alpha}) = \begin{cases} A(u; \omega) & \text{if sinusoidal arrangement—see (4.3),} \\ A(u; a, b) & \text{if Kumaraswamy PDF-like arrangement—see (4.5).} \end{cases}$$

As it was difficult to depict results with three design variables, multiple SBAO processes were performed while one of the two remaining design variables was held constant. The two remaining design variables are UFC spacing (x_1) and room spacing (x_2), and it was chosen that room spacing would be held constant in between the optimization processes. Thus, the two design variables were UFC spacing and UFC age in each optimization. Four optimizations were carried out with room spacings of $x_2 = \{10, 15, 20, 25\}$, which were values near and including the NWMO reference design (20 m). As before, ten initial design points (now for x_1 and x_3—but more specifically, $\boldsymbol{\alpha}$) were chosen using LHS at the start of each optimization.

The SBAOs here use cubic RBF surrogates rather than polynomial functions. Although all polynomial and RBF surrogates resulted in very similar results in the previous section (see Fig. 4.5), new relationships are modelled in this section. The surrogates in the previous section concerned the relationship between UFC spacing and room spacing. However, this section focuses on the relationship between UFC spacing and UFC age arrangement (shape parameter). As it is unclear how these design variables relate to one another, RBFs are chosen to better capture nonlinear behaviours should there be any.

4.4.1 Sinusoidal UFC Age Arrangement

The results for when the UFC age was arranged in the way of a cosine function determined using cubic RBF surrogates with room spacings of $x_2 = \{10, 15, 20, 25\}$ are organized in Fig. 4.7. The figures present the final surrogate models and the optimal UFC spacing for each value of the shape parameter ($\omega = \{0.5, 1.0, 1.5, \ldots, 10.0\}$). The optimal points border the feasible region, which is located to the right of the points. Table A.1 of Appendix A.1 compares the true maximum temperatures of the optimal points to their predicted values in Fig. 4.7. Overall, 80 optimal points were identified with an MAE of 1.302 °C. Three of those points were found to be above the maximum temperature constraint of 100 °C, but only slightly (< 1 °C).

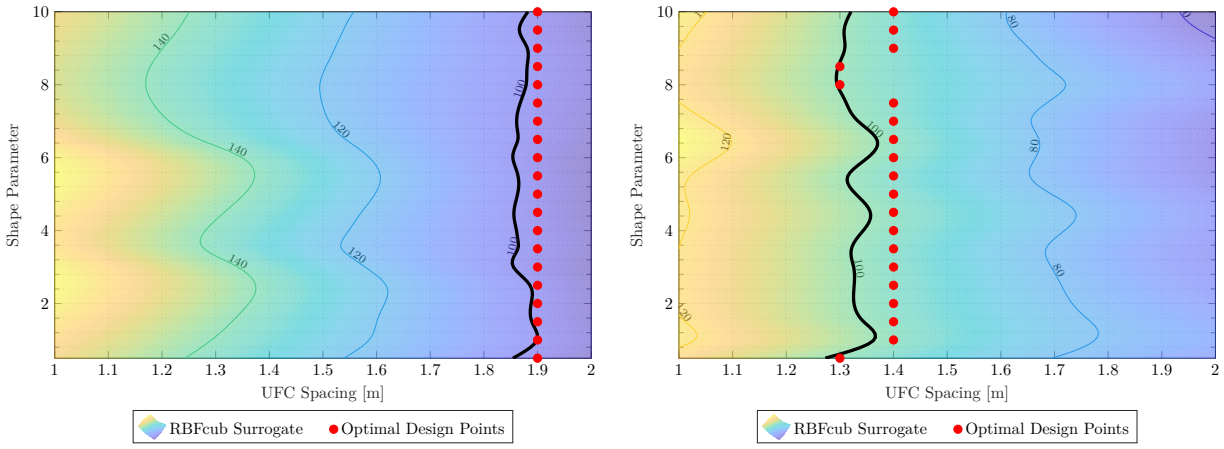

(a) Room Spacing = 10 m

(b) Room Spacing = 15 m

Figure 4.7: Surrogate optimization results using cubic RBF surrogates for a sinusoidal (cosine) UFC age arrangement

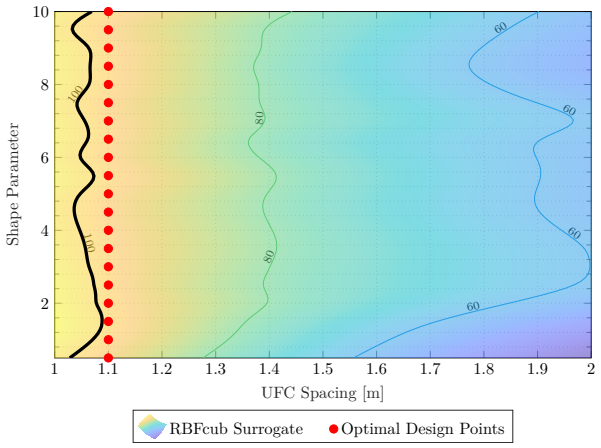

(c) Room Spacing = 20 m

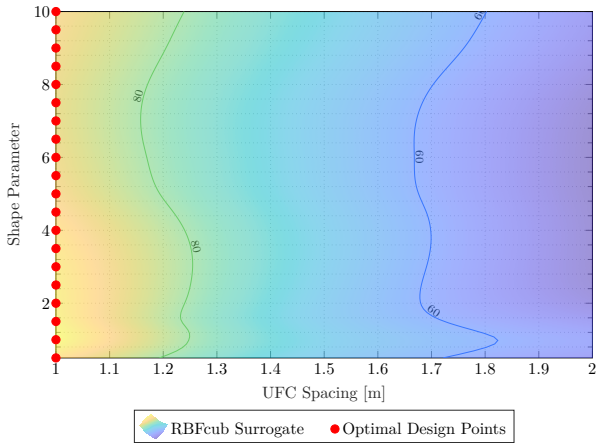

(d) Room Spacing = 25 m

Figure 4.7: (Continued)

Two main features in the contour plots are quite evident even without examining Fig. 4.7 closely. First, the maximum temperature inside the DGR was not very sensitive to the various arrangements of the UFC age when they were arranged following a family of cosine functions, within the range of the shape parameter studied. Although the maximum temperature contours are rather noisy, they can essentially be interpreted as vertical lines (note the location of the optimal points) due to the discrete domain considered. For each room spacing, the UFC spacing required at each value of the shape parameter ω in the interval $[0.5, 10]$ is essentially the same. The second obvious feature in Fig. 4.7 is that the maximum temperature contours shifted toward smaller UFC spacings as room spacing increased. This was expected, and it aligns with what was seen in Fig. 4.4 of the previous section—the identical UFC age case. Larger room spacings spread out the placement rooms, allowing the heat-generating UFCs to be placed closer together.

Observing the results from a design-focused perspective, Fig. 4.7 helps to identify the approximate minimum UFC spacing required at each room spacing for the DGR. If the 30 to 60-year-old UFCs are arranged sinusoidally (cosine) with a room spacing of 10 m, the minimum UFC spacing required would be 1.9 m. For room spacings of 15 and 20 m, the minimum UFC spacings required are about 1.4 and 1.1 m, respectively. At larger room spacings such as above 25 m, the UFC spacing can be at its lower bound of 1.0 m. This last detail indicates that spacer blocks are not necessary if the room spacing is increased past 25 m.

4.4.2 Kumaraswamy PDF-Like UFC Age Arrangement

The final surrogate models and the optimal UFC spacing for each value of the shape parameter ($a = \{0.25, 0.50, 0.75, \ldots, 4.00\}$) when the UFC age is arranged in the way of a Kumaraswamy PDF are provided in Fig. 4.8. Again, the results here were determined using cubic RBF surrogates with room spacings of $x_2 = \{10, 15, 20, 25\}$. The feasible region is located to the right of the plotted optimal points. The true maximum temperatures of the optimal points compared to their predicted values in Fig. 4.8 are listed in Table A.3 of Appendix A.2. Overall, 56 optimal points were identified with an MAE of 1.308 °C. Four of these points exceeded the maximum temperature constraint of 100 °C, which could be mitigated should a tighter convergence criterion be applied.

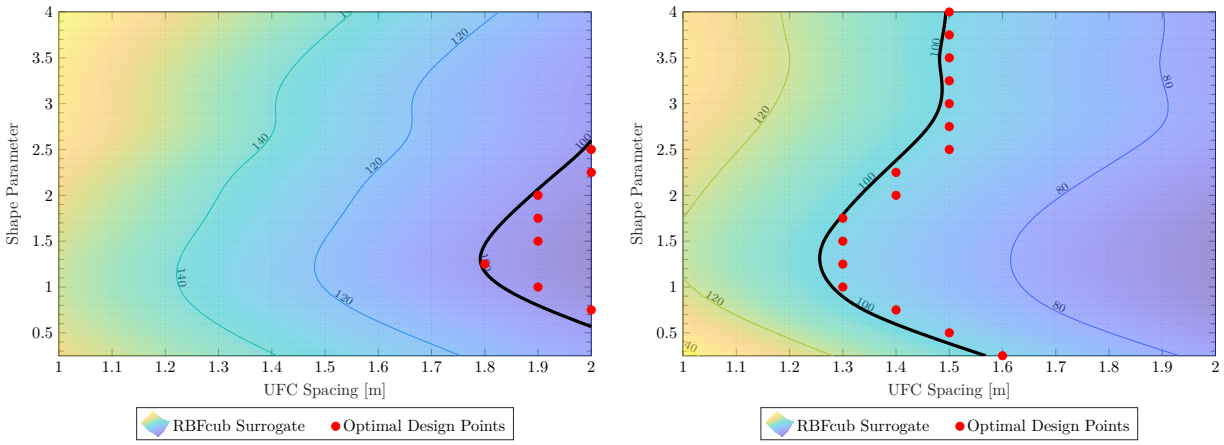

(a) Room Spacing = 10 m (b) Room Spacing = 15 m

Kumaraswamy shape parameters a varying and $b = 1.5$.

Figure 4.8: Surrogate optimization results using cubic RBF surrogates for a Kumaraswamy PDF-like UFC age arrangement

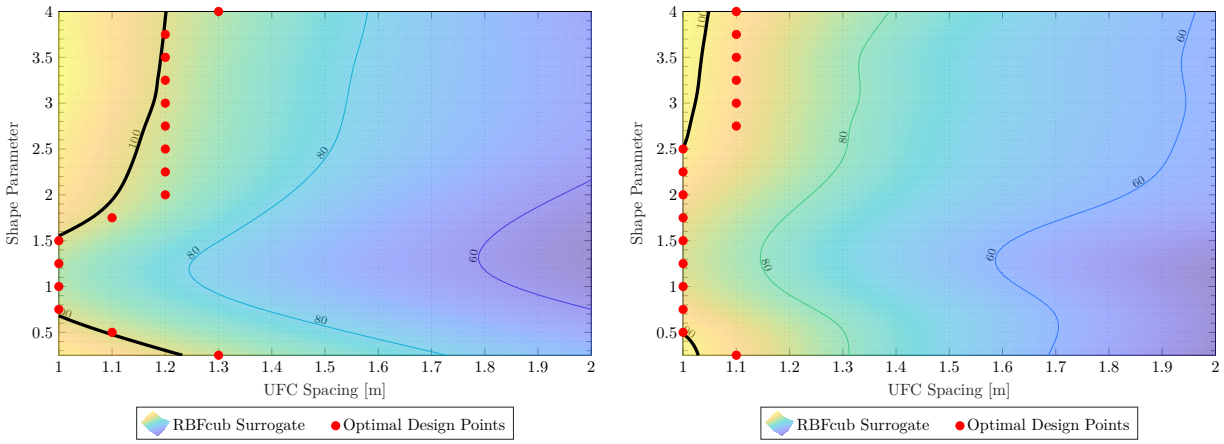

(c) Room Spacing = 20 m (d) Room Spacing = 25 m

Kumaraswamy shape parameters a varying and $b = 1.5$.

Figure 4.8: (Continued)

Similar to previous observations, the maximum temperature contours in Fig. 4.8 are seen to shift toward smaller UFC spacings as the room spacing increased. However, unlike what was seen in the sinusoidal UFC age arrangement case, the maximum temperature inside the DGR was indeed affected by the various arrangements of the UFC age when they were arranged following a family of Kumaraswamy PDFs, within the range of the shape parameter studied. For a given room spacing, the maximum DGR temperatures were the hottest near the bounds of the shape parameter ($a \to 0.25$ or $a \to 4.00$). In reference to Fig. 4.2, this makes sense as these values of the shape parameters bring more young UFCs closer together compared to shape parameter values in between the bounds. The shape parameter values of $a \to 0.25$ and $a \to 4.00$ assume that the UFC inventory mainly comprises young and high heat-generating containers whereas the values of $0.25 < a < 4.00$ assume that the UFC inventory has more of a balance between the UFC ages.

Based on Fig. 4.8, at a room spacing of 10 m and UFC spacing up to 2.0 m, only shape parameter values of $0.75 \leq a \leq 2.50$ can result in maximum temperatures below 100 °C. Spacer blocks are not necessary (i.e., UFC spacing of 1.0 m) at a room spacing of 20 m if the shape parameter a is in the interval $[0.75, 1.50]$, and are also not necessary at a room spacing of 25 m if the shape parameter is in the interval $[0.50, 2.50]$. Generally speaking, to ensure that a UFC inventory of assorted UFC ages (within the shape parameter range explored) is placed such that the maximum temperature inside the DGR does not exceed 100 °C, the approximate maximum UFC spacings required at room spacings of 15, 20,

and 25 m are 1.6, 1.3, and 1.1 m, respectively. These values of UFC spacing represent an upper limit because if the placement of the variously aged UFCs does not respect the arrangement specified by the shape parameter, the expected maximum temperature would only be lower than predicted by the surrogates of Fig. 4.8. This is because the maximum UFC spacings required mentioned above correspond to the shape parameter values of either $a = 0.25$ or $a = 4.00$, which put the most number of young, high heat-generating UFCs together. Deviating from the arrangement specified by the shape parameter values of $a = 0.25$ or $a = 4.00$ would only spread the young, hot containers among other older and cooler containers, lowering the peak temperature achieved.

4.4.3 Review of Surrogate Function Choice

Thus far, the SBAOs in this section used cubic RBF surrogates to model the relationship between UFC spacing and UFC age arrangement (shape parameter) at various values of room spacing. The choice of using RBFs over polynomial functions as the surrogates were mentioned previously, with the main reason being that RBFs would model nonlinearity better than polynomial functions should there be any. For comparison, the optimizations leading to Fig. 4.7 and 4.8 were repeated using cubic polynomial surrogate functions, and some results are shown in Fig. 4.9 and 4.10. The remaining plots can be found in Appendix A (Fig. A.1 and A.2). Tables comparing the true maximum temperatures of the optimal points to their predicted values are also located in the appendix (Table A.2 and A.4).

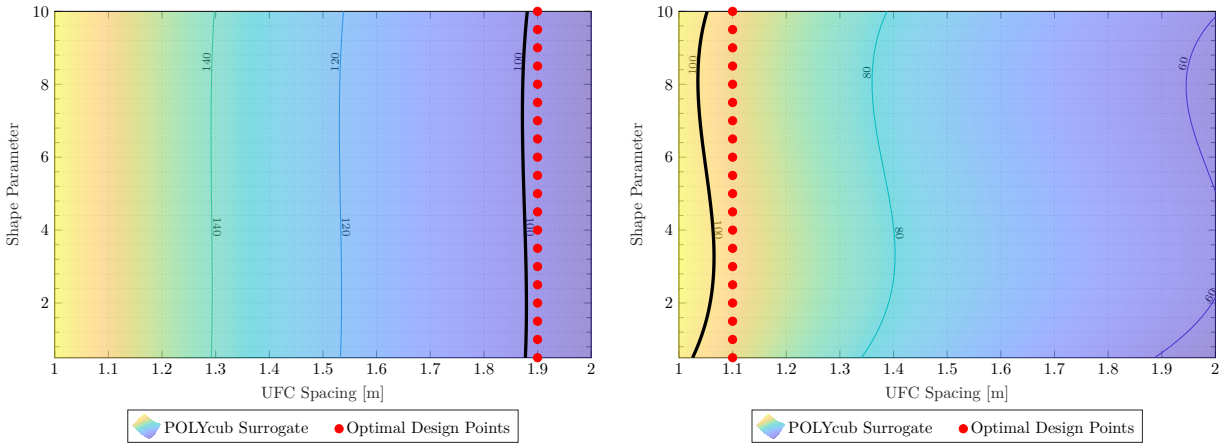

(a) Room Spacing = 10 m (b) Room Spacing = 20 m

Figure 4.9: Surrogate optimization results using cubic polynomial surrogates for a sinusoidal (cosine) UFC age arrangement

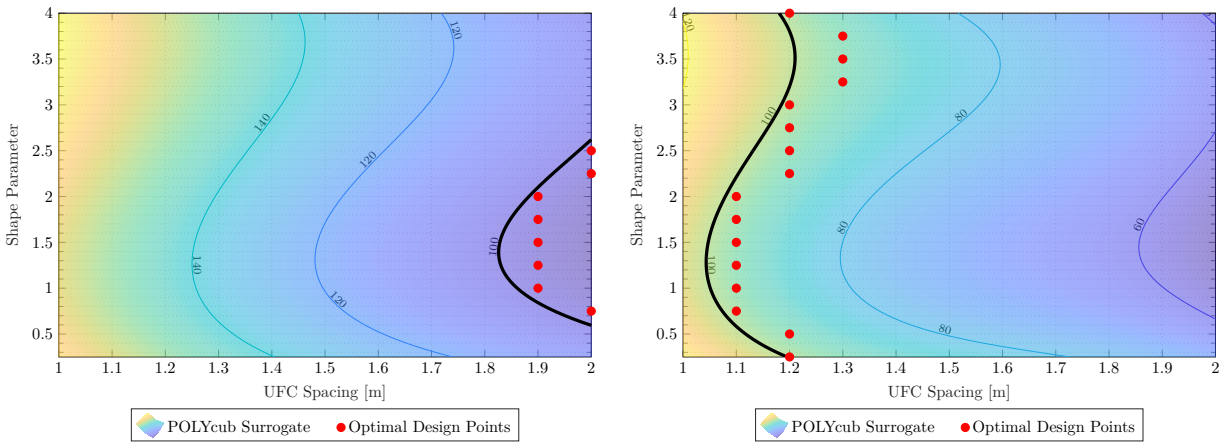

(a) Room Spacing = 10 m (b) Room Spacing = 20 m

Kumaraswamy shape parameters a varying and $b = 1.5$.

Figure 4.10: Surrogate optimization results using cubic polynomial surrogates for a Kumaraswamy PDF-like UFC age arrangement

When comparing Fig. 4.9 to Fig. 4.7, the results for a sinusoidal UFC age arrangement are identical. The cubic polynomial surrogate functions seem to fit the maximum temperatures inside the DGR easily and do so with very smooth contour lines. Because the contour lines are almost linear, using polynomial functions would have been sufficient in this case for modelling the relationship between UFC spacing and UFC age arrangement. They may perhaps even be better than RBFs here as the contour lines are not as noisy. This observation is supported by the MAE being smaller when using polynomial functions (0.543 °C) than when using RBFs (1.302 °C).

However, when comparing Fig. 4.10 to Fig. 4.8, there are major differences in the results for a Kumaraswamy PDF-like UFC age arrangement. The cubic polynomial surrogates seem to fit the maximum temperatures inadequately. As explained earlier, it was expected that for small and large values of the shape parameter ($a \to 0.25$ or $a \to 4.00$), the DGR would be at its hottest, and thus would require the largest UFC spacing. This is not the case in Fig. 4.10b where it is predicted that shape parameters values $a = \{3.25, 3.50, 3.75\}$ would require larger UFC spacings than when $a = 4.00$. As well, due to the curve shape of the cubic polynomial surrogates and how they interpolate between data points, they did not estimate when the absence of spacer blocks (UFC spacing of 1.0 m) is allowed very well. These poor predictions are reflected by a larger MAE of 2.102 °C when polynomial functions were used compared to 1.308 °C for RBFs. These observations support the use of RBFs as the surrogate functions in this section rather than polynomial functions.

4.5 Summary

In this chapter, the maximum temperature inside a crystalline DGR for when UFCs are identical and assorted in age were investigated using SBAO. The use of SBAO proved advantageous in reducing the number of high-fidelity model evaluations required to reach convergent results, providing the benefit of saving computation time and resources. Only a small subset of the entire design space had to be evaluated using the high-fidelity model of the DGR when SBAO was employed. While it was shown that although the choice of initial points supplied to the SBAO did not affect the overall converged results, the choice of the surrogate function did play a role in obtaining accurate conclusions. Cubic polynomial surrogate functions were used for the identical UFC age case while cubic RBF surrogates were used for the assorted UFC ages case.

For an inventory of identical UFC age where all the UFCs were assumed to be discharged from a nuclear power reactor for 30 years, the feasible region in two design variables (UFC spacing and room spacing) was identified. For an inventory of assorted UFC ages where UFCs were assumed to be 30–60 years out of a nuclear power reactor, feasible regions in the two design variables of UFC spacing and shape parameter at fixed values of a third design variable, room spacing, were identified for two UFC age arrangements—sinusoidal (cosine) and Kumaraswamy PDF-like. Should a DGR with a comparable UFC inventory be constructed such that the design point is within the identified feasible regions, the DGR should safely contain the UFCs without system failure. Since the inventory of used nuclear fuel can change leading up to and during DGR operation and because the design of the DGR has not been finalized to date, the visualization of the feasible regions in this chapter offers insight into how future additions to Canada's existing UFC inventory can be stored while still satisfying the studied maximum temperature constraint.

Chapter 5

Yield Optimization

The results from SBAO in Chapter 4 offered insight into how various arrangements of UFCs could affect the maximum temperature evolved inside the studied DGR. The conclusions regarding the required UFC spacings and room spacings were deterministic as they assumed that at each value of the shape parameter considered (whether it be ω for the sinusoidal arrangement or a for the Kumaraswamy PDF-like arrangement), the spacer blocks separating the UFCs and the separations between the placement rooms could be manufactured or constructed exactly to measure. Thus, those deterministic solutions are only reliable if that assumption is true. In practice, however, it would be difficult to precisely obtain a specific DGR design due to manufacturing and construction limitations. This means that the maximum temperature inside the repository could deviate from a deterministic value and possibly lead to system failure.

Since variability (uncertainty) in the design could lead to unexpected occurrences of system failure, it was an important aspect to consider. Yield optimization is a method to mitigate failure by taking into account the expected tolerances of the design variables and the shapes of their random distributions. Again, yield is the probability of a design meeting specifications, and in this thesis, the maximum temperature inside the DGR must not exceed 100 °C. Depending on the problem formulation, yield optimization can reduce a design's failure probability by either: (i) determining what the allowed tolerances on design variables are at a fixed nominal design point or (ii) determining a more robust nominal design point given the tolerances on design variables. The latter would be the method used here.

This chapter first examines the yield of selected deterministically identified optimal points found in the previous chapter through SBAO for the assorted UFC ages case under assumed tolerances and distributions for two of the three design variables—UFC spacing and room spacing. Then, yield optimization is performed to determine new nominal design points that would minimize the probability of system failure at specific shape parameter values. The yield optimization would determine both nominal points that lead to no failure (100% yield) and points that allow some small probabilities of failure (95, 97, and 99% yields).

5.1 Tolerance and Distribution Assumptions

The design variables treated as random variables were the UFC spacing (x_1) and room spacing (x_2). Additional variables could be considered if known, e.g., the density of the bentonite materials as they swell in the presence of groundwater after DGR closure. UFC spacing was expected to vary due to variabilities originating from the spacer blocks that separate the buffer boxes containing the UFCs. The spacer blocks might be manufactured or placed into the DGR imperfectly, leading to deficient or excess UFC spacings. Room spacing was expected to vary due to unpredictable variations in the host rock of the DGR and construction complications underground. Excavation methods such as blasting might result in overbreaks in the host rock, and construction oversight might lead to placement rooms not being spaced according to design. In consideration of all these uncertainties, the tolerances for the design variables used in this chapter are 0.2 m for UFC spacing and 3 m for room spacing. In other words, with reference to a nominal design point, the ranges considered would be $x_1 \pm 0.1$ and $x_2 \pm 1.5$. These are believed to be reasonably anticipated variations; however, the methodology could consider any other ranges if known.

In terms of the distributions of the UFC spacing and room spacing values, the Kumaraswamy distribution was used for both random variables. As introduced in Chapter 2, depending on the values of its two parameters, a and b, the Kumaraswamy distribution can take on different shapes and mimic common distributions. With that available, several combinations of PDFs were considered. The two design variables were assumed to be independent since the manufacturing of the spacer blocks and the excavation of the host rock should be unrelated events. The combinations of distributions considered for UFC spacing and room spacing are presented in Table 5.1, and examples of the joint PDFs are illustrated in Fig. 5.1.

Table 5.1: Various distributions for UFC spacing and room spacing

Case	Parameters		Distributions	
	$\boldsymbol{a}$	$\boldsymbol{b}$	x_1	x_2
1	[1,1]	[1,1]	Uniform	Uniform
2	[2.5,2.5]	[4,4]	Gaussian-like	Gaussian-like
3	[8,8]	[8,8]	Kurtotic, tending large	Kurtotic, tending large
4	[1,2]	[2,1]	Triangular, tending small	Triangular, tending large
5	[5,1]	[1,5]	Tail, tending large	Tail, tending small
6	[2.5,2]	[4,1]	Gaussian-like	Triangular, tending large

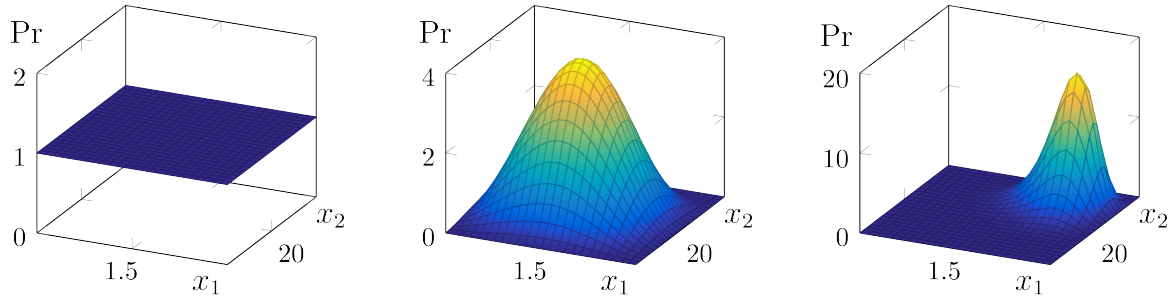

(a) Case 1 (b) Case 2 (c) Case 3

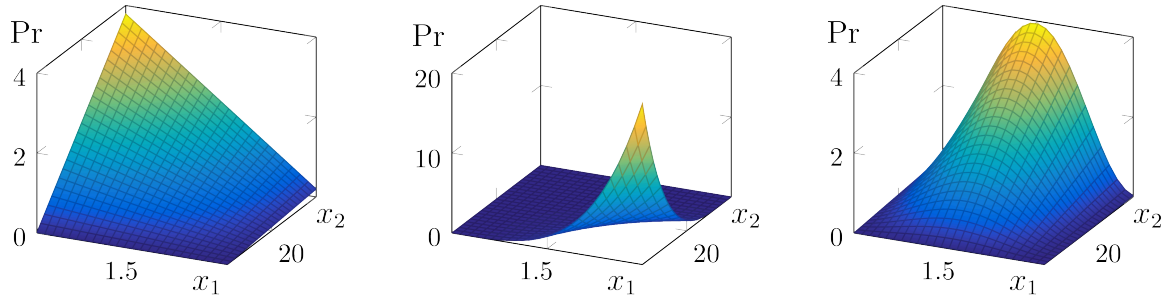

(d) Case 4 (e) Case 5 (f) Case 6

Distribution parameters for each case are from Table 5.1. Assuming independence.
Using nominal point $(x_1, x_2) = (1.5, 20)$ with tolerances of $x_1 \pm 0.1$ and $x_2 \pm 1.5$.

Figure 5.1: Joint PDFs for various distributions of UFC spacing and room spacing

If the true distribution of each design variable were known, much value could be obtained from yield optimization. However, without that information, the distributions listed in Table 5.1 could be used to explore different manufacturing and construction cases for the time being. Designing for Case 1 leads to a worst-case design as both UFC spacing and

room spacing would be assigned uniform distributions. This would be useful if absolutely no information about the distributions of design variables were available. Case 2 represents when the design variables are approximately normally distributed. The remaining cases in the table assume that the manufacturing and construction of the DGR and its components are such that the distributions of the design variables are asymmetric (Case 3–6), i.e., there are tendencies for under- or overshooting nominal values. Note that the realized values of the random variables would be applied to the entire DGR, with all components (UFC spacing and room spacing) being identical.

5.2 Yield of Optimal Points from SBAO

The deterministically identified optimal points from the previous chapter chosen for further investigation to determine their yields under assumed tolerances and distributions were from Fig. 4.8b. The figure corresponds to UFC inventories of assorted ages placed inside the DGR following Kumaraswamy PDF-like arrangements with shape parameters a varying and $b = 1.5$ at a room spacing of 15 m. For clarity, the design variables being random variables having Kumaraswamy distributions (Table 5.1) is different from the arrangement of the variously aged UFCs following Kumaraswamy PDFs. Three design points (with variables of UFC spacing, room spacing, and shape parameter) were of interest:

Point A $x_1 = 1.6$, $x_2 = 15$, and $a = 0.25$,
Point B $x_1 = 1.3$, $x_2 = 15$, and $a = 1.25$, and
Point C $x_1 = 1.5$, $x_2 = 15$, and $a = 4.00$.

5.2.1 Feasible Regions via SBAO

To investigate how variabilities in the UFC spacing (x_1) and room spacing (x_2) affected the yield of the DGR, the feasible regions defined by these two design variables were required. Point A is in the design space corresponding to a shape parameter of $a = 1.25$, while Point B and C are in the design spaces corresponding to $a = 0.25$ and $a = 4.00$, respectively. It was found previously in Fig. 4.5 that the maximum temperature contour in the two-dimensional design space of UFC spacing and room spacing was similarly approximated when using polynomial and RBF surrogates. Thus, for consistency and algebraic simplicity, cubic polynomial surrogates were used again to identify the feasible regions needed in this chapter.

Using available data and the same design variable bounds from Chapter 4, SBAO was performed again to determine the feasible regions required. The resulting feasible regions for Kumaraswamy shape parameter values of $a = \{0.25, 1.25, 4.00\}$ are distinguished as shaded regions in Fig. 5.2. For increased accuracy when determining the maximum temperature contours, the convergence criterion used in the SBAO processes here were tightened to 0.25 °C instead of 0.5 °C as used before.

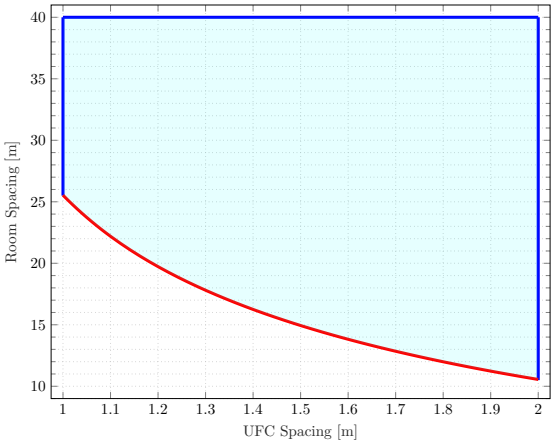

(a) $R_{A,\,a=0.25}$

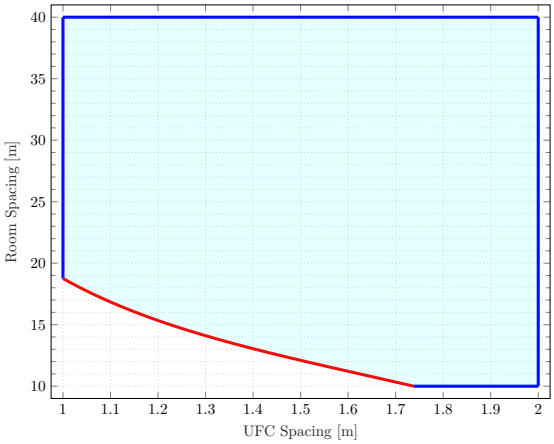

(b) $R_{A,\,a=1.25}$

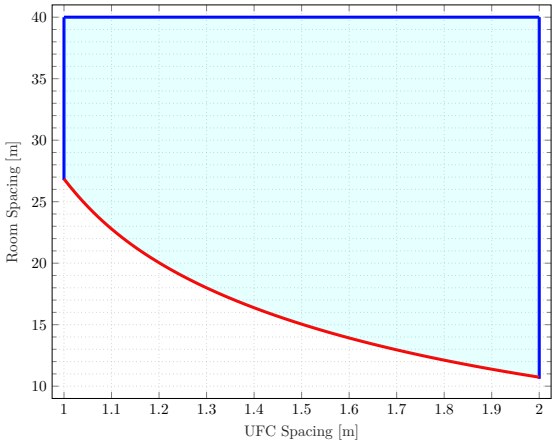

(c) $R_{A,\,a=4.00}$

Boundary constraints in blue. Maximum temperature constraint in red.
Kumaraswamy shape parameter $b = 1.5$.

Figure 5.2: Feasible regions (UFC spacing and room spacing) for various Kumaraswamy PDF-like UFC age arrangements

5.2.2 Monte Carlo Simulations

The yield of the three selected deterministically identified optimal points under assumed tolerances and distributions were determined using Monte Carlo simulations. For each nominal point (Point A, B, and C), randomly selected points from the appropriate Kumaraswamy distribution were observed to either fall within or beyond their feasible region. From the yield equation in (2.16), yield can be calculated as the number of realized points that are within their feasible region over the total number of realizations. The results from Monte Carlo simulations for the three points of interest with the design variables following the six distributions cases in Table 5.1 are shown in Table 5.2. The reason for the yields at Point C being significantly lower than those at Point A and B was because Point C lied very close to the boundary of its feasible region. The points' distances from the boundaries differed due to the optimal design points being chosen from discrete sets of values ($x_1 = \{1.0, 1.1, 1.2, \ldots, 2.0\}$ and $x_2 = \{10, 11, 12, \ldots, 40\}$). For visualization, Case 1 and 4 corresponding to uniform and triangular distributions, respectively, are shown in Fig. 5.3. Plots for the remaining cases are given in Appendix B.1.

Table 5.2: Yield of various optimal points from SBAO

Case	Parameters		Monte Carlo Yield		
	a	b	Point A	Point B	Point C
1	[1,1]	[1,1]	84.4%	75.3%	48.6%
2	[2.5,2.5]	[4,4]	93.0%	84.9%	42.0%
3	[8,8]	[8,8]	100%	100%	99.4%
4	[1,2]	[2,1]	91.5%	85.0%	53.6%
5	[5,1]	[1,5]	96.8%	88.9%	27.3%
6	[2.5,2]	[4,1]	96.8%	92.6%	70.1%

Using tolerances of $x_1 \pm 0.1$ and $x_2 \pm 1.5$.
Total of 1000 Monte Carlo simulations performed.

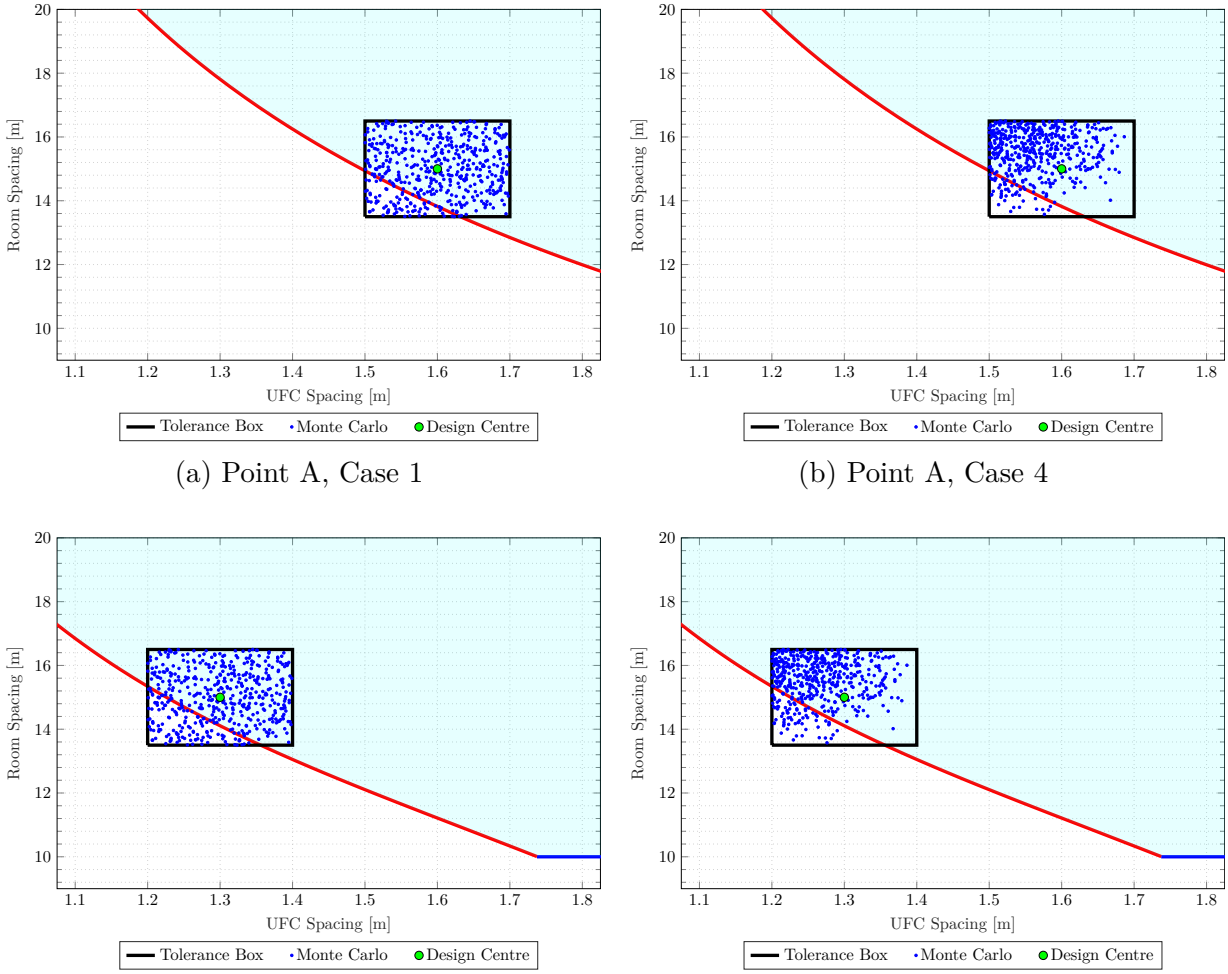

(a) Point A, Case 1

(b) Point A, Case 4

(c) Point B, Case 1

(d) Point B, Case 4

Distribution parameters for each case are from Table 5.1. 500 Monte Carlo simulations shown.

Figure 5.3: Monte Carlo simulations for various optimal points from SBAO and design variable distributions

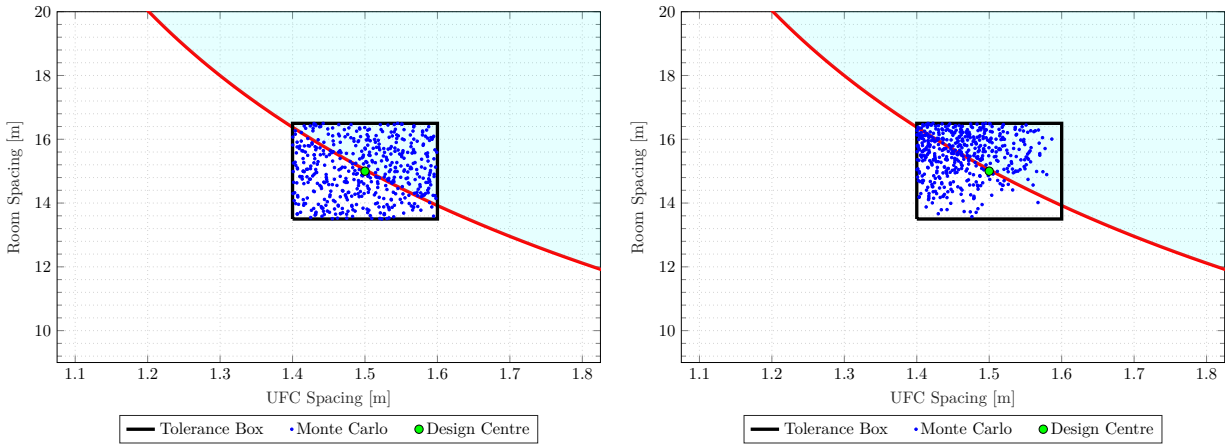

(e) Point C, Case 1

(f) Point C, Case 4

Distribution parameters for each case are from Table 5.1. 500 Monte Carlo simulations shown.

Figure 5.3: (Continued)

While the deterministically identified optimal points found in the previous chapter might have seemed to be efficient because the smallest feasible combinations of UFC spacing and room spacing were chosen, which would reduce DGR cost and size, Table 5.2 shows otherwise. The table reveals that depending on the actual design variables' distributions, the points might not be the best choices when uncertainty is taken into account. Most of the yields listed in the table are not at or even close to an ideal 100%. By having the nominal points very close to the boundaries of their feasible region, there was a higher probability that their realized points would lie outside their feasible region. It is here that we see the need to perform yield optimization to determine more robust design points.

Examining Fig. 5.3, it can be seen that if both the distributions of UFC spacing and room spacing skew toward larger values, the yield of the DGR increases. This is due to the maximum temperature constraint sloping downwards and the feasible region lying above it. This indicates that if tight tolerances in the manufacturing and construction of the DGR and its components cannot be achieved and if the maximum temperature constraint is the only consideration, then as can be expected, choosing processes that would more likely lead to larger UFC spacings and room spacings should be preferred—but these can be costly solutions.

5.3 Yield Optimization for Nominal Design Points

The analysis of the deterministically identified optimal points found in Chapter 4 in the section above made clear the need for yield optimization. Table 5.2 and Fig. 5.3 demonstrated that the optimal points might not result in a DGR with perfect yield should there be variabilities in the design variables. Depending on the sizes of the design variables' tolerances and the distributions of their values, the probability of the designed DGR meeting performance specifications would change. For ensuring the highest chance of avoiding system failure, yield optimization could be applied to determine new nominal design points in which the aforementioned uncertainties would be incorporated.

As mentioned before, the yield optimization method used in this thesis determines more robust nominal design points given tolerances on design variables. In this section, yield optimization is performed for the three feasible regions corresponding to Point A, B, and C (i.e., the two-dimensional design spaces for UFC spacing and room spacing at specific shape parameter values). The feasible regions required are the same as those determined via SBAO earlier (illustrated in Fig. 5.2).

5.3.1 Worst-Case Design

Due to the bounds selected for SBAO in the previous chapter, the feasible regions were very large in comparison to any reasonably sized tolerance box (see Fig. 5.2 and 5.3), and so, 100% yield was always achievable. Thus, any distribution case assumed for the design variables (e.g., those in Table 5.1) would always lead to the same optimal nominal design point—essentially the worst-case design. In this subsection, the three nominal design points that yield 100% for the feasible regions of interest, regardless of the design variables' distributions, are determined.

Problem Formulation

If one were to perform yield optimization (recall (2.26)) using very large feasible regions, the nominal design points found would be centred in their respective feasible regions as they would be the furthest from all their constraints. However, these results would not be desirable for the DGR design problem at hand because more efficient design points should exist. Design points that use smaller UFC spacings and room spacings (toward the bottom left regions of Fig. 5.2) are better design points as they would lead to UFCs being placed more densely together, reducing repository size and cost.

To have yield optimization lead to nominal design points which take into consideration the preference for smaller values of UFC spacing and room spacing, the objective function in the yield maximization problem described in (2.26) was modified to include two small penalty terms that would be proportional to the values of the design variables. Since a preference between repository size and cost had not been specified by NWMO yet, arbitrary weights for the penalty terms were assigned. This led to the following problem formulation:

$$\begin{aligned} \max_{\boldsymbol{x}^r, \boldsymbol{x}^l, \boldsymbol{x}^u} \quad & Y(\boldsymbol{x}^r, \boldsymbol{x}^l, \boldsymbol{x}^u) - \frac{1}{100}\left(\frac{\theta(X_{0,1} - x_1^L)}{x_1^U - x_1^L} + \frac{(1-\theta)(X_{0,2} - x_2^L)}{x_2^U - x_2^L}\right) \\ \text{s.t.} \quad & \boldsymbol{A}^+\boldsymbol{x}^u - \boldsymbol{A}^-\boldsymbol{x}^l \leq \boldsymbol{c} \\ & \boldsymbol{x}^u \leq \boldsymbol{x}^r + \boldsymbol{t} \\ & \boldsymbol{x}^r \leq \boldsymbol{x}^l \leq \boldsymbol{x}^u \end{aligned} \tag{5.1}$$

where θ is an arbitrary weighting parameter, and $\boldsymbol{X}_0 = \boldsymbol{x}^r + 0.5\boldsymbol{t}$ is the design centre with indices 1 and 2 corresponding to UFC spacing and room spacing, respectively. The constant 1/100 scales the penalty terms down so that maximizing yield is of higher priority. Note that the lowercase superscripts l and u denote the bounds of the optimal maximum yield box while the uppercase superscripts L and U denote the bounds of the design variables.

Feasible Regions

The feasible regions corresponding to Point A, B, and C required for yield optimization were those determined via SBAO and illustrated in Fig. 5.2. Reiterating, the feasible regions were for shape parameter values of $a = \{0.25, 1.25, 4.00\}$, and they were determined using cubic polynomial surrogate functions with a 0.25 °C convergence criterion. To more accurately specify the feasible regions, they were described in the form of (2.18) as follows:

$$\text{a)}\ R_{A,\,a=0.25} = \left\{ \boldsymbol{x} \in \mathbb{R}^2 \;\middle|\; \begin{array}{l} x_1 - 1 \geq 0, \\ 2 - x_1 \geq 0, \\ x_2 - 10 \geq 0, \\ 40 - x_2 \geq 0, \\ -329.82 + 173.25x_1 + 18.13x_2 - 40.25x_1^2 \\ \quad -1.32x_1x_2 - 0.50x_2^2 + 3.76x_1^3 + 0.01x_2^3 \geq 0 \end{array} \right\},$$

$$\text{b)}\ R_{A,\,a=1.25} = \left\{ \boldsymbol{x} \in \mathbb{R}^2 \;\middle|\; \begin{array}{l} x_1 - 1 \geq 0, \\ 2 - x_1 \geq 0, \\ x_2 - 10 \geq 0, \\ 40 - x_2 \geq 0, \\ -379.69 + 370.32x_1 + 16.21x_2 - 189.31x_1^2 \\ \quad -1.58x_1x_2 - 0.41x_2^2 + 39.96x_1^3 + 0.004x_2^3 \geq 0 \end{array} \right\}, \text{ and}$$

$$\text{c)}\ R_{A,\,a=4.00} = \left\{ \boldsymbol{x} \in \mathbb{R}^2 \;\middle|\; \begin{array}{l} x_1 - 1 \geq 0, \\ 2 - x_1 \geq 0, \\ x_2 - 10 \geq 0, \\ 40 - x_2 \geq 0, \\ -344.34 + 175.39x_1 + 19.22x_2 - 38.18x_1^2 \\ \quad -1.30x_1x_2 - 0.54x_2^2 + 2.84x_1^3 + 0.01x_2^3 \geq 0 \end{array} \right\}.$$

Note that the boundary constraint $x_2 - 10 \geq 0$ is redundant in the first and third sets above (see Fig. 5.2).

Having the constraints $\boldsymbol{h}(\boldsymbol{x})$ defining the bounded feasible regions identified algebraically, the yield optimization step in which a feasible region is approximated using a polyhedron was made simple. This was because having the algebraic forms of the constraints meant that their derivatives required for polyhedral approximation were also immediately available. The required polyhedral approximations could be determined using (2.19) through (2.22).

Algorithm

The yield optimization algorithm for solving (5.1) followed the methods and steps described in Chapter 2, and it was a modification of the MATLAB code developed by Seifi et al. for their various applications in [17, 59, 64]. The algorithm was iterative (for nonconvex problems) and started with a hypothesized design centre (nominal design point). At the end of each iteration, the solution was used as the new nominal design point for the next iteration. An iterative process allowed the polyhedral approximation step in the yield optimization algorithm to be based on a previously converged nominal design point rather than an initial guess. The details of the algorithm are described as follows.

For each feasible region in Fig. 5.2, the algorithm began by finding a polyhedral approximation of the region by determining the appropriate expansion point for each constraint based on a hypothesized design centre. Point A, B, and C from SBAO were used as the initial design centres. The expansion points were used to linearize the constraints and were solved iteratively using a fixed-point method. With a polytope approximating the

feasible region obtained and under specified design variable tolerances, yield maximization occurred using MATLAB's *fmincon* function to solve the constrained optimization problem. The tolerances for UFC spacing and room spacing were assumed to be 0.2 and 3 m, respectively. Since their distributions did not affect the results, an arbitrary Kumaraswamy distribution was used as that allowed for a closed-form CDF to be used when calculating the yield. The algorithm sought a location for the tolerance box such that maximum yield was achieved (100% in this problem) and that the design centre was at smaller values of UFC spacing and room spacing (low penalty). In doing so, an optimal nominal design point was determined, and a maximum yield box was also identified. This entire process was then repeated for a specified number of iterations using the recently determined nominal point in the polyhedral approximation step.

Results

The value of θ in (5.1) that was used during yield optimization here was 0.8, which put a higher weighting on UFC spacing over room spacing. This was chosen because reducing the cost of the repository was considered to be important here, and UFC spacing has a greater influence on the overall cost of the DGR. Larger UFC spacing would lead to more placement rooms; therefore, more land space and excavation of the host rock would be required. Since the excavation cost for placement rooms would greatly exceed the cost of acquiring more land for sparser rooms (cf. [69] and [70]) and because larger room spacing would only require more land space (ignoring excavation for support tunnels), reducing UFC spacing was of greater interest.

The yield optimization results for the three feasible regions of interest are visualized in Fig. 5.4 and their corresponding nominal design points are summarized in Table 5.3. Note that since 100% yield was achievable, the maximum yield box was the same as the tolerance box.

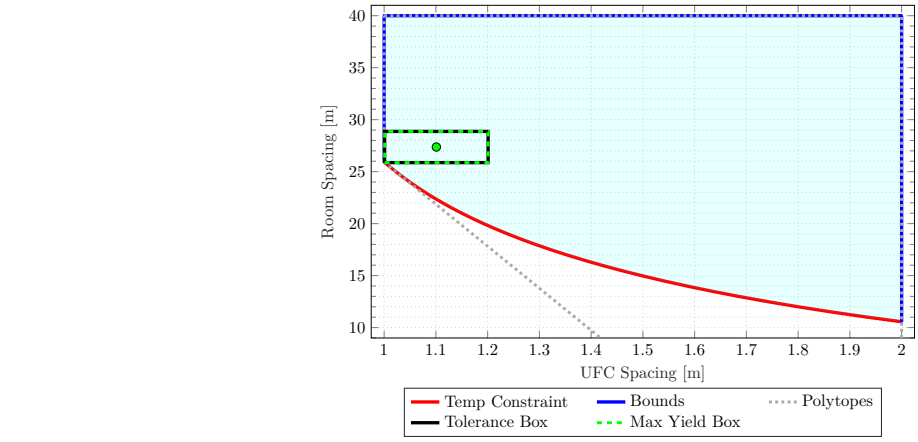

(a) $R_{A,\,a=0.25}$

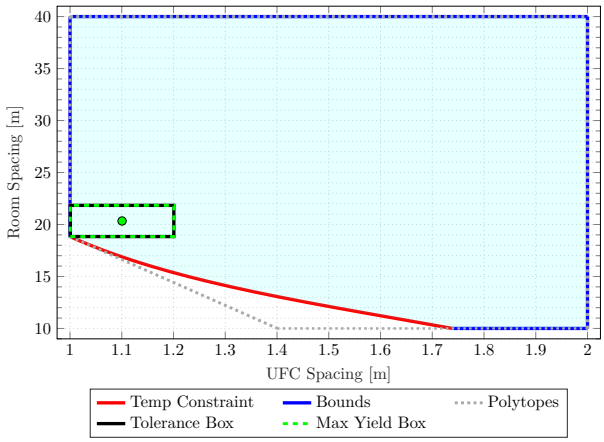

(b) $R_{A,\,a=1.25}$

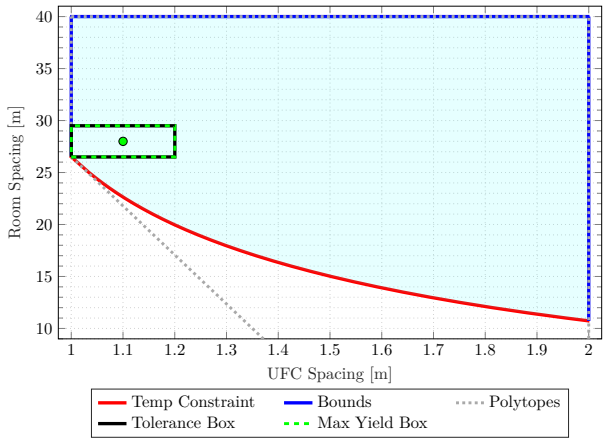

(c) $R_{A,\,a=4.00}$

Figure 5.4: Worst-case design yield optimization results for various feasible regions

Table 5.3: Worst-case design nominal points for various feasible regions

Feasible Region	Nominal Design Point (x_1, x_2)
$R_{A,\,a=0.25}$	(1.10,27.4)
$R_{A,\,a=1.25}$	(1.10,20.3)
$R_{A,\,a=4.00}$	(1.10,28.0)

Using tolerances of $x_1 \pm 0.1$ and $x_2 \pm 1.5$.

With a higher weighting for smaller values of UFC spacing, the worst-case designs specified that the nominal design points should be toward the intersections of the maximum temperature constraint and the UFC spacing lower bound. By incorporating the uncertainties of the design variables into the design, the new nominal points found are more robust than the deterministically identified optimal points mentioned in the previous section. Should the true tolerances on UFC spacing and room spacing be 0.2 and 3 m, respectively, the nominal design points listed in Table 5.3 will lead to no system failure of the DGR regardless of the distributions of the design variables.

5.3.2 Design with Failure Allowance

The nominal design points found through the worst-case design in the previous subsection led to 100% yields based on the assumptions made on the design variable tolerances. Though no system failure is undoubtedly desirable, sacrificing yield to allow for some chance of system failure may be advantageous for certain aspects in an engineering project. One clear advantage would be a reduction in cost. For the problem discussed, suppose that some failure probability is allowed. The nominal design points in Fig. 5.4 would then shift closer toward the bottom left of the feasible regions, further reducing the repository size and cost. In this subsection, designs with failure allowance are considered, and nominal design points for the feasible regions of interest that approximately lead to failure probabilities of 1, 3, and 5% are determined. Since non-failure was not the target, the distributions of the design variables would influence the results. Thus, the distribution cases in Table 5.1 were considered.

Problem Formulation

For the yield optimization process to allow a specified system failure probability, the objective was to maximize yield to a certain degree such that some portion of the tolerance box was outside its feasible region. This was done by modifying the yield maximization problem in (5.1) to include an upper bound on the predicted yield (determined by the maximum yield box). This new constraint was:

$$Y(\boldsymbol{x}^r, \boldsymbol{x}^l, \boldsymbol{x}^u) \leq 1 - F^T$$

where F^T is the target failure probability. While this modification was simple, it is cautioned that since the maximum yield box is rectangular, the predicted yield would only approximate the actual portion of the tolerance box that would be inside the feasible region (or inversely, the actual portion of the tolerance that would be beyond the feasible region). However, for

small failure probabilities, the approximation should be acceptable. The full formulation for designing with failure allowance was then:

$$\begin{aligned} \max_{\boldsymbol{x}^r, \boldsymbol{x}^l, \boldsymbol{x}^u} \quad & Y(\boldsymbol{x}^r, \boldsymbol{x}^l, \boldsymbol{x}^u) - \frac{1}{100}\left(\frac{\theta(X_{0,1} - x_1^L)}{x_1^U - x_1^L} + \frac{(1-\theta)(X_{0,2} - x_2^L)}{x_2^U - x_2^L}\right) \\ \text{s.t.} \quad & Y(\boldsymbol{x}^r, \boldsymbol{x}^l, \boldsymbol{x}^u) \leq 1 - F^T \\ & \boldsymbol{A}^+ \boldsymbol{x}^u - \boldsymbol{A}^- \boldsymbol{x}^l \leq \boldsymbol{c} \\ & \boldsymbol{x}^u \leq \boldsymbol{x}^r + \boldsymbol{t} \\ & \boldsymbol{x}^r \leq \boldsymbol{x}^l \leq \boldsymbol{x}^u \end{aligned} \tag{5.2}$$

and the value of θ considered was 0.8 again for comparability. The failure probabilities, F^T, of 1, 3, and 5% were considered.

Algorithm

Solving the design with failure allowance problem of (5.2) required the same steps used to solve the yield maximization problem of (5.1). For each feasible region in Fig. 5.2, its polyhedral approximation based on a hypothesized design centre was first obtained. The nominal design points determined for the yield maximization problems in Table 5.3 of the previous subsection were used as the initial design centres here. Under tolerances of 0.2 and 3 m for UFC spacing and room spacing, respectively, and for specified Kumaraswamy distributions for the design variables from Table 5.1, the constrained maximization problem was solved using MATLAB's *fmincon* function to reach one of the target failure probabilities. The yield was calculated using closed-form Kumaraswamy CDFs. The algorithm placed the tolerance box such that an approximate portion corresponding to the target failure probability was beyond the maximum temperature constraint. The resulting design centre was then the optimal nominal design point. The process was repeated from the polyhedral approximation step using the newly found nominal point for a specified number of iterations. In the end, to evaluate the actual yield of a solution, Monte Carlo simulation was performed about the final nominal design point.

Results

Table 5.4 lists the yield optimization results for designs with failure allowances of 1, 3, and 5%. By observing each row of the table, it can be seen that as the failure allowance increased, the nominal design points shifted toward smaller values of UFC spacing and room spacing (bottom left of the feasible regions in Fig. 5.2) as expected. As a nominal design point

shifted closer to the bottom left of its feasible region, it was more likely that a realized design point would be beyond its feasible boundaries. Considering that a nominal design point with small values for UFC spacing and room spacing gives a smaller and cheaper repository, the yield optimization performed here provided an understanding of the trade-off between yield and cost. Thus, the practicality and significance of yield optimization as part of the design process for the DGR was demonstrated.

Table 5.4: Design with failure allowance results for various feasible regions and design variable distributions

Feasible Region	Case	1% Failure Design		3% Failure Design		5% Failure Design	
		Nominal Point (x_1, x_2)	MC Yield	Nominal Point (x_1, x_2)	MC Yield	Nominal Point (x_1, x_2)	MC Yield
$R_{A,\,a=0.25}$	1	(1.10,27.42)	99.4%	(1.09,27.42)	96.3%	(1.09,27.38)	94.6%
	2	(1.08,27.35)	99.3%	(1.07,27.31)	96.7%	(1.07,27.28)	94.6%
	3	(1.01,26.46)	99.3%	(1.00,26.33)	97.0%	(1.00,26.21)	94.8%
	4	(1.10,27.31)	99.6%	(1.10,27.06)	99.2%	(1.10,27.00)	95.6%
	5	(1.02,27.35)	99.3%	(1.00,27.35)	96.3%	(0.99,27.38)	94.5%
	6	(1.08,27.36)	99.3%	(1.07,27.31)	96.9%	(1.07,27.27)	94.6%
$R_{A,\,a=1.25}$	1	(1.10,20.34)	99.3%	(1.09,20.34)	97.4%	(1.09,20.34)	94.6%
	2	(1.08,20.27)	99.3%	(1.07,20.23)	96.7%	(1.07,20.22)	94.5%
	3	(1.01,19.38)	99.3%	(1.00,19.25)	96.9%	(1.00,19.17)	94.7%
	4	(1.10,20.22)	99.5%	(1.10,20.05)	98.5%	(1.10,19.99)	96.2%
	5	(1.02,20.32)	99.3%	(1.00,20.31)	96.3%	(1.00,20.35)	94.5%
	6	(1.08,20.28)	99.3%	(1.07,20.23)	96.9%	(1.07,20.20)	94.6%
$R_{A,\,a=4.00}$	1	(1.10,28.00)	99.3%	(1.09,28.00)	96.3%	(1.09,28.00)	94.4%
	2	(1.08,27.93)	99.3%	(1.07,27.89)	96.9%	(1.07,27.86)	94.6%
	3	(1.01,27.04)	99.3%	(1.00,26.88)	96.8%	(1.00,26.82)	94.8%
	4	(1.10,27.84)	99.7%	(1.10,27.62)	99.3%	(1.10,27.60)	95.9%
	5	(1.02,28.00)	99.3%	(1.00,27.95)	96.3%	(1.00,27.77)	95.1%
	6	(1.08,27.95)	99.3%	(1.07,27.90)	96.5%	(1.07,27.85)	94.6%

Distribution parameters for each case are from Table 5.1. Using tolerances of $x_1 \pm 0.1$ and $x_2 \pm 1.5$.
Total of 1000 Monte Carlo simulations performed.

To emphasize the importance of assuming appropriate distributions for the design variables, some yield optimization results (Case 1, 3, and 5) for feasible region $R_{A,\,a=0.25}$ from Table 5.4 are visualized in Fig. 5.5. Plots for the remaining cases (Case 2, 4, and 6) of feasible region $R_{A,\,a=0.25}$ can be found in Appendix B.2.

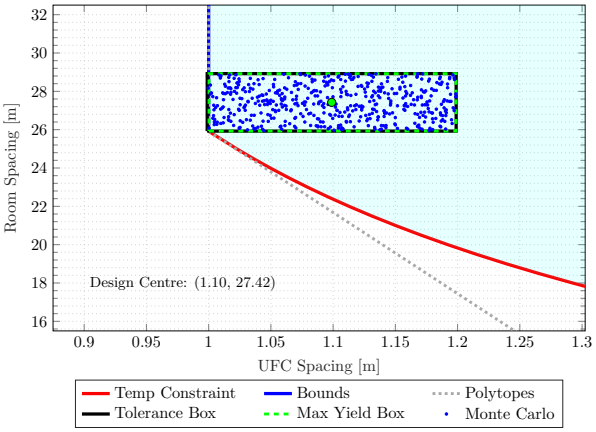

(a) 1% Design Failure, Case 1

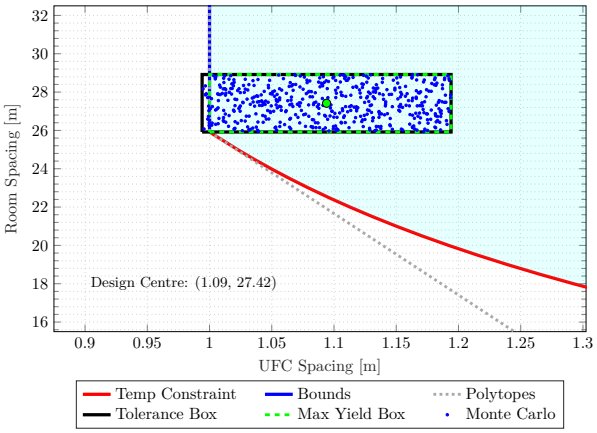

(b) 3% Design Failure, Case 1

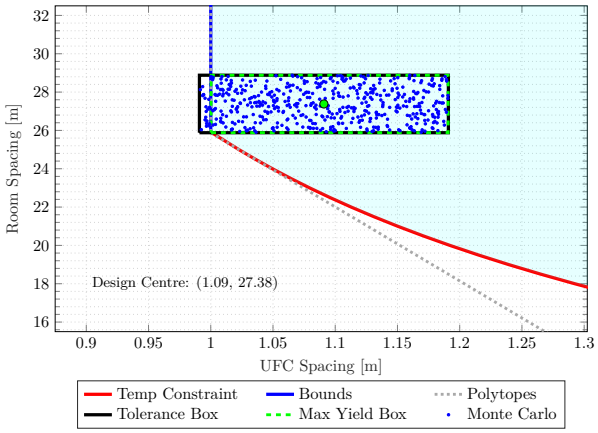

(c) 5% Design Failure, Case 1

Distribution parameters for each case are from Table 5.1. 500 Monte Carlo simulations shown.
Magenta arrows in (d)–(i) show the changes in design centre locations relative to those of Case 1 (uniform distribution).

Figure 5.5: Design with failure allowance results for feasible region $R_{A,\,a=0.25}$ under various design variable distributions

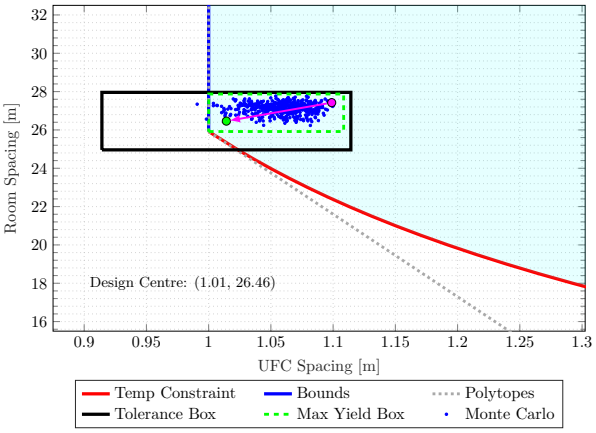

(d) 1% Design Failure, Case 3

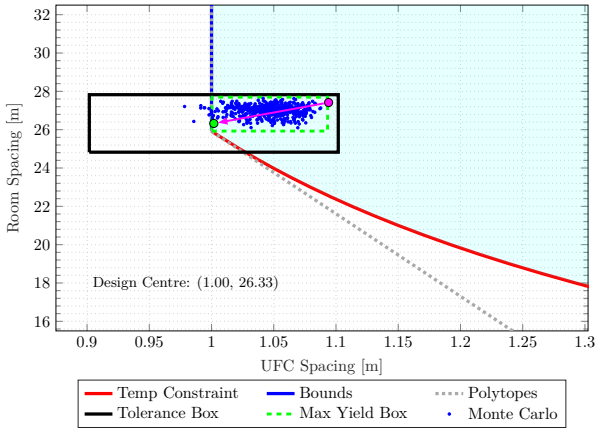

(e) 3% Design Failure, Case 3

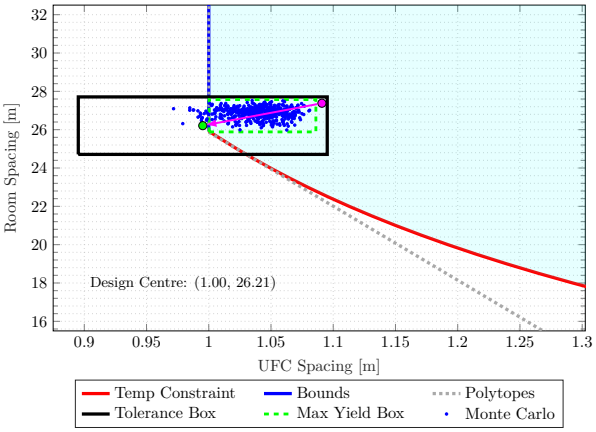

(f) 5% Design Failure, Case 3

Distribution parameters for each case are from Table 5.1. 500 Monte Carlo simulations shown.
Magenta arrows in (d)–(i) show the changes in design centre locations relative to those of Case 1 (uniform distribution).

Figure 5.5: (Continued)

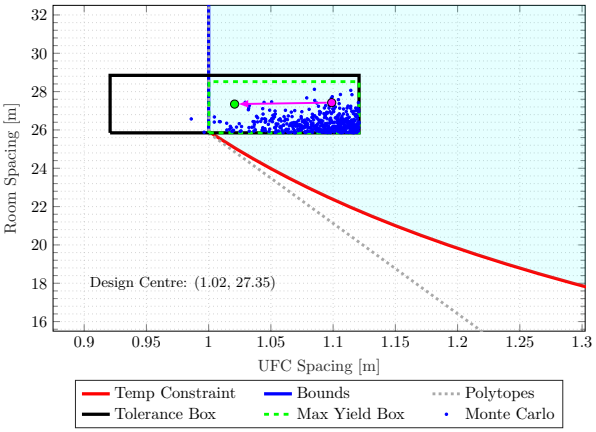

(g) 1% Design Failure, Case 5

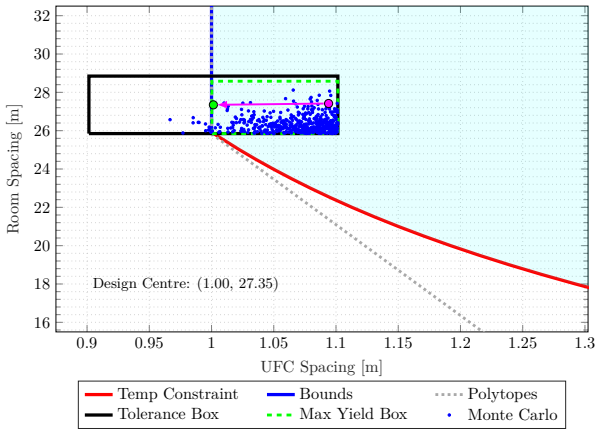

(h) 3% Design Failure, Case 5

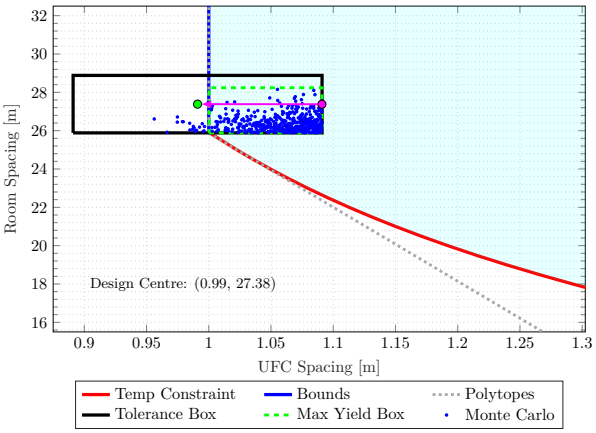

(i) 5% Design Failure, Case 5

Distribution parameters for each case are from Table 5.1. 500 Monte Carlo simulations shown.
Magenta arrows in (d)–(i) show the changes in design centre locations relative to those of Case 1 (uniform distribution).

Figure 5.5: (Continued)

Depending on the assumed distributions for UFC spacing and room spacing, the location of the resulting optimal nominal design point changes. In the first three subfigures of Fig. 5.5 (Case 1), the design variables were assumed to be uniformly distributed. There was an equal probability for a realized point to be in the bottom-left corner of the tolerance box versus anywhere else. In this case, the spread of the design variables' values led to the design centres being far away from the boundaries of the feasible region to ensure adequate yields. For distributions with high kurtosis, the distributions of the design variables' values are concentrated in the design space; thus, realized values are likely to fall within a certain area of the tolerance box. Yield optimization takes advantage of this by potentially choosing a design centre closer to the boundaries of the feasible region. This is seen in the remaining subfigures of Fig. 5.5. In Fig. 5.5d–5.5f (Case 3), the distributions of the design variables were highly kurtotic for large values meaning realized points were likely to be in the top-right portion of the tolerance box. This allowed the design centres to move closer to the bottom-left of the feasible region as it was less likely that extreme small values for the design variables would occur. In Fig. 5.5g–5.5i (Case 5), the distributions of the design variables were highly skewed as they follow tail distributions. Realized points were likely to lie at the bottom-right corner of the tolerance box for this case, which led to the design centres shifting left. The relative movements of the design centres from Case 1 over to Case 3 and 5 are revealed in Fig. 5.5d–5.5i using magenta arrows. In some designs with more liberal failure allowances, their design centres might even lie outside their feasible regions but still have high probabilities for realized points to be within them. This is exemplified in Fig. 5.5f and 5.5i.

5.4 Summary

This chapter began with an analysis of the yields of the optimal design points determined via SBAO in the chapter prior. These points were attractive design options as they suggested the smallest possible combinations of UFC spacing and room spacing, meaning the DGR would be smaller and cheaper to manufacture and construct. However, the yield analysis revealed that should the manufacturing and construction of the DGR be with design variables that inherently have variabilities, the deterministically identified optimal design points would not be as desirable as once thought. Thus, the stochastic nature of the design variables needed to be considered, and this was done through the use of yield optimization.

New nominal design points were identified under arbitrary assumptions of design variable tolerances and distributions. As only one main constraint (maximum temperature constraint) was of concern, the feasible regions were bounded through specifying upper and lower bounds on the design variables. This led to large feasible regions resulting in yield optimization finding the same nominal design points regardless of the design variables' distributions, all with 100% yields (i.e., no system failure). When some probability of failure was allowed in the design (between 1 and 5% failure probability), the distributions of the design variables were ultimately significant in the yield optimization process, and different nominal design points were found for the various distribution cases considered. Overall, the yield optimization in this chapter demonstrated that the variabilities in design variables should be considered in the repository design process and that appropriate tolerances and distributions need to be used to represent them.

Chapter 6

Conclusion

The objective of this thesis was to determine optimal designs for the spatial arrangement of UFCs in a conceptual Canadian DGR such that a maximum temperature criterion was satisfied over the lifetime of the repository (one million years) to prevent system failure. The criterion was that no part of the DGR beyond the surfaces of the placed UFCs could exceed a temperature of 100 °C as radioactive decay occurred inside the containers. In terms of spatial arrangement, the spacing between UFCs (UFC spacing), the separation between placement rooms underground (room spacing), and the locations of variously aged UFCs that generate heat at different rates (shape parameter) were the three design variables of concern for the design optimization.

Due to high computational requirements for solving a large finite element model and even more intense requirements when optimizing it, a compact model was first created in Chapter 3. This model ignored insignificant components of the DGR, made use of symmetries within the DGR, and reduced the required simulation time far down from one million years by noticing that the maximum temperature within the DGR occurred at around 40–45 years after placement of the UFCs. The final model required approximately two hours to solve on the machine used (Intel Core i5-3230M CPU).

In Chapter 4, two cases were studied through surrogate optimization: (i) UFCs all having been 30 years since discharged from a nuclear power reactor and (ii) UFCs being between 30 and 60 years since discharged. For the first case, a trade-off curve bordering the feasible region was identified, allowing the determination of optimal combinations of UFC spacing and room spacing that result in maximum temperatures just below 100 °C. A cubic polynomial surrogate function was used and 16 evaluations (requiring about 32 hours) were performed in total to reach convergence (within 0.5 °C), significantly less than if the entire

design space was explored without SBAO (341 discrete points requiring roughly 700 hours). For the second case, sinusoidal (ii.a) and Kumaraswamy PDF-like (ii.b) arrangements of the variously aged UFCs were explored by parameterizing the UFC age at each location in a placement room using a shape parameter. Cubic RBF surrogate functions were used, and it was determined that within the bounds studied: (ii.a) the alternating frequency for sinusoidally placing UFCs by age did not affect the maximum temperature significantly and (ii.b) the minimum UFC spacings required at room spacings of 15, 20, and 25 m when placing UFCs by age in a Kumaraswamy PDF-like arrangement were 1.6, 1.3, and 1.1 m, respectively.

When the design variables of UFC spacing and room spacing were considered as random variables having assumed tolerances of 0.2 and 3 m, respectively, the deterministic designs determined through surrogate optimization had appreciable probabilities of system failure since the identified design points were very close to the boundaries of their feasible regions. Yield optimization was performed in Chapter 5 to incorporate a stochastic aspect into the analysis and to determine more robust design points. New nominal design points were suggested based on several levels of allowed failure probabilities under various assumed distributions for the design variables, shifting the design centres more into the feasible regions as higher yields were explored.

The work presented in this thesis serves as methods that can be considered for the currently ongoing design process for Canada's DGR. As the DGR site selection process by NWMO continues and as design criteria are eventually finalized, more detailed information and constraints for the conceptual repository will become available. These pave the way for future work, and the following are recommended:

- Extend the design space to higher dimensions to include design variables that reflect other modes of system failure such as corrosion and deformation.
- Analyse the effects of varying the UFCs' internal fuel bundle distributions on the maximum temperature evolved.
- Couple the effects of multiple physical processes.
- Explore other surrogate functions beyond polynomial functions and RBFs, e.g., artificial neural networks for higher-dimensional problems.
- Investigate yield for correlated random variables.
- Study the effects of the model parameters on yield.
- Consider the temperature effects on the material properties in the model.
- Use multi-objective optimization to minimize multiple objectives such as repository size, cost, and yield.

References

[1] G. L. Brooks, "A short history of the CANDU nuclear power system," Atomic Energy of Canada Ltd., Tech. Rep. AECL–10788, January 1993.

[2] *Country Nuclear Power Profiles*, ser. Non-serial Publications. Vienna: International Atomic Energy Agency, 2019.

[3] *Pan-Canadian Framework on Clean Growth and Climate Change: Canada's Plan to Address Climate Change and Grow the Economy.* Environment and Climate Change Canada, 2016.

[4] NWMO, "Description of a deep geological repository and centre of expertise for Canada's used nuclear fuel," 2015.

[5] NWMO, "Moving towards partnership: Annual report 2018," March 2018.

[6] *Nuclear Fuel Waste Act*, SC 2002, c. 23, s. 6.

[7] NWMO, "Choosing a way forward: The future management of Canada's used nuclear fuel (final study)," November 2005.

[8] J. Noronha, "Deep geological repository conceptual design report: Crystalline/sedimentary rock environment," Nuclear Waste Management Organization, Tech. Rep. APM-REP-00440-0015 R001, May 2016.

[9] NWMO, "Implementing adaptive phased management 2019 to 2023," March 2019.

[10] NWMO, "Ensuring safety: Multiple-barrier system," 2015.

[11] D. S. Hall and P. G. Keech, "An overview of the Canadian corrosion program for the long-term management of nuclear waste," *Corrosion Engineering, Science and Technology*, vol. 52, no. sup1, pp. 2–5, 2017.

[12] T. Standish, J. Chen, R. Jacklin, P. Jakupi, S. Ramamurthy, D. Zagidulin, P. Keech, and D. Shoesmith, "Corrosion of copper-coated steel high level nuclear waste containers under permanent disposal conditions," *Electrochimica Acta*, vol. 211, pp. 331–342, 2016.

[13] J. Garcia, K. Ponnambalam, and M. Sivaraman, "Lifetimes of used fuel containers assuming sulphate reducing bacterial activity," in *Proceedings. 8th International Conference on Simulation Methods in Nuclear Science and Engineering*, 2018.

[14] SKBF/KBS, "Final storage of spent nuclear fuel—KBS-3: Summary," Swedish Nuclear Fuel Supply Co./Division KBS (SKBF/KBS), Tech. Rep. Art716 5, May 1983.

[15] N. V. Queipo, R. T. Haftka, W. Shyy, T. Goel, R. Vaidyanathan, and P. K. Tucker, "Surrogate-based analysis and optimization," *Progress in Aerospace Sciences*, vol. 41, no. 1, pp. 1–28, 2005.

[16] S. Lin and K. Ponnambalam, "Surrogate-based optimization for spacing parameters of the Canadian deep geological repository," in *Proceedings. 4th Nuclear Waste Management, Decommissioning and Environmental Restoration Conference*, 2019.

[17] A. Seifi, K. Ponnambalam, and J. Vlach, "Maximization of manufacturing yield of systems with arbitrary distributions of component values," *Annals of Operations Research*, vol. 99, no. 1, pp. 373–383, Dec 2000.

[18] M. Ion, "Nuclear fuel waste projections in Canada: 2018 update," Nuclear Waste Management Organization, Tech. Rep. NWMO-TR-2018-18, December 2018.

[19] Acres Consulting Services Ltd. in conjunction with RE/SPEC Ltd., "A feasibility study of the multilevel vault concept," Atomic Energy of Canada Limited, Tech. Rep. TR-297, 1985.

[20] W. G. Mathers, "HOTROK, a program for calculating the transient temperature field from an underground nuclear waste disposal vault," Atomic Energy of Canada Limited, Tech. Rep. TR-366, 1985.

[21] K. K. Tsui and A. Tsai, "Thermal analyses for different options of nuclear fuel waste placement," Atomic Energy of Canada Limited, Tech. Rep. AECL-7823, 1985.

[22] Acres Consulting Services Ltd., "A preliminary study of long-hole emplacement alternatives," Atomic Energy of Canada Limited, Tech. Rep. TR-346, 1993.

[23] P. Baumgartner, T. V. Tran, and R. Burgher, "Sensitivity analyses for the thermal response of a nuclear fuel waste disposal vault," Atomic Energy of Canada Limited, Tech. Rep. TR-621, COG-94-258, 1994.

[24] J. H. Park, J. E. Kuh, S. Kwon, and C. H. Kang, "Thermal analysis of high level radioactive waste repository using a large model," *Journal of the Korean Nuclear Society*, vol. 32, no. 3, pp. 244–253, 2000.

[25] R. Guo, "Numerical modelling of a deep geological repository using the in-floor borehole placement method," Nuclear Waste Management Organization, Tech. Rep. NWMO-TR-2007-14, December 2007.

[26] R. Guo, "Sensitivity analyses to investigate the influence of the container spacing and tunnel spacing on the thermal response in a deep geological repository," Nuclear Waste Management Organization, Tech. Rep. NWMO-TR-2008-24, December 2008.

[27] H. Hökmark, M. Lönnqvist, and B. Fälth, "THM-issues in repository rock: Thermal, mechanical, thermo-mechanical and hydro-mechanical evolution of the rock at the Forsmark and Laxemar sites," Swedish Nuclear Fuel and Waste Management Co., Tech. Rep. SKB TR-10-23, May 2010.

[28] R. Guo, "Thermal response of a Mark II conceptual deep geological repository in crystalline rock," Nuclear Waste Management Organization, Tech. Rep. NWMO-TR-2016-03, March 2016.

[29] R. Guo, "Thermal response of a Canadian conceptual deep geological repository in crystalline rock and a method to correct the influence of the near-field adiabatic boundary condition," *Engineering Geology*, vol. 218, pp. 50–62, 2017.

[30] SKB, "Final repository facility: Underground design premises/D2," Swedish Nuclear Fuel and Waste Management Co., Tech. Rep. SKB R-07-33, 2007.

[31] X. Zhou, D. Sun, Y. Tan, and A. Zhou, "Canister spacing in high-level radioactive nuclear waste repository," *Annals of Nuclear Energy*, vol. 141, p. 107335, 2020.

[32] K. Crump, "Numerical inversion of Laplace transforms using a Fourier series approximation," *Journal of the ACM (JACM)*, vol. 23, no. 1, pp. 89–96, 1976.

[33] H. Hökmark and B. Fälth, "Thermal dimensioning of the deep repository: Influence of canister spacing, canister power, rock thermal properties and nearfield design on the maximum canister surface temperature," Swedish Nuclear Fuel and Waste Management Co., Tech. Rep. SKB TR-03-09, 2003.

[34] S. Koziel, D. E. Ciaurri, and L. Leifsson, "Surrogate-based methods," in *Computational Optimization, Methods and Algorithms*, ser. Studies in Computational Intelligence. Berlin, Heidelberg: Springer Berlin Heidelberg, 2011, vol. 356, pp. 33–59.

[35] K. K. Vu, C. D'Ambrosio, Y. Hamadi, and L. Liberti, "Surrogate-based methods for black-box optimization," *International Transactions in Operational Research*, vol. 24, no. 3, pp. 393–424, 2017.

[36] G. Rudolph, "Convergence of evolutionary algorithms in general search spaces," in *Proceedings of IEEE International Conference on Evolutionary Computation*, 1996, pp. 50–54.

[37] R. Yang, "Convergence of the simulated annealing algorithm for continuous global optimization," *Journal of Optimization Theory and Applications*, vol. 104, no. 3, pp. 691–716, 2000.

[38] S. Hanafi, "On the convergence of tabu search," *Journal of Heuristics*, vol. 7, no. 1, pp. 47–58, 2001.

[39] C. Audet and J. E. Dennis, "Mesh adaptive direct search algorithms for constrained optimization," *SIAM Journal on Optimization*, vol. 17, no. 1, pp. 188–217, 2006.

[40] J. A. Nelder and R. Mead, "A simplex method for function minimization," *The Computer Journal*, vol. 7, no. 4, pp. 308–313, 01 1965.

[41] A. R. Conn, K. Scheinberg, and L. N. Vicente, "Global convergence of general derivative-free trust-region algorithms to first- and second-order critical points," *SIAM Journal on Optimization*, vol. 20, no. 1, pp. 387–415, 2009.

[42] S. Koziel and L. Leifsson, *Simulation-Driven Design by Knowledge-Based Response Correction Techniques*. Cham: Springer International Publishing, 2016.

[43] B. Husslage, G. Rennen, E. Dam, and D. Hertog, "Space-filling Latin hypercube designs for computer experiments," *Optimization and Engineering*, vol. 12, no. 4, pp. 611–630, 2011.

[44] K. Q. Ye, "Orthogonal column Latin hypercubes and their application in computer experiments," *Journal of the American Statistical Association*, vol. 93, no. 444, pp. 1430–1439, 1998.

[45] M. D. McKay, R. J. Beckman, and W. J. Conover, "Comparison of three methods for selecting values of input variables in the analysis of output from a computer code," *Technometrics*, vol. 21, no. 2, pp. 239–245, 1979.

[46] M. Johnson, L. Moore, and D. Ylvisaker, "Minimax and maximin distance designs," *Journal of Statistical Planning and Inference*, vol. 26, no. 2, pp. 131–148, 1990.

[47] A. I. Forrester and A. J. Keane, "Recent advances in surrogate-based optimization," *Progress in Aerospace Sciences*, vol. 45, no. 1, pp. 50–79, 2009.

[48] J. Müller, "MATSuMoTo: The MATLAB surrogate model toolbox for computationally expensive black-box global optimization problems," *arXiv e-prints*, p. arXiv:1404.4261, Apr 2014.

[49] J. Müller and R. Piché, "Mixture surrogate models based on Dempster-Shafer theory for global optimization problems," *Journal of Global Optimization*, vol. 51, no. 1, pp. 79–104, 2011.

[50] J. Müller, C. A. Shoemaker, and R. Piché, "SO-MI: A surrogate model algorithm for computationally expensive nonlinear mixed-integer black-box global optimization problems," *Computers and Operations Research*, vol. 40, no. 5, pp. 1383–1400, 2013.

[51] J. Müller, C. Shoemaker, and R. Piché, "SO-I: a surrogate model algorithm for expensive nonlinear integer programming problems including global optimization applications," *Journal of Global Optimization*, vol. 59, no. 4, pp. 865–889, 2014.

[52] J. Müller and C. Shoemaker, "Influence of ensemble surrogate models and sampling strategy on the solution quality of algorithms for computationally expensive black-box global optimization problems," *Journal of Global Optimization*, vol. 60, no. 2, pp. 123–144, 2014.

[53] Z. H. Han and K. S. Zhang, "Surrogate-based optimization," in *Real-World Applications of Genetic Algorithms*, O. Roeva, Ed. Rijeka: IntechOpen, 2012, ch. 17.

[54] R. L. Hardy, "Multiquadric equations of topography and other irregular surfaces," *Journal of Geophysical Research (1896-1977)*, vol. 76, no. 8, pp. 1905–1915, 1971.

[55] S. Bagheri, W. Konen, and T. Bäck, "Comparing kriging and radial basis function surrogates," in *Proceedings. 27. Workshop Computational Intelligence*, 2017, pp. 243–259.

[56] C. A. Micchelli, "Interpolation of scattered data: Distance matrices and conditionally positive definite functions," *Constructive Approximation*, vol. 2, no. 1, pp. 11–22, Dec 1986.

[57] M. J. D. Powell, "Radial basis function methods for interpolation to functions of many variables," in *HERCMA*, October 2001.

[58] D. Brockhoff, "Comparison of the MATSuMoTo library for expensive optimization on the noiseless black-box optimization benchmarking testbed," in *2015 IEEE Congress on Evolutionary Computation (CEC)*, May 2015, pp. 2026–2033.

[59] K. Ponnambalam, A. Seifi, and J. Vlach, "Probabilistic design of systems with general distributions of parameters," *International Journal of Circuit Theory and Applications*, vol. 29, no. 6, pp. 527–536, 2001.

[60] H. L. Abdel-Malek and J. W. Bandler, "Yield estimation for efficient design centring assuming arbitrary statistical distributions," *International Journal of Circuit Theory and Applications*, vol. 6, no. 3, pp. 289–303, 1978.

[61] S. W. Director, W. Maly, and A. J. Strojwas, *VLSI Design for Manufacturing: Yield Enhancement*, ser. The Kluwer International Series in Engineering and Computer Science. Boston: Kluwer Academic Publishers, 1990.

[62] S. W. Director, P. Feldmann, and K. Krishna, "Optimization of parametric yield: A tutorial," in *1992 Proceedings of the IEEE Custom Integrated Circuits Conference*, May 1992, pp. 3.1.1–3.1.8.

[63] J. Wojciechowski, J. Vlach, and L. Opalski, "Design for nonsymmetrical statistical distributions," *IEEE Transactions on Circuits and Systems I: Fundamental Theory and Applications*, vol. 44, no. 1, pp. 29–37, Jan 1997.

[64] A. Seifi, K. Ponnambalam, and J. Vlach, "Optimization of filter designs with dependent and asymmetrically distributed parameters," *Journal of the Franklin Institute*, vol. 350, no. 2, pp. 378–396, 2013.

[65] P. Kumaraswamy, "A generalized probability density function for double-bounded random processes," *Journal of Hydrology*, vol. 46, no. 1, pp. 79–88, 1980.

[66] M. Gobien, F. Garisto, E. Kremer, and C. Medri, "Sixth case study: Reference data and codes," Nuclear Waste Management Organization, Tech. Rep. NWMO-TR-2016-10, December 2016.

[67] F. Garisto, "Sixth case study: Features, events and processes," Nuclear Waste Management Organization, Tech. Rep. NWMO-TR-2017-08, July 2017.

[68] J. C. Tait, H. Roman, and C. A. Morrison, "Characteristic and radionuclide inventories of used fuel from OPG nuclear generation stations," Ontario Power Generation, Nuclear Waste Management Division, Tech. Rep. 06819-REP-01200-10029-R00, 2000.

[69] D. Heimlich, "APM 2016 lifecycle cost estimate update summary report," Nuclear Waste Management Organization, Tech. Rep. APM-REP-00440-0202, April 2016.

[70] Statistics Canada, "Table 32-10-0047-01 Value per acre of farm land and buildings at July 1."

Appendix A

Surrogate-Based Analysis and Optimization

A.1 Sinusoidal UFC Age Arrangement

The following tables and figure show the results from SBAO for when an inventory of assorted UFC ages was arranged sinusoidally in the way of a cosine function.

Table A.1: Optimal design points using cubic RBF surrogates for a sinusoidal (cosine) age arrangement

UFC Spacing [m]	Room Spacing [m]	Shape Parameter	Predicted Maximum Temperature [°C]	Actual Maximum Temperature [°C]	Error [°C]
1.9	10	0.50	97.171	98.530	−1.359
1.9		1.00	99.943	99.943	0*
1.9		1.50	99.288	99.288	0*
1.9		2.00	99.166	99.166	0*
1.9		2.50	99.010	99.010	0*
1.9		3.00	97.059	98.957	−1.898
1.9		3.50	97.844	98.855	−1.011
1.9		4.00	97.623	98.840	−1.217
1.9		4.50	97.089	98.905	−1.816
1.9		5.00	97.360	98.884	−1.524
1.9		5.50	97.349	98.926	−1.577
1.9		6.00	96.847	98.900	−2.053
1.9		6.50	97.818	98.937	−1.119
1.9		7.00	97.911	98.911	−1.000
1.9		7.50	98.377	98.943	−0.566
1.9		8.00	98.993	98.993	0*
1.9		8.50	99.028	99.028	0*
1.9		9.00	99.000	99.000	0*

Table A.1: (Continued)

UFC Spacing [m]	Room Spacing [m]	Shape Parameter	Predicted Maximum Temperature [°C]	Actual Maximum Temperature [°C]	Error [°C]
1.9	10	9.50	98.063	99.032	−0.969
1.9		10.00	98.933	98.933	0*
1.3	15	0.50	98.515	98.515	0*
1.4		1.00	97.783	97.467	+0.316
1.4		1.50	96.958	96.165	+0.793
1.4		2.00	96.004	95.721	+0.283
1.4		2.50	95.925	95.386	+0.539
1.4		3.00	95.715	95.250	+0.465
1.4		3.50	95.368	95.047	+0.321
1.4		4.00	96.802	94.994	+1.808
1.4		4.50	97.604	94.895	+2.709
1.4		5.00	95.917	94.828	+1.089
1.4		5.50	94.674	94.747	−0.073
1.4		6.00	96.751	94.687	+2.064
1.4		6.50	97.806	94.647	+3.159
1.4		7.00	95.578	94.582	+0.996
1.4		7.50	94.880	94.545	+0.335
1.3		8.00	99.727	100.664	−0.937
1.3		8.50	99.822	100.605	−0.783
1.4		9.00	94.476	94.402	+0.074
1.4		9.50	93.877	94.338	−0.461
1.4		10.00	94.306	94.306	0*
1.1	20	0.50	93.993	93.993	0*
1.1		1.00	97.525	100.565	−3.040
1.1		1.50	99.013	99.013	0*
1.1		2.00	98.307	98.307	0*
1.1		2.50	97.771	97.771	0*
1.1		3.00	97.427	97.427	0*
1.1		3.50	97.223	97.133	+0.090
1.1		4.00	96.641	96.926	−0.285
1.1		4.50	95.977	96.739	−0.762
1.1		5.00	96.618	96.618	0*
1.1		5.50	98.220	96.486	+1.734
1.1		6.00	96.380	96.380	0*
1.1		6.50	97.125	96.282	+0.843
1.1		7.00	96.990	96.176	+0.814
1.1		7.50	96.105	96.105	0*
1.1		8.00	97.507	96.012	+1.495
1.1		8.50	97.611	95.953	+1.658
1.1		9.00	97.563	95.872	+1.691
1.1		9.50	95.831	95.831	0*
1.1		10.00	98.188	95.725	+2.463
1.0	25	0.50	91.454	91.454	0*
1.0		1.00	97.540	97.540	0*
1.0		1.50	95.843	95.843	0*
1.0		2.00	94.960	94.960	0*
1.0		2.50	94.606	94.422	+0.184
1.0		3.00	94.011	94.011	0*
1.0		3.50	93.144	93.716	−0.572
1.0		4.00	91.954	93.464	−1.510
1.0		4.50	90.475	93.231	−2.756
1.0		5.00	89.007	93.019	−4.012

Table A.1: (Continued)

UFC Spacing [m]	Room Spacing [m]	Shape Parameter	Predicted Maximum Temperature [°C]	Actual Maximum Temperature [°C]	Error [°C]
1.0	25	5.50	88.049	92.856	−4.807
1.0		6.00	87.440	92.709	−5.269
1.0		6.50	86.952	92.541	−5.589
1.0		7.00	86.668	92.390	−5.722
1.0		7.50	86.656	92.267	−5.611
1.0		8.00	86.923	92.168	−5.245
1.0		8.50	87.408	92.055	−4.647
1.0		9.00	87.963	91.950	−3.987
1.0		9.50	88.501	91.849	−3.348
1.0		10.00	89.082	91.757	−2.675
				Mean Absolute Error	1.302

* Zero error entries due to evaluated points being used in the RBF interpolation during SBAO.

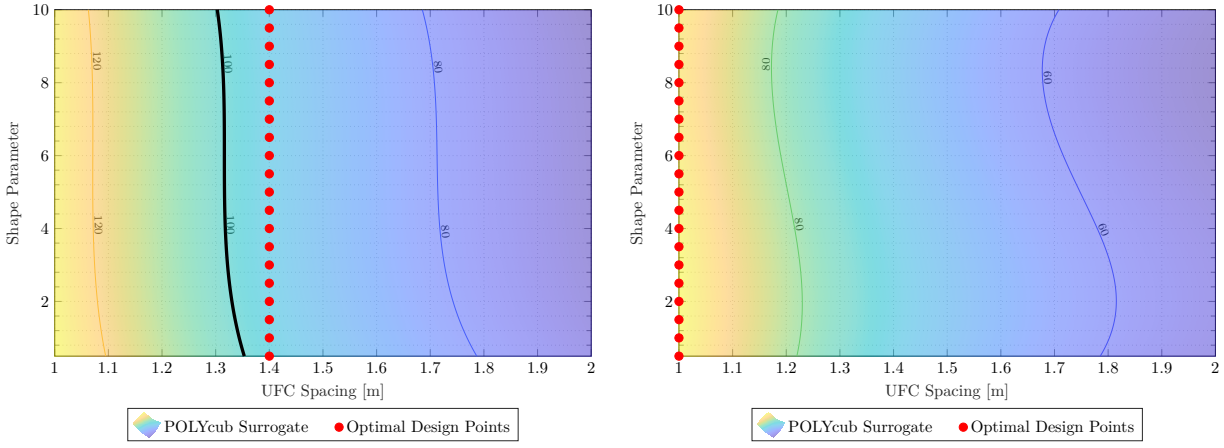

(a) Room Spacing = 15 m

(b) Room Spacing = 25 m

Figure A.1: Surrogate optimization results using cubic polynomial surrogates for a sinusoidal (cosine) UFC age arrangement (continued from Fig. 4.9)

Table A.2: Optimal design points using cubic polynomial surrogates for a sinusoidal (cosine) age arrangement

UFC Spacing [m]	Room Spacing [m]	Shape Parameter	Predicted Maximum Temperature [°C]	Actual Maximum Temperature [°C]	Error [°C]
1.9	10	0.50	98.835	98.530	+0.305
1.9		1.00	98.896	99.943	−1.047
1.9		1.50	98.928	99.288	−0.360
1.9		2.00	98.935	99.166	−0.231
1.9		2.50	98.921	99.010	−0.089
1.9		3.00	98.891	98.957	−0.066
1.9		3.50	98.849	98.855	−0.006
1.9		4.00	98.798	98.840	−0.042
1.9		4.50	98.742	98.905	−0.163
1.9		5.00	98.686	98.884	−0.198
1.9		5.50	98.634	98.926	−0.292
1.9		6.00	98.590	98.900	−0.310
1.9		6.50	98.558	98.937	−0.379
1.9		7.00	98.541	98.911	−0.370
1.9		7.50	98.545	98.943	−0.398
1.9		8.00	98.573	98.993	−0.420
1.9		8.50	98.629	99.028	−0.399
1.9		9.00	98.718	99.000	−0.282
1.9		9.50	98.843	99.032	−0.189
1.9		10.00	99.008	98.933	+0.075
1.4	15	0.50	97.166	92.135	+5.031
1.4		1.00	96.565	97.467	−0.902
1.4		1.50	96.072	96.165	−0.093
1.4		2.00	95.676	95.721	−0.045
1.4		2.50	95.367	95.386	−0.019
1.4		3.00	95.133	95.250	−0.117
1.4		3.50	94.964	95.047	−0.083
1.4		4.00	94.848	94.994	−0.146
1.4		4.50	94.777	94.895	−0.118
1.4		5.00	94.737	94.828	−0.091
1.4		5.50	94.720	94.747	−0.027
1.4		6.00	94.714	94.687	+0.027
1.4		6.50	94.708	94.647	+0.061
1.4		7.00	94.692	94.582	+0.110
1.4		7.50	94.655	94.545	+0.110
1.4		8.00	94.586	94.470	+0.116
1.4		8.50	94.475	94.432	+0.043
1.4		9.00	94.310	94.402	−0.092
1.4		9.50	94.082	94.338	−0.256
1.4		10.00	93.778	94.306	−0.528
1.1	20	0.50	94.513	93.993	+0.520
1.1		1.00	95.603	100.565	−4.962
1.1		1.50	96.418	99.013	−2.595
1.1		2.00	96.987	98.307	−1.320
1.1		2.50	97.339	97.771	−0.432
1.1		3.00	97.504	97.427	+0.077
1.1		3.50	97.511	97.133	+0.378
1.1		4.00	97.389	96.926	+0.463
1.1		4.50	97.169	96.739	+0.430
1.1		5.00	96.879	96.618	+0.261

Table A.2: (Continued)

UFC Spacing [m]	Room Spacing [m]	Shape Parameter	Predicted Maximum Temperature [°C]	Actual Maximum Temperature [°C]	Error [°C]
1.1	20	5.50	96.549	96.486	+0.063
1.1		6.00	96.208	96.380	−0.172
1.1		6.50	95.885	96.282	−0.397
1.1		7.00	95.610	96.176	−0.566
1.1		7.50	95.413	96.105	−0.692
1.1		8.00	95.323	96.012	−0.689
1.1		8.50	95.368	95.953	−0.585
1.1		9.00	95.580	95.872	−0.292
1.1		9.50	95.986	95.831	+0.155
1.1		10.00	96.616	95.725	+0.891
1.0	25	0.50	94.078	91.454	+2.624
1.0		1.00	94.397	97.540	−3.143
1.0		1.50	94.567	95.843	−1.276
1.0		2.00	94.607	94.960	−0.353
1.0		2.50	94.533	94.422	+0.111
1.0		3.00	94.364	94.011	+0.353
1.0		3.50	94.118	93.716	+0.402
1.0		4.00	93.813	93.464	+0.349
1.0		4.50	93.466	93.231	+0.235
1.0		5.00	93.095	93.019	+0.076
1.0		5.50	92.719	92.856	−0.137
1.0		6.00	92.354	92.709	−0.355
1.0		6.50	92.020	92.541	−0.521
1.0		7.00	91.733	92.390	−0.657
1.0		7.50	91.511	92.267	−0.756
1.0		8.00	91.373	92.168	−0.795
1.0		8.50	91.336	92.055	−0.719
1.0		9.00	91.418	91.950	−0.532
1.0		9.50	91.637	91.849	−0.212
1.0		10.00	92.011	91.757	+0.254
				Mean Absolute Error	0.543

A.2 Kumaraswamy PDF-Like UFC Age Arrangement

The following tables and figure show the results from SBAO for when an inventory of assorted UFC ages was arranged in the way of a Kumaraswamy PDF.

Table A.3: Optimal design points using cubic RBF surrogates for a Kumaraswamy PDF-like UFC age arrangement

UFC Spacing [m]	Room Spacing [m]	Shape Parameter	Predicted Maximum Temperature [°C]	Actual Maximum Temperature [°C]	Error [°C]
2.0	10	0.75	96.098	96.505	−0.407
1.9		1.00	96.595	96.595	0*
1.8		1.25	99.598	99.598	0*
1.9		1.50	94.715	95.916	−1.201
1.9		1.75	96.738	96.823	−0.085
1.9		2.00	99.302	100.137	−0.835
2.0		2.25	96.710	98.257	−1.547
2.0		2.50	99.203	100.080	−0.877
1.6	15	0.25	98.038	93.545	+4.493
1.5		0.50	96.317	96.092	+0.225
1.4		0.75	95.928	95.928	0*
1.3		1.00	98.673	96.656	+2.017
1.3		1.25	97.245	94.983	+2.262
1.3		1.50	97.739	96.070	+1.669
1.3		1.75	99.653	99.653	0*
1.4		2.00	95.971	96.929	−0.958
1.4		2.25	98.624	99.427	−0.803
1.5		2.50	95.695	95.480	+0.215
1.5		2.75	97.882	96.714	+1.168
1.5		3.00	99.051	97.636	+1.415
1.5		3.25	99.144	98.337	+0.807
1.5		3.50	98.878	98.878	0*
1.5		3.75	99.302	99.302	0*
1.5		4.00	99.639	99.639	0*
1.3	20	0.25	96.979	92.402	+4.577
1.1		0.50	99.346	103.988	−4.642
1.0		0.75	98.489	106.250	−7.761
1.0		1.00	94.548	96.506	−1.958
1.0		1.25	94.422	95.339	−0.917
1.0		1.50	98.808	98.657	+0.151
1.1		1.75	97.316	96.013	+1.303
1.2		2.00	93.752	92.515	+1.237
1.2		2.25	95.507	94.759	+0.748
1.2		2.50	96.599	96.336	+0.263
1.2		2.75	97.471	97.471	0*
1.2		3.00	98.448	98.306	+0.142
1.2		3.25	98.934	98.934	0*
1.2		3.50	99.416	99.416	0*
1.2		3.75	99.791	99.791	0*
1.3		4.00	94.142	93.453	+0.689
1.1	25	0.25	94.585	93.988	+0.597
1.0		0.50	99.734	99.734	0*
1.0		0.75	94.029	94.029	0*

Table A.3: (Continued)

UFC Spacing [m]	Room Spacing [m]	Shape Parameter	Predicted Maximum Temperature [°C]	Actual Maximum Temperature [°C]	Error [°C]
1.0		1.00	90.026	81.551	+8.475
1.0		1.25	88.515	81.073	+7.442
1.0		1.50	89.053	87.569	+1.484
1.0		1.75	91.128	92.864	−1.736
1.0		2.00	94.061	96.232	−2.171
1.0		2.25	97.242	98.416	−1.174
1.0	25	2.50	99.903	99.903	0*
1.1		2.75	93.580	92.900	+0.680
1.1		3.00	94.297	93.601	+0.696
1.1		3.25	94.717	94.122	+0.595
1.1		3.50	94.956	94.518	+0.438
1.1		3.75	95.733	94.823	+0.910
1.1		4.00	96.522	95.063	+1.459
				Mean Absolute Error	1.308

Kumaraswamy shape parameters a varying and $b = 1.5$.
* Zero error entries due to evaluated points being used in the RBF interpolation during SBAO.

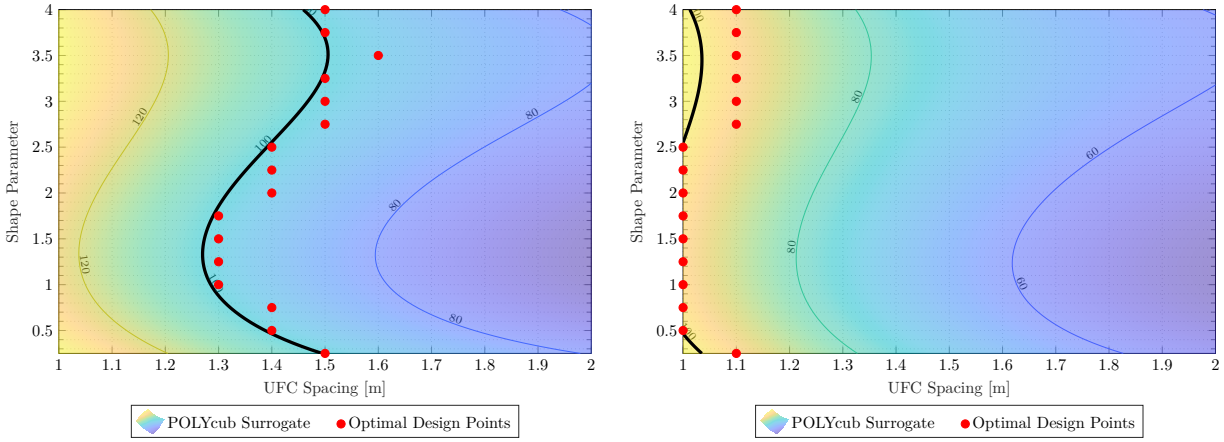

(a) Room Spacing = 15 m (b) Room Spacing = 25 m

Kumaraswamy shape parameters a varying and $b = 1.5$.

Figure A.2: Surrogate optimization results using cubic polynomial surrogates for a Kumaraswamy PDF-like UFC age arrangement (continued from Fig. 4.10)

Table A.4: Optimal design points using cubic polynomial surrogates for a Kumaraswamy PDF-like UFC age arrangement

UFC Spacing [m]	Room Spacing [m]	Shape Parameter	Predicted Maximum Temperature [°C]	Actual Maximum Temperature [°C]	Error [°C]
2.0	10	0.75	97.147	96.505	+0.642
1.9		1.00	98.278	96.595	+1.683
1.9		1.25	96.813	95.306	+1.507
1.9		1.50	96.648	95.916	+0.732
1.9		1.75	97.522	96.823	+0.699
1.9		2.00	99.175	100.137	−0.962
2.0		2.25	96.543	98.257	−1.714
2.0		2.50	98.865	100.080	−1.215
1.5	15	0.25	99.688	98.838	+0.850
1.4		0.50	99.183	101.887	−2.704
1.4		0.75	94.724	95.928	−1.204
1.3		1.00	98.929	96.656	+2.273
1.3		1.25	97.845	94.983	+2.862
1.3		1.50	98.043	96.070	+1.973
1.3		1.75	99.250	99.653	−0.403
1.4		2.00	94.413	96.929	−2.516
1.4		2.25	96.827	99.427	−2.600
1.4		2.50	99.426	101.230	−1.804
1.5		2.75	96.015	96.714	−0.699
1.5		3.00	98.175	97.636	+0.539
1.5		3.25	99.698	98.337	+1.361
1.6		3.50	95.180	93.613	+1.567
1.5		3.75	99.732	99.302	+0.430
1.5		4.00	97.694	99.639	−1.945
1.2	20	0.25	99.685	98.984	+0.701
1.2		0.50	93.573	96.482	−2.909
1.1		0.75	97.502	97.695	−0.193
1.1		1.00	95.183	88.578	+6.605
1.1		1.25	94.328	88.048	+6.280
1.1		1.50	94.678	90.784	+3.894
1.1		1.75	95.975	96.013	−0.038
1.1		2.00	97.960	99.645	−1.685
1.2		2.25	91.796	94.759	−2.963
1.2		2.50	94.294	96.336	−2.042
1.2		2.75	96.703	97.471	−0.768
1.2		3.00	98.765	98.306	+0.459
1.3		3.25	93.229	92.374	+0.855
1.3		3.50	93.733	92.821	+0.912
1.3		3.75	93.113	93.170	−0.057
1.2		4.00	98.363	100.088	−1.725
1.1	25	0.25	94.946	93.988	+0.958
1.0		0.50	99.606	99.734	−0.128
1.0		0.75	97.384	94.029	+3.355
1.0		1.00	96.084	81.551	+14.533
1.0		1.25	95.567	81.073	+14.494
1.0		1.50	95.689	87.569	+8.120
1.0		1.75	96.310	92.864	+3.446
1.0		2.00	97.289	96.232	+1.057
1.0		2.25	98.483	98.416	+0.067
1.0		2.50	99.752	99.903	−0.151

Table A.4: (Continued)

UFC Spacing [m]	Room Spacing [m]	Shape Parameter	Predicted Maximum Temperature [°C]	Actual Maximum Temperature [°C]	Error [°C]
1.1	25	2.75	93.357	92.900	+0.457
1.1		3.00	94.385	93.601	+0.784
1.1		3.25	95.063	94.122	+0.941
1.1		3.50	95.250	94.518	+0.732
1.1		3.75	94.804	94.823	−0.019
1.1		4.00	93.583	95.063	−1.480
				Mean Absolute Error	2.102

Kumaraswamy shape parameters a varying and $b = 1.5$.

Appendix B

Yield Optimization

B.1 Yield of Optimal Points from SBAO

The following figure shows the remaining results (Case 2, 3, 5, and 6) from Monte Carlo simulations in Subsection 5.2.2. The values of variables (UFC spacing, room spacing, and shape parameter) corresponding to each of the three points in the figure are:

Point A $x_1 = 1.6$, $x_2 = 15$, and $a = 0.25$,
Point B $x_1 = 1.3$, $x_2 = 15$, and $a = 1.25$, and
Point C $x_1 = 1.5$, $x_2 = 15$, and $a = 4.00$.

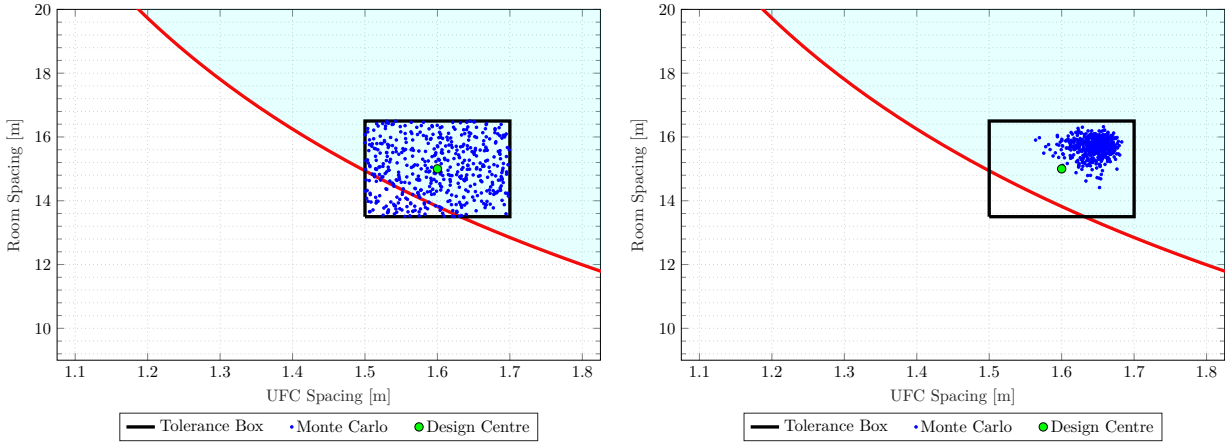

(a) Point A, Case 2

(b) Point A, Case 3

(c) Point A, Case 5

(d) Point A, Case 6

Distribution parameters for each case are from Table 5.1. 500 Monte Carlo simulations shown.

Figure B.1: Monte Carlo simulations for various optimal points from SBAO and design variable distributions (continued from Fig. 5.3)

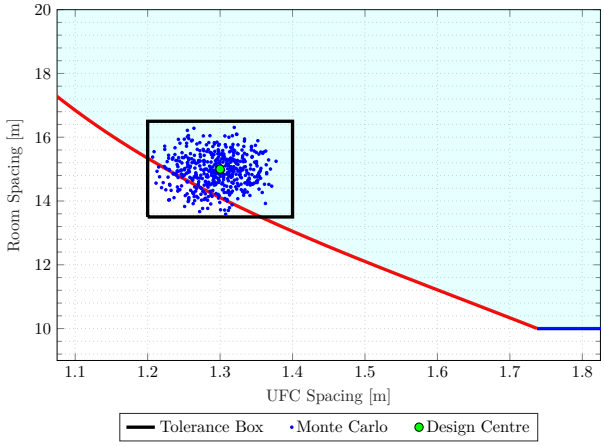

(e) Point B, Case 2

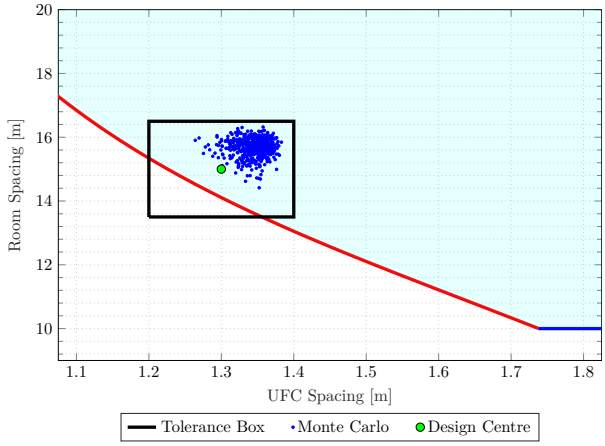

(f) Point B, Case 3

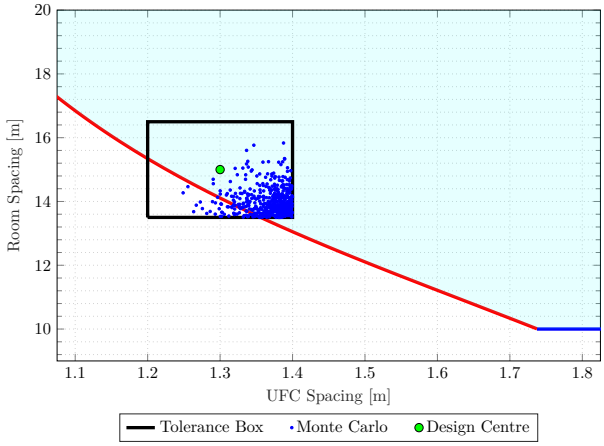

(g) Point B, Case 5

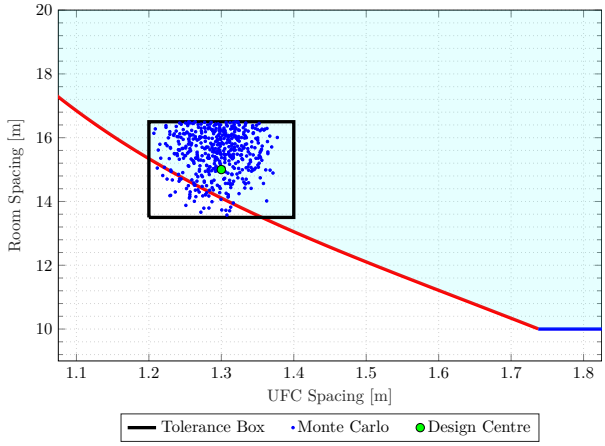

(h) Point B, Case 6

Distribution parameters for each case are from Table 5.1. 500 Monte Carlo simulations shown.

Figure B.1: (Continued)

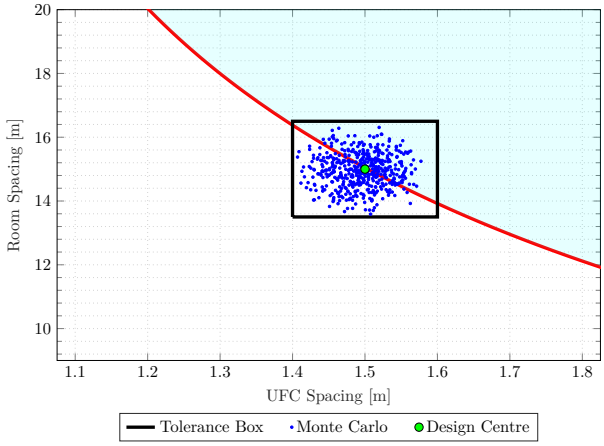

(i) Point C, Case 2

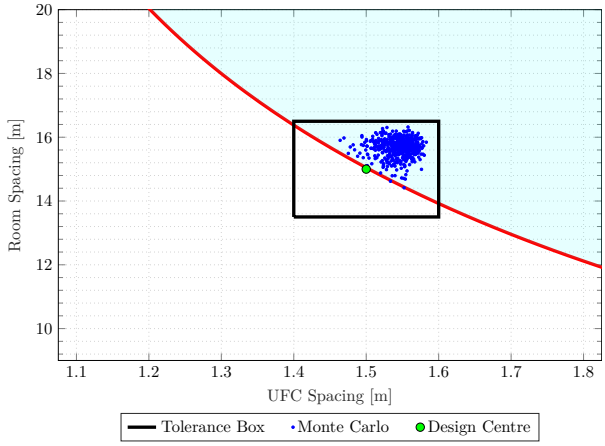

(j) Point C, Case 3

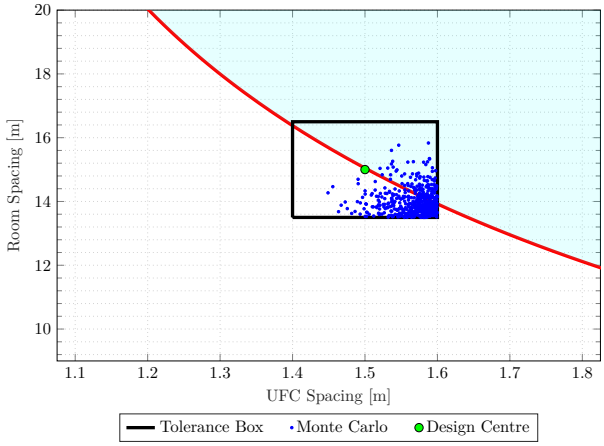

(k) Point C, Case 5

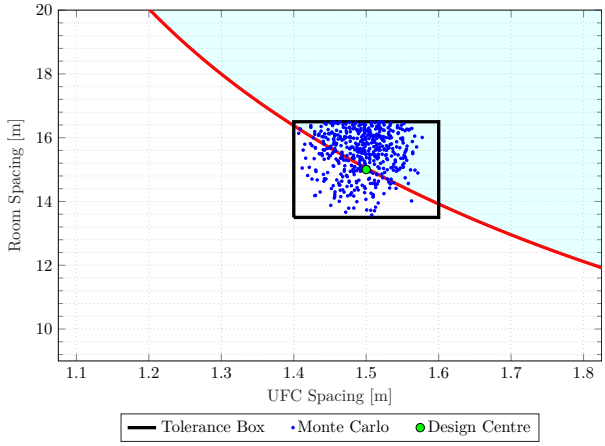

(l) Point C, Case 6

Distribution parameters for each case are from Table 5.1. 500 Monte Carlo simulations shown.

Figure B.1: (Continued)

B.2 Yield Optimization for Nominal Design Points

The following figure shows the remaining results (Case 2, 4, and 6) from yield optimization under design with failure allowance in Subsection 5.3.2, for feasible region $R_{A,\,a=0.25}$.

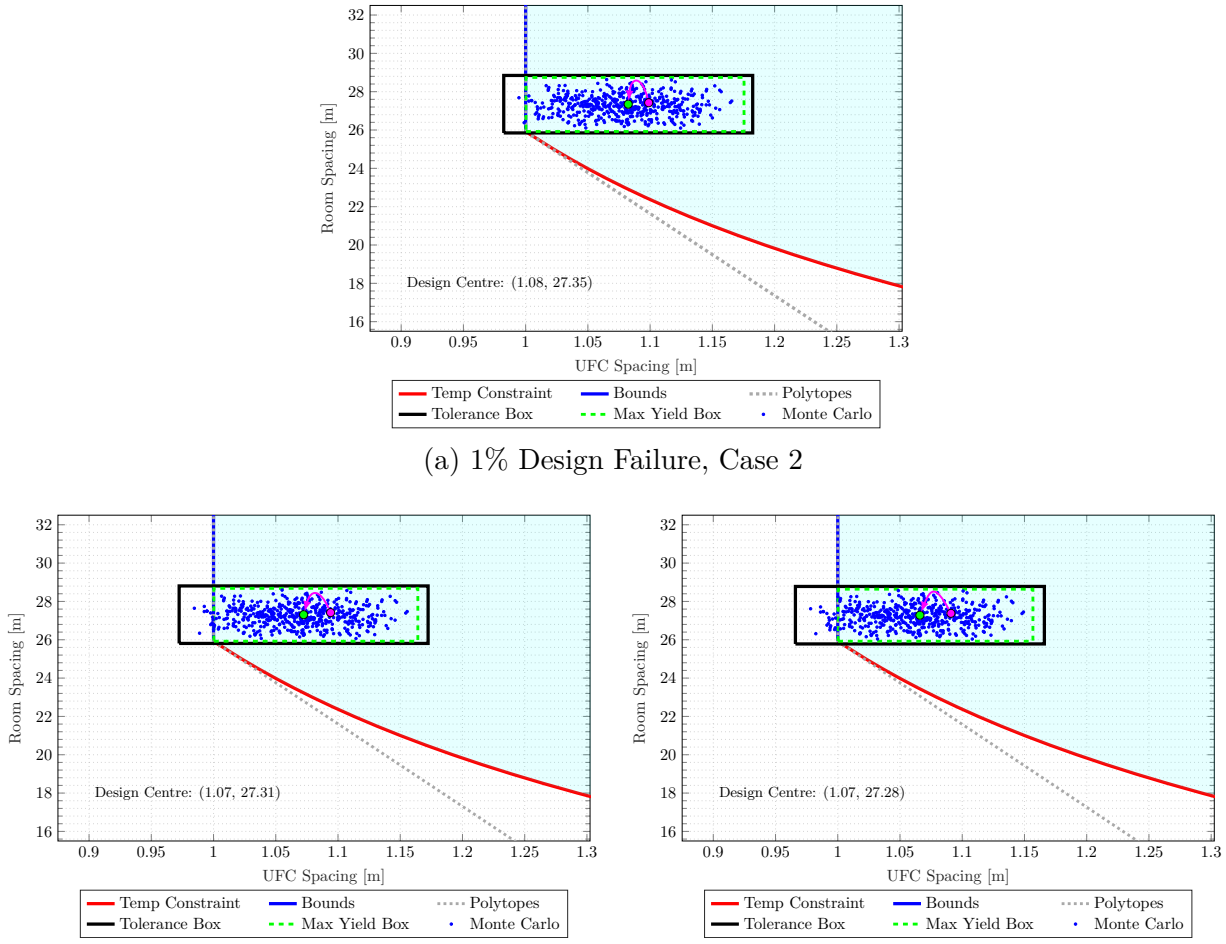

(a) 1% Design Failure, Case 2

(b) 3% Design Failure, Case 2

(c) 5% Design Failure, Case 2

Distribution parameters for each case are from Table 5.1. 500 Monte Carlo simulations shown.
Magenta arrows show the changes in design centre locations relative to those of Case 1 (uniform distributions).

Figure B.2: Design with failure allowance results for feasible region $R_{A,\,a=0.25}$ under various design variable distributions (continued from Fig. 5.5)

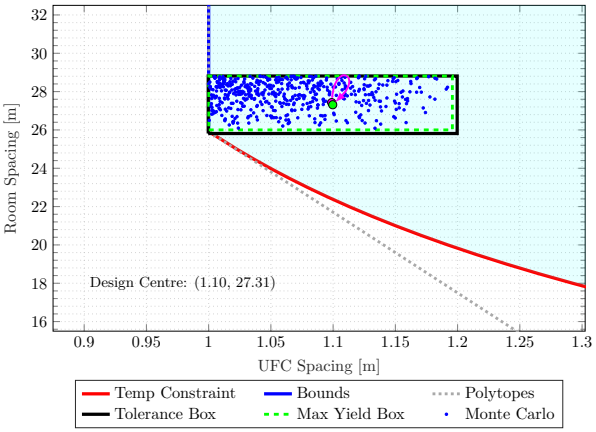

(d) 1% Design Failure, Case 4

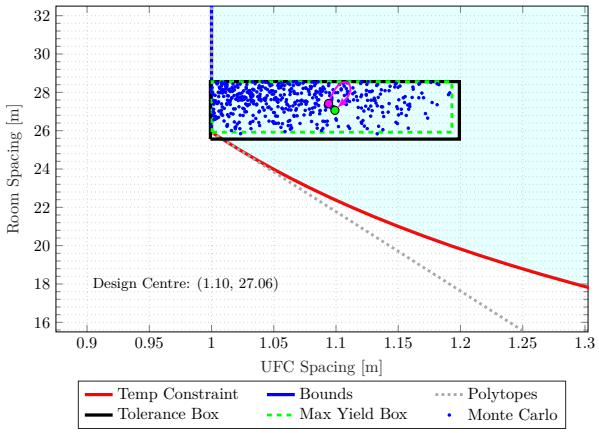

(e) 3% Design Failure, Case 4

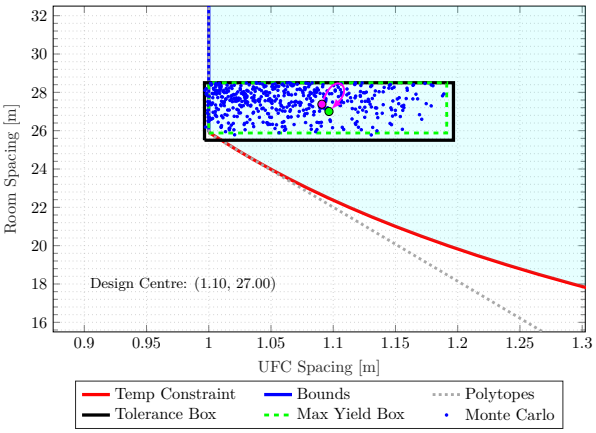

(f) 5% Design Failure, Case 4

Distribution parameters for each case are from Table 5.1. 500 Monte Carlo simulations shown.
Magenta arrows show the changes in design centre locations relative to those of Case 1 (uniform distributions).

Figure B.2: (Continued)

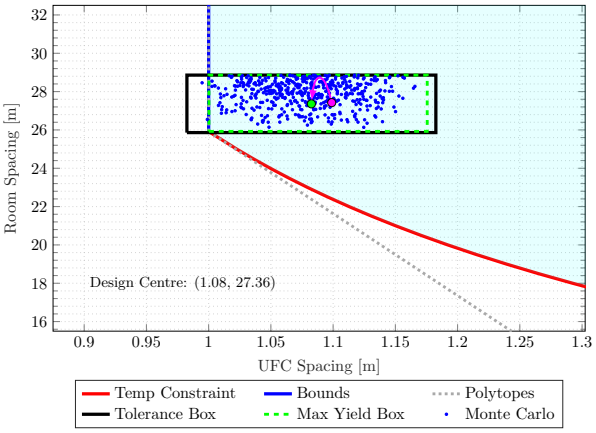

(g) 1% Design Failure, Case 6

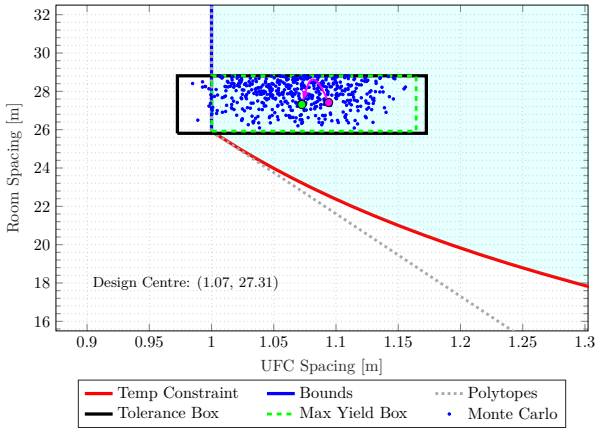

(h) 3% Design Failure, Case 6

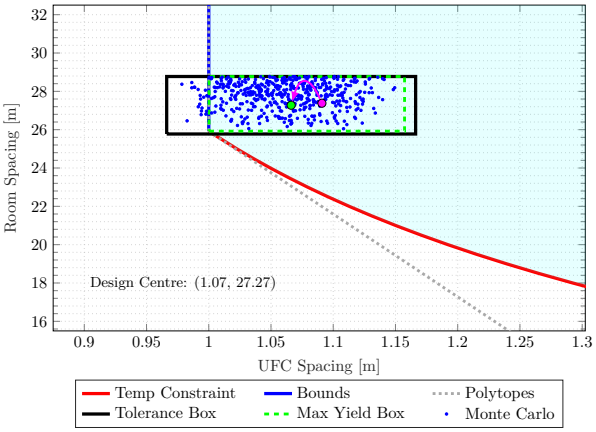

(i) 5% Design Failure, Case 6

Distribution parameters for each case are from Table 5.1. 500 Monte Carlo simulations shown.
Magenta arrows show the changes in design centre locations relative to those of Case 1 (uniform distributions).

Figure B.2: (Continued)

Glossary

Buffer Box

Pre-compacted box made of highly compacted bentonite that is placed around a used fuel container, *see also:* dense backfill, gap-fill.

Dense Backfill (also **spacer block**)

Bentonite block that fills the space between two buffer boxes, *see also:* buffer box, gap-fill.

Fuel Burnup

Measure of how much energy is extracted from nuclear fuel, typically in units of energy released per mass of initial fuel.

Gap-Fill

Bentonite pellets that fill the space between buffer boxes/dense backfill blocks and the excavation, *see also:* buffer box, dense backfill.

IV-25

Original reference used fuel container design by the Nuclear Waste Management Organization.

KBS-3

Methodology for final disposal of spent nuclear fuel by the Swedish Nuclear Fuel and Waste Management Company.

Mark II

Current reference used fuel container design by the Nuclear Waste Management Organization.

Maximin

Maximum of a series of minima.

Non-Collapsing

Describes design points that do not share the same value in any dimension.

Room Spacing

Distance between one placement room and another, from centre to centre, in the deep geological repository.

Space-Filling

Describes design points that uniformly spread over the entire design space, maximizing the distance between any pair of points.

Spacer Block

See: dense backfill.

System Failure

Defined as when the maximum temperature inside the deep geological repository exceeds 100 °C.

UFC Age

Time since used nuclear fuel contained inside a used fuel container was discharged from a nuclear power reactor at the time of placement into the deep geological repository.

UFC Spacing

Distance between one used fuel container and another, from centre to centre, in the deep geological repository.

Yield

Probability of a design meeting specifications.